SELF-ASSEMBLY OF SYNTHESIZED 4-PENTYNOIC ACID FUNCTIONALIZED MAGNETITE-MAGHEMITE NANOPARTICLES ON SILICON DIOXIDE/N-TYPE SILICON SUBSTRATE

AAINAA AQILAH BINTI BAHARUDDIN

FACULTY OF ENGINEERING
UNIVERSITY OF MALAYA
KUALA LUMPUR

2017

SELF-ASSEMBLY OF SYNTHESIZED 4-PENTYNOIC ACID FUNCTIONALIZED MAGNETITE-MAGHEMITE NANOPARTICLES ON SILICON DIOXIDE/N-TYPE SILICON SUBSTRATE

AAINAA AQILAH BINTI BAHARUDDIN

DISSERTATION SUBMITTED IN FULFILMENT OF THE REQUIREMENTS FOR THE DEGREE OF MASTER OF ENGINEERING SCIENCE

FACULTY OF ENGINEERING
UNIVERSITY OF MALAYA
KUALA LUMPUR

2017

UNIVERSITY OF MALAYA
ORIGINAL LITERARY WORK DECLARATION

Name of Candidate: Aainaa Aqilah binti Baharuddin

Registration/Matric No: KGA150011

Name of Degree: Master of Engineering Science

Title of Project Paper/Research Report/Dissertation/Thesis (“this Work”):

Self-Assembly of Synthesized 4-Pentynoic Acid Functionalized Magnetite-Maghemite Nanoparticles on Silicon Dioxide/N-Type Silicon Substrate

Field of Study: Advanced Materials/Nanomaterials

I do solemnly and sincerely declare that:

(1) I am the sole author/writer of this Work;
(2) This Work is original;
(3) Any use of any work in which copyright exists was done by way of fair dealing and for permitted purposes and any excerpt or extract from, or reference to or reproduction of any copyright work has been disclosed expressly and sufficiently and the title of the Work and its authorship have been acknowledged in this Work;
(4) I do not have any actual knowledge nor do I ought reasonably to know that the making of this work constitutes an infringement of any copyright work;
(5) I hereby assign all and every rights in the copyright to this Work to the University of Malaya (“UM”), who henceforth shall be owner of the copyright in this Work and that any reproduction or use in any form or by any means whatsoever is prohibited without the written consent of UM having been first had and obtained;
(6) I am fully aware that if in the course of making this Work I have infringed any copyright whether intentionally or otherwise, I may be subject to legal action or any other action as may be determined by UM.

Candidate’s Signature   Date:

Subscribed and solemnly declared before,

Witness’s Signature   Date:

Name:

Designation:

ABSTRACT

This study is divided into two parts; i) synthesis of the functionalized magnetite-maghemite (Fe_3O_4-γ-Fe_2O_3) nanoparticles (FNPs) and ii) self-assembly of the FNPs on silicon substrate which serves as metal-oxide-semiconductor capacitor. Bare iron oxide nanoparticles (NPs) were synthesized by co-precipitation method and were altered to pH 12 (optimum pH) using NH_4OH to promote dispersity right before ex-situ modification with oleic acid (0.2-0.8 g/g oleic acid to iron oxide) and subsequent 4-pentynoic acid (1.63 mmol) functionalization. In the first part, X-ray-diffraction (XRD) showed that lattice constants of the iron oxides co-exist as Fe_3O_4-γ-Fe_2O_3. Transmission electron microscopy showed that the particle size (10.94 ± 0.24 nm) of sample P-0.4 is complementary to the mean crystallite size (10 ± 1 nm) attained from XRD. Thermogravimetric-differential thermal analysis indicated that monolayer oleic acid FNPs was produced for ex-situ modification of 0.2 g/g oleic acid to iron oxide. Whereas higher concentrations of oleic acid ex-situ modifications generated bilayer oleic acid-coated FNPs to which, functionalization of 4-pentynoic acid was only successfully performed as indicated by Fourier transform infrared spectroscopy. Zetasizer affirmed the highly stabilized dispersion of FNPs at pH 12 with zeta potentials at relatively -47 to -75 mV and mean hydrodynamic particle size distributions of ~35-48 nm. Sample 0.4 g/g oleic acid to iron oxide, functionalized with 4-pentynoic acid, with the most stabilized nanoparticles in an aqueous medium was chosen for self-assembly in the second part. In the second part, investigation on the relation between temperature-influential self-assembly (70-300 ˚C) of the samples on SiO_2/n-Si structure with their electrical characteristics was conducted. XRD analysis revealed that 8 ± 1 nm of FNPs which aggregated non-uniformly into film of 12.6 μm thickness was self-assembled via Si-O-C linkages. Besides, increasing temperature of heat treatments induced growth of native oxide, SiO_2 on the Si substrate. Other implications of increasing heating temperature disclosed by attenuated total reflectance infrared analysis are breakdowns of Si-O-C linkages and formations of Si-OH defects. Atomic force microscopy implied that sample with more physisorbed surfactants exhibited the highest root-mean-square roughness (18.12 ± 7.13 nm) and vice versa (12.99 ± 4.39 nm). The increased saturation magnetization (71.527 $A \cdot m^2/kg$) and coercivity (929.942 A/m) acquired by vibrating sample magnetometer of the sample heated at 300 ˚C verified the surfactants' disintegration. Leakage current density-electric field characteristics signified that sample heated at 150 ˚C with the most aggregated FNPs as well as the most developed Si-O-C linkages demonstrated the highest breakdown field and barrier height at 2.58×10^{-3} MV/cm and 0.38 eV respectively. Whereas sample heated at 300 ˚C with the least Si-O-C linkages and more Si-OH defects as well as lesser aggregated NPs showed the lowest breakdown field and barrier height at 1.08×10^{-3} MV/cm and 0.19 eV respectively.

ABSTRAK

Kajian ini terbahagi kepada dua bahagian; i) Nanopartikel magnetit-maghemite (Fe_3O_4-γ-Fe_2O_3) sintesis yang difungsionalisasi (FNPs) dan ii) pendepositan sendiri FNPs di atas silikon yang berkhidmat sebagai kapasitor logam-oksida-semikonduktor. Nanopartikel ferrum oksidatidak diubahsuai (NPs) telah disintesis melalui kaedah pemendakan dan diubah kepada pH 12 (pH optimum) sebelum diubahsuai secara ex-situ dengan asid oleik (0.2-0.8 g/g; asid oleik/ferrum oksida). Seterusnya, pengfungsian NPs dengan asid 4-pentynoic (1.63 mmol) dilaksanakan Untuk bahagian pertama, pembelauan sinar-X (XRD) menunjukkan pemalar kekisi ferrum oksida wujud bersama-sama sebagai Fe_3O_4-γ-Fe_2O_3 namun sebahagian besarnya wujud sebagai Fe_3O_4 seiring dengan peningkatan konsentrasi asid oleic (9-14 nm julat saiz kristal). Penghantaran elektron mikroskop menunjukkan saiz partikel (10.94 ± 0.24 nm) sampel P-0.4 yang lebih kurang sama dengan purata size kristal (10 ± 1 nm) dianalisis oleh XRD. Analisis termogravimetri- pengkamiran haba menunjukkan satu lapisan asid oleik FNPs dihasilkan bagi pengubahsuaian sebanyak 0.2 g/g asid oleik: ferrum oksida. Manakala kepekatan yang lebih tinggi menghasilkan pengubahsuaian dua lapisan FNPs dimana, pengfungsian asid 4-pentynoic hanya berjaya dilakukan seperti yang ditunjukkan oleh fourier spektroskopi inframerah. Zetasizer mengesahkan bahawa media FNPs sangat stabil pada pH 12 dimana daya zeta tercatat lebih kurang -42 hingga -75 mV dan hidrodinamik taburan saiz zarah ~ 35-48 nm. Sampel 0.4 g/g asid oleik: ferrum oksida modifikasi bersama pengfungsian asid 4-pentynoic, dengan kestabilan yang paling bagus di dalam media akueus dipilih untuk pengdepositan sendiri dalam bahagian kedua. Untuk bahagian kedua, siasatan mengenai hubungan antara suhu-berpengaruh deposit-sendiri (70-300 ˚C) sampel di atas struktur SiO_2/n-Si dengan ciri-ciri elektrik sampel telah dilaksanakan. Analisis XRD menunjukkan bahawa 8 ± 1 nm FNPs yang agregat secara tidak seragam dan membentuk menjadi filem dengan ketebalan 12.6 mikron telah berjaya dideposit dengan sendirinya melalui hubungan Si-O-C. Selain itu, peningkatan suhu haba menggalakkan pertumbuhan SiO_2 di atas substrat Si. Implikasi lain yang diperlihatkan melalui peningkatan suhu pemanasan (dianalisis oleh Pengurangan jumlah pantulan inframerah) ialah pemutusan hubungan Si-O-C dan pembentukan pemudaratan Si-OH. Daya atomik mikroskop menunjukkan sampel dengan lebih surfaktan yang terfungsi secara fizikal mempamerkan punca-min-persegi kekasaran yang paling tinggi (18.12 ± 7.13 nm) dan sebaliknya (12.99 ± 4.39 nm). Sampel magnetometer bergetar menunjukkan peningkatan pemagnetan tepu (71.527 $A\cdot m^2/kg$) dan coercivity (929.942 A/m) bagi filem yang dipanaskan pada 300 ˚C mengesahkan perpecahan surfaktan dari FNPs. Aliran ciri-ciri ketumpatan elektrik arus bocor menunjukkan sampel yang dipanaskan pada 150 ˚C yang mempunyai agregat FNPs paling ketara dan hubungan Si-O-C yang paling banyak menunjukkan breakdown field (2.58 x 10-3 MV/cm) dan barrier height (0.38 eV) tertinggi. Manakala sampel dipanaskan pada 300 ˚C dengan ciri-ciri yang bertentangan menunjukkan breakdown field (1.08 x 10-3 MV/cm) dan barrier height (0.19 eV) yang paling rendah.

ACKNOWLEDGEMENTS

I would like to express my earnest appreciation to many parties, especially to my supervisors, Assoc. Prof. Ir. Dr. Ang Bee Chin and Ir. Dr. Wong Yew Hoong. I am most grateful for their uncompromising support, astounding guidance and advice in which they had so generously bestowed upon me throughout the completion of this research.

My appreciation also goes to the Head, Centre for Advanced Materials (CAM), Department of Mechanical Engineering, Faculty of Engineering, Assoc. Prof. Dr. Hendrik Simon Cornelis Metselaar**,** whose effort had enabled me to explore extensive knowledge in this subject area. Moreover, thank you to the Centre for Research Grant Management (PPGP), for awarding this particular research, a Postgraduate Research Grant (PPP) (PG215-2015B).

I am also indebted to the Science Officers and my supportive colleagues whom had assisted me in any possible ways throughout this journey. Lastly, to my family for their infinite encouragement; thank you.

TABLE OF CONTENTS

LIST OF FIGURES

LIST OF TABLES

LIST OF SYMBOL AND ABBREVIATIONS

$\sigma_{\bar{x}}$	: Standard error
ac	: Alternating current
AFM	: Atomic force microscopy
APTES	: 3-(aminopropyl)triethoxysilane
ATR-IR	: Attenuated total reflectance infrared
Conc.	: Concentration
dc	: Direct current
FE-SEM	: Field emission scanning electron microscope
FNPs	: Functionalized nanoparticles
FTIR	: Fourier transform infrared
H_{ci}	: Coercivity
Hrs	: Hours
IR	: Infrared region
JCPDS	: Joint Committee on Powder Diffraction Standards
J-E	: Leakage current density-electric field
Min	: Minutes
MOS	: Metal oxide semiconductor
NM	: Not mentioned
NPs	: Bare nanoparticles
PSD	: Particle size distribution
PVTri	: Poly(1-vinyl-1,2,4-triazole)
SAMs	: Self-assembly monolayers
Si	: Silicon
SP	: Superparamagnetic
TEM	: Transmission electron microscopy
Temp.	: Temperature
THF	: Tetrahydrofurane
THY	: N-1-(Triethoxysilylundecyl)thymine
VSM	: Vibrating sample magnetometer
XRD	: X-ray-diffraction
ZP	: Zeta potential

LIST OF APPENDICES

CHAPTER 1: INTRODUCTION

1.1 Background and problem statements

Magnetic particles, especially in nanometer size are desirable materials in various fields. Among them are the iron oxide nanoparticles (NPs) of various kinds and derivatives which include magnetite (Fe_3O_4), maghemite (γ-Fe_2O_3), and hematite (α-Fe_2O_3). Iron oxide NPs possess good compatibility as material building blocks for a particularly wide range of applications including high-density data storage (Ghosh & Srıvastava, 2014; Sun, 2006; Terris & Thomson, 2005), catalysis (Hosseini-Monfared *et al.*, 2015; Lee *et al.*, 2014), ferrofluids and bioprocessing (Némethová *et al.*, 2017; Goswami *et al.*, 2016; Jeong *et al.*, 2007;) because of its fascinating transport and magnetic properties.

In the aspect of spin electronic device, magnetite (Fe_3O_4) particularly, is a promising material (Kotnala & Shah, 2015; Muñoz-Noval *et al.*, 2015), owing to its nearly 100% spin polarization (Yang, 2011) and its superparamagnetic behaviour at room temperature with high saturation magnetization, M_s. Moreover, its non-toxicity and high biocompatibility makes it reasonable to be used in many applications especially in biotechnology fields (Petcharoen & Sirivat, 2012). It is a black ferrimagnetic mineral, consists of Fe(II) and Fe(III) which is often non-stoichiometric hence, exhibited cation deficient Fe(III) layer. It has an inverse spinel crystal structure with a unit cell consisting of 32 oxygen atoms in a face-centred cubic structure. While the Fe^{2+} ions and half of the Fe^{3+} ions occupy the octahedral sites, the other half of Fe^{3+} ions occupy the tetrahedral sites (Wasilewski & Kletetschka, 1999). Its half metallic properties have made it a promising candidate to be exploited in spin electronic applications (Cattaruzza *et al.*, 2005).

However, Fe_3O_4 is known to transform into γ-Fe_2O_3 with temperature increase (Faria *et al.*, 1997). Hence, co-existence of magnetite-maghemite (Fe_3O_4-γ-Fe_2O_3) is common (Chowdhury & Yanful, 2013; Chowdhury *et al.*, 2012; Kim *et al.*, 2012; Chowdhury & Yanful, 2010). Spinel structure of γ-Fe_2O_3 is similar to that of Fe_3O_4 but with a larger number of cation vacancies (Greaves, 1983). In a study conducted by Yanagihara et al., room temperature resistivity of their γ-Fe_2O_3 film was achieved at $\sim 10^2$ Ω cm which is five orders of magnitude higher than that of Fe_3O_4 (Yanagihara *et al.*, 2006). To date, electrical properties of the associated phases; Fe_3O_4-γ-Fe_2O_3 have not been discussed despite the fact that these phases have more tendency to naturally coexist.

Furthermore, assembling magnetic NPs such as iron oxide into arrays is a very anticipating and significant challenge because of their high potentials in the development of nanodevices for spintronic, magnetic, and magneto-electronic application (Pichon *et al.*, 2012). Despite the promising advantages, iron oxide has its shortcomings. Iron oxide NPs in general, are unstable and aggregate rapidly. Sedimentation is usually stimulated by their large surface area-to-volume ratio whereby agglomeration is triggered to reduce their surface energy (Yang *et al.*, 2010). To mitigate these setbacks, modification of iron oxide with surfactants is essential in introducing stearic repulsion between the particles. Hence, surface modification of iron oxide NPs with oleic acid was carried out in this study to promote dispersibility in polar basic medium in the determination of abating the anticipated agglomeration (Shete *et al.*, 2015).

It has been reported by many that the properties of iron oxide NPs depend strongly on the preparation method, experimental conditions such as chemical routes, pH, type of precursors, solvent, temperature, gas atmosphere, and ex-situ treatment (Petcharoen & Sirivat, 2012; Lemine *et al.*, 2012; Andrade *et al.*, 2012). Moreover, the size and morphology of iron oxide NPs influence the electrical, optical, and magnetic properties of the NPs (Lemine *et al.*, 2012; Andrade *et al.*, 2012). Thus, ex-situ modifications with surfactants (oleic acid and 4-pentynoic acid) were optimized in this study along with enhanced stability at pH 12 (optimum pH) to achieve the best properties of iron oxide NPs. In order to accomplish superparamagnetic behavior and a single domain of particles, the particle size of iron oxide should be in the range of 30-50 nm (Petcharoen & Sirivat, 2012). Various synthesis methods had been reported in the literature. Among these methods, co-precipitation was chosen in this study due to its ease, large yield and economy (Mahmed *et al.*, 2014; Roth *et al.*, 2015).

In the relevance of iron oxide surface modification with surfactant, oleic acid has been used regularly as coating agent because of its greater affinity towards the material's surface compared to other surfactants (Shete *et al.*, 2015; Soares *et al.*, 2014). Oleic acid has a non-polar hydrocarbon tail and a polar carboxylic acid head group. While the polar head group anchors on the surface of iron oxide, the non-polar tail extends into solution, causing iron oxide to become hydrophobic and dispersible particularly in organic solvent (Šutkaa *et al.*, 2014).

In-situ surface modification with oleic acid during synthesis of iron oxide was often reported in the literature (Khalil *et al.*, 2014; Jiang *et al.*, 2014). However, it is difficult to control and produce single phase iron oxide due to different metal oxidation states, leading to the existence of various phases of the iron oxide, such as magnetite-maghemite (Fe_3O_4-γ-Fe_2O_3) (Pichon *et al.*, 2012). To date, phase control of the iron oxide is still a major concern. Even though this is not one of the objectives of this study, an improved approach of a single phase accentuation of iron oxide NPs by ex-situ modification with various concentrations of oleic acid and subsequent functionalization with a fixed amount of 4-pentynoic acid is discovered, leading to several plausible mechanisms.

The first part of this study focuses on mechanisms of the synthesized ex-situ oleic acid-coated iron oxide FNPs functionalized with 4-pentynoic acid. The mechanisms of highly stabilized compounds in pH 12 medium permits the understanding of iron oxide FNPs morphological relationship with the chemical reactions involved. Besides, the reaffirmation of the 4-pentynoic acid functionalization to the iron oxide FNPs had set a milestone to the development of these FNPs on silicon substrate. This enabled productive investigation on electrical characteristics of the FNPs in the second part of this study.

In addition to that, the potential of iron oxide NPs particularly Fe_3O_4-γ-Fe_2O_3 as dielectric film in high density data storage has yet been properly assessed. There were deficiencies of reported works in the literature concerning breakdown field and barrier height on this material. To benefit the usage of iron oxide NPs in memory and even gas sensing devices, a comprehensive understanding on electrical properties of the iron oxide FNPs/SiO_2/Si system is vital. Therefore, a decent study on the development of this material on Si substrate facilitated a proper investigation on its electrical properties; e.g. leakage current. This was executed on the second part of this study.

Apart from that, covalent development of magnetic nanoparticles on the surface of substrate is a significant research topic related to technological applications. In order to anchor nanoparticles to a surface such as silicon, special linkers are required to act as bridges between the surface and the nanoparticles. It was demonstrated that linear-chain-1-carboxylic acids with unsaturated ends are suitable to act as bridges for certain applications on unoxidized silicon substrate through hydrosilylation reaction. These molecules were expected to be bound to silicon surface through a covalent Si-C bond. Thus, 4-pentynoic acid which exhibits terminal alkyne as a part of its chemical structure was chosen to be functionalized to the iron oxide NPs. Alkynes is more reactive on silicon surface than other compounds such as alkenes due to higher electron density around the triple bond (Ng *et al.*, 2009). The terminal alkyne of 4-pentynoic acid was anticipated to form hydrosilylation reaction with silicon. Incorporation of this will allow additional properties to be exploited in the design of silicon base electronic devices (Cattaruzza *et al.*, 2005). But alas, such bonding is not accomplished in this study. Instead, Si-O-C bond was observed as a repercussion of native oxide (SiO_2) growth.

The second part of this study focuses on the relation between temperature-influential self-assembly of 4-pentynoic acid functionalized Fe_3O_4-γ-Fe_2O_3 FNPs on SiO_2/n-Si structure with their electrical characteristics. The temperatures were varied at 70-300 ˚C and the samples were sputtered with aluminium. It is more realistic and practical to examine Fe_3O_4-γ-Fe_2O_3 mixture due to common association of the two phases in nature. Since investigation on the association of self-assembly and electrical properties of Fe_3O_4-γ-Fe_2O_3 has not been aptly discussed before, the following objective of this study is closely related to the role of surface chemistry at the interface of 4-pentynoic acid functionalized Fe_3O_4-γ-Fe_2O_3 FNPs/SiO_2/n-Si on oxide breakdown field and barrier heights. Formation of linkages and defects in this study were influenced by different heating temperatures of the self-assembly.

1.2 Significance of study

Self-assembly monolayers (SAMs) are essentially an ideal part of good building blocks in nanotechnology, on account of great structural stabilization of covalent bonds, acting as linkages. SAMs are introduced to improve performances of the most critical interfaces, i.e. metal/semiconductor and dielectric/semiconductor interfaces (Ji *et al.*, 2016; Fabre, 2016). In this study, Fe_3O_4-γ-Fe_2O_3 FNPs/SiO_2/Si interfaces were considered. Strong chemical linkage (Si-O-C) between iron oxide FNPs and SiO_2/Si structure in this study was achieved by designing appropriate organic coatings; oleic acid and 4-pentynoic acid (the one that is accountable to form the linkage) to the bare NPs.

The chemistry of surface and interfaces are intriguing especially for organic-inorganic electronic device as most phenomena (charge injection and transport) occur at the interfaces (Miozzo *et al.*, 2010; Majee *et al.*, 2015). Often times however, electrical properties of a single phase iron oxide; either Fe_3O_4 (Deniz *et al.*, 2016; Wang *et al.*, 2016; Deniz *et al.*, 2013; Vikulov *et al.*, 2016; Çaldıran *et al.*, 2013) or γ- Fe_2O_3 (Ali *et al.*, 2015; Nadeem *et al.*, 2014; Zhang *et al.*, 2012; Hasegawa *et al.*, 2007) were reported without paying heeds to interfaces between the materials and substrates. On the other hand, where self-assembly interactions between iron oxides and substrates were deliberated (Singh *et al.*, 2015; Pichon *et al.*, 2012; Sarantopoulou *et al.*, 2008; Cattaruzza *et al.*, 2005; Cattaruzza *et al.*, 2004;), electrical properties of these materials were neglected. Unfortunately, there is hardly any discussion reported on association between iron oxide and substrate interfaces alongside their electrical characteristics in the literature, particularly Fe_3O_4-γ-Fe_2O_3.

In addition, achieving large barrier height at heterojunction materials interface is crucial for high performance of device in electronics industry (Deniz *et al.*, 2016). Furthermore, energy level alignment at organic/metal interfaces is critical for Ohmic contact. Unfortunately, a simple Mott-Schottky model is not necessarily ascribed to such contact. Most of the time, the interface exhibits an extra dipole barrier which tends to change metal work function, hence the interface barrier height (Wan *et al.*, 2005). By introducing dipoles or chemical interactions at the metal surface, charge injection into the metal-oxide-semiconductor (MOS) structure can be enhanced. Ultimately, such interfaces can be accomplished through SAMs (Miozzo *et al.*, 2010). In a retrieval of barrier height conducted on Fe_3O_4/n-Si by Deniz et al., an average of 0.91 eV was achieved at room temperature (Deniz *et al.*, 2016). Whereas investigations on two different Fe_3O_4/p-Si structures attained 0.72 eV (Çaldıran *et al.*, 2013) and 0.88 eV (Deniz *et al.*, 2013) of barrier heights.

The second part of this study was particularly dedicated to the investigation on association between self-assembly of 4-pentynoic acid functionalized Fe_3O_4-γ-Fe_2O_3 NPs on SiO_2/n-Si structure with electrical characteristics. The self-assembly approach which was influenced by different heating temperatures (70-300 ˚C) has opened up better understandings on how the formation of linkages and defects (prior self-assembly) at the interface affected electrical breakdown field and barrier height. This has subsequently, initiated better ideas for future development of self-assembly silicon based MOS structure particularly in the presence of SiO_2.

1.3 Objectives of study

The objectives of study include:-

1. To synthesize highly stabilized ex-situ oleic acid-coated Fe_3O_4-γ-Fe_2O_3, functionalized with 4-pentynoic acid (FNPs) at different concentrations of oleic acid to iron oxide.
2. To deposit the FNPs on SiO_2/n-Si structure by self-assembly method at different heating temperatures.
3. To investigate the association between temperature-influential self-assembly of the FNPs with electrical characteristics using current-voltage systems.

CHAPTER 2: LITERATURE REVIEW

2.1 Iron oxide nanoparticles (NPs)

Iron oxide nanoparticles (NPs) are attractive magnetic materials, which can be used in various applications, such as magnetic storage or memory devices, supercapacitors, ferrofluids, catalysts, gas sensors, magnetic resonance imaging (MRI) contrast agents, drug delivery facilitators and hyperthermia applications. The derivatives of this oxide NPs include magnetite (Fe_3O_4), maghemite (γ-Fe_2O_3), and hematite (α-Fe_2O_3). Different phases of iron oxide NPs will lead to different properties for various applications. Thus, synthesizing iron oxide nanoparticles into optimum particle size, size distribution, tailored particle geometry, and morphology are becoming imperative in the area of nanomaterials (Camponeschi, 2008; Ramimoghadam, 2014). Furthermore, iron oxide is desirable owing to its low cost, environment friendly nature, and abundance (Li *et al.*, 2016).

According to Lu and coworkers (2007), successful application of magnetic NPs in the aforementioned areas is substantially depended on the stability of the NPs under a range of various conditions. Often times, the NPs perform best under a critical size value range, typically around 10-20 nm. Each NP becomes a single magnetic domain and displays superparamagnetic behavior when the temperature is above blocking temperature. Such individual NP has a large constant magnetic moment and behaves like a giant paramagnetic atom with a fast response to applied magnetic fields and negligible remanence (residual magnetism), as well as coercivity (the field required to bring the magnetization to zero) (Lu *et al.*, 2007).

2.1.1 Properties of iron oxide NPs

Iron oxide nanoparticles (NPs) possess unique features compared to equivalent larger-scale materials. Since iron oxide NPs have different surface structures and surface interactions compared to the sub-micron sized particles, nanoparticles have an extremely high tendency of adhesion and aggregation. Thus, for industrial applications, it is important to develop techniques to control the dispersion/aggregation phenomena of nanoparticles to apply them into functional materials and products (Pichon *et al.*, 2012).

Among the iron oxides, magnetite (Fe_3O_4) is the most studied material due to its superparamagnetic behavior at room temperature with high saturation magnetization in which electron delocalization occur between adjacent site of both Fe^{2+} and Fe^{3+} (Lu *et al.*, 2007). Moreover, its non-toxicity and high biocompatibility makes it reasonable to be used in many applications especially in the biotechnology fields (Smith & Hashemi, 2006, p. 14). The Curie temperature (T_C) of magnetite is 860 K. Saturation magnetization decreases gradually and drops to zero at Curie temperature (Shete *et al.*, 2015).

Fe_3O_4 is a black ferromagnetic mineral, consists of Fe^{2+} and Fe^{3+} which is often non-stoichiometric resulting in cation deficient Fe^{3+} layer. It has an inverse spinel crystal structure with a unit cell consisting of 32 oxygen atoms in a face-centred cubic structure and a unit cell edge length of 0.839 nm. While the Fe^{2+} and half of the Fe^{3+} occupy the octahedral sites, the other half of Fe^{3+} occupy the tetrahedral sites (Shete *et al.*, 2015). Fe_3O_4 is essentially unstable under oxidizing conditions and may be transformed to γ-Fe_2O_3 and α-Fe_2O_3 at high temperatures (Lu *et al.*, 2007). Nonetheless, α-Fe_2O_3 is reversible to Fe_3O_4 through hydrogen reduction (Pang *et al.*, 2016).

Based on the band calculations, the conduction electron is expected to be fully spin polarized. Hence, magnetite is half metallic but with a strong tendency to form polarons below T_C and the conductivity shows small activation energy. However, the mutual spin-coupling forces are destroyed if temperature exceeds T_C. Its half metallic properties have made it a promising candidate to be exploited in spin electronic applications (Soares, 2014).

In conjunction with that, Fe_3O_4 is a negative temperature coefficient type of thermistor, a very attractive ceramic compound whose resistance decreases with increasing temperature. Thereby its conductivity creates a linear relationship with temperature. Moreover, Fe_3O_4 has a relatively low resistivity of approximately 10^{-5} Ω.m which boosts its attribute as a more enticing thermistor compared to most regular metal oxides with resistivity of about 10^{8} Ω.m. Fe_3O_4 is deemed as a good electrical conductor because of the random location of the Fe^{2+} ions and Fe^{3+} ions in the octahedral sites. This enables transfer of electrons between Fe^{2+} ions and Fe^{3+} ions while maintaining charge neutrality (Smith & Hashemi, 2006, p. 566).

In the prospect of supercapacitors, Fe_3O_4 possesses a relatively high theoretical lithium storage capacity and acts as a highly pseudocapacitive material through redox reactions (Ma *et al.*, 2015). Thus far, Fe_3O_4 has been under the limelight in the development of electrochemical energy storage and conversion device; as a response to the gradual depletion of fossil fuel and environmental quality downgrade (Li *et al.*, 2016).

In several published works, Fe_3O_4 was composited with graphene oxide to modify electrochemical property of the supercapacitors. Aside from increasing the whole capacitance, incorporation of Fe_3O_4 facilitated stabilization of the graphene sheet (Yan *et al.*, 2015; Li *et al.*, 2016). Fe_3O_4/carbon coated silicon ternary hybrid composites were also fabricated in 2015 by Oh et.al. In a nutshell, Fe_3O_4 is deemed as a good material for graphene-based composite for supercapacitors (Wang *et al.*, 2014; Liu *et al.*, 2014).

2.1.2 Synthesis of iron oxide NPs by co-precipitation method

It has been reported by many that the properties of iron oxide NPs depend strongly on preparation method, experimental conditions such as chemical routes, pH, type of precursors, solvent, temperature, gas atmosphere, and ex-situ treatment (Yang *et al.*, 2010; Lemine *et al.*, 2012). Moreover, the size and morphology of iron oxide NPs influence the electrical, optical, and magnetic properties of the NPs (Yang *et al.*, 2010; Lemine *et al.*, 2012). Hence, the mentioned parameters should be optimized in order to achieve the best properties of iron oxide NPs.

The method should enable high reproducibility taking into account of the nanoparticle size, structure, morphology, and good process scale-up without adverse effects on the quality of products and the environment (Camponeschi *et al.*, 2008). In order to achieve superparamagnetic behaviour and single domain particles, the particle size of iron oxide should be in the range of 30-50 nm (Smith & Hashemi, 2006, p. 815). Various methods have been reported in the literature. These include co-precipitation, thermal decomposition, solvothermal and hydrothermal processes and microemulsion process (Pang *et al.*, 2016). However, among these methods, co-precipitation is most commonly used to synthesize iron oxide NPs due to its ease, large yield and economy (Andrade *et al.*, 2012; Mahmed *et al.*, 2014; Roth *et al.*, 2015).

The co-precipitation process engages the reaction between Fe^{2+} and Fe^{3+} aqueous salt solution with precipitating agent such as sodium hydroxide (NaOH) or ammonium hydroxide (NH_4OH). The size, shapes and composition of the iron oxide NPs are influenced by the type of salts used (e.g chlorides, sulfates, nitrates), molar ratio of the iron precursors, reaction temperature, pH environment, introduction of surfactants and other reaction parameters (Pang *et al.*, 2016). The chemical reaction of co-precipitation can be expressed as the following (Darroudi *et al.*, 2014):

$$\mathrm{Fe^{2+} + 2Fe^{3+} + 8OH^- \rightarrow Fe_3O_4 + 4H_2O}$$

The major drawback of co-precipitation is the inevitable particles nucleation and subsequent growth throughout the process. As results, particles synthesized are relatively large, have broad size distribution, poor crystallinity, polydisperse, and irregular in morphology (Jing *et al.*, 2012). Therefore, it is useful to perform appropriate modifications on the particles to improve their features which are relevant to their respective fields of applications (Pang *et al.*, 2016).

Most researches preferred chloride salts for both Fe^{2+} and Fe^{3+} (Upadhyay *et al.*, 2016; Rehana *et al.*, 2015; Soares *et al.*, 2014) whereas for the replacement of chloride salt for Fe^{2+}, most researches would opt for sulphate (Mir *et al.*, 2015; Aliakbari *et al.*, 2015). Besides, the most favorable molar ratio used in the co-precipitation method of Fe^{2+}:Fe^{3+} was 2:1. This often resulted in the yield of approximately 10 nm of particle size.

Upadhyay *et al.* (2016) had implemented both di-salt and mono-salt synthesis of iron oxide NPs. However, the di-salt co-precipitation had produced the most desirable size of ~7.9 nm. A critical size of 36 nm from magnetization measurement was obtained, above which, particles were considered multi domain whereas below 14 nm, the particles were superparamagnetic. The coercivity of the NPs was varied between 9.55-163 Oe which indicates the changes of superparamagnetism of the NPs to single domain with increasing size (Upadhyay *et al.* 2016).

2.1.3 Relevance of surface modification of iron oxide NPs

Iron oxide NPs are unstable and aggregate rapidly due to their large surface area-to-volume ratio hence undergo agglomeration to decrease their surface energy. This can be avoided by coating the iron oxide NPs with surfactants in order to introduce stearic repulsion between the NPs (Šutkaa *et al.*, 2014; Khalil *et al.*, 2014; Jiang *et al.*, 2014). Hence, surface modification of iron oxide NPs would improve their solubility in solvent, affects their interfacial properties, and reduces agglomeration (Šutkaa *et al.*, 2014).

According to Wu *et al.* (2008), curbing agglomeration by means of surface modification would further expand the scope of application. In an achievement of a stable colloidal solution by surface modification, adequate repulsive interaction and compatibility of surfactants with the NPs are essential. Surface coated iron oxide NPs can be divided into three types; oil-soluble, water-soluble, and amphiphilic. An oil-soluble type is coated with generally hydrophobic group such as alkyl phenol and fatty acid (n=6-10, linear or branched). Contrariwise, water-soluble type possesses hydrophilicity characteristic and the surfactants used are such that; ammonium salt, polyol, and lycine. Amphiphilic type is the resultant of surface modification with a surfactant that comprises both hydrophilic and hydrophobic structural regions such as sulfuric lycine (Wu *et al.*, 2008).

Oleic acid has been used regularly as coating agent in the study of surface modification of iron oxide because it has greater affinity to the surface of iron oxide compared to other surfactants (Šutkaa *et al.*, 2014; Khalil *et al.*, 2014; Jiang *et al.*, 2014). Oleic acid has a non-polar hydrocarbon tail and a polar carboxylic acid head group. While the polar head group anchors on the iron oxide surface, the non-polar tail extends into solution, causing iron oxide to become hydrophobic and dispersible in organic solvent (Šutkaa *et al.*, 2014). Besides that, hexanoic acid has also been used as a comparison to oleic acid to study the effect of chain length of the coating agent (Rehana *et al.*, 2015). Table 2.1 summarizes the reported co-precipitation and surface modification parameters with iron oxide properties by several published works

Table 2.1: Reported co-precipitation and surface modification parameters with iron oxide properties by several published works

Reference	Type of salt/ molar ratio (M)	Precipitating agent /conc. or molar ratio (M)	Reaction temp. /time (˚C/min)	Surface coating	Lattice constants (Å)	NPs/FNPs size by TEM (nm)	Magnetic properties	Hydrodynamic size & stability	Phase of iron oxide
Upadhyay *et al.*, 2016	i)$FeCl_3$:$FeCl_2$/2 ii)$FeCl_2$/1 iii)$FeCl_2$/1	i)NaOH/0.75 ii)NaOH:KNO_3/3 iii)NaOH + KNO_3/3	i)0/- ii)100/10 iii)100/120	-	8.397-8.414	i)7.9±0.3 ii)27±3 iii)200±10	SP: < 14 nm M_s:62-87 emu/g H_C: 9.55-163 Oe	-	Fe_3O_4
Mir *et al.*, 2015	$FeCl_3$:$FeSO_4$/2	NH_4OH/NM	25-90/60	Fe^{2+}:phenanthroline 1:0.25-1	-	5-10	M_s: 55 emu/g	-	γ-Fe_2O_3
Rehana *et al.*, 2015	$FeCl_3$:$FeCl_2$/0.7	NH_4OH/NM	NM	i)Ascorbic acid ii)Hexanoic acid iii)Salicylic acid iv)L-arginine v)L-cysteine each: 0.07% v/v	-	26-31	M_s:1.06-2.23 emu/g H_C: 907-16121 Oe	30-195 nm 3.8-21.2 mV	Fe_3O_4
Aliakbari *et al.*, 2015	$FeCl_3$:$FeSO_4$/2	NH_4OH/1.4	80/30	5% v/v oleic acid NH_4OH/1.4M 80˚C /30min	-	18-22	SP M_s: 57 emu/g H_C: 0 Oe	-	Fe_3O_4
Soares *et al.*, 2014	$FeCl_3$:$FeCl_2$/2	NH_4OH /0.56	NM	8-196 mM oleic acid Final pH: 7	-	9-10	SP: at 320 K M_s: 34-45 emu/g H_C: 0 Oe	150-225 nm	Fe_3O_4
Petcharoen & Sirivat, 2012	$FeCl_3$:$FeCl_2$/2.45	NH_4OH/0.56	90/-	0.2-1% v/v oleic acid	~8.390	~10	M_s: 33 emu/g H_C: 26.6 Oe	-	Fe_3O_4
Yang *et al.*, 2010	$FeCl_3$:$FeCl_2$/2	NH_4OH/0.32	80/5	5% v/v oleic acid	-	~20	-	-	Fe_3O_4
Unal *et al.*, 2010	$FeCl_3$:$FeCl_2$/2	37% NH_4OH added until solution; pH 11	90/720	4 M salicylic acid	~8.390	~20	-	-	Fe_3O_4
Ünal *et al.*, 2010	$FeCl_3$:$FeCl_2$/2	NH_4OH added until solution; pH 11	80/360	4 M L-histidine	~8.390	8.5±0.25	M_s: 45.5 emu/g	-	Fe_3O_4

Mir *et al.* (2015) performed co-precipitation method in the synthesis of iron oxide NPs but used 1,10-phenanthroline as ligand instead of oleic acid. It was revealed that both concentration of the ligand and reaction temperature are crucial in achieving the best magnetic FNPs. It goes the same with Rehana *et al.* (2015) whereby the size of particles was reduced from 31 nm to 26 nm as the consequent of coating agent. The size reduction was believed to have been ensued by the prevented agglomeration. Lower magnetization value was also observed for the bare NPs when compared to the coated FNPs. This is most likely because the NPs were more inclined to phase transformation as temperature was increased. Moreover, increasing crystallinity size would likely hike up the saturation magnetization, M_s (Mir *et al.* 2015).

As for the case of two different approaches of ex-situ modifications with oleic acid, it appears that the size of FNPs were smaller when oleic acid was added all at once into the mixture than in the case of when oleic acid was added dropwise into the mixture. Though, the strain observed in the FNPs was more prominent in the first process than in the latter. As a result for the small yield of FNPs and the strain, the M_s was apparently lowered (Aliakbari *et al.*, 2015).

On the other hand, a study conducted by Soares and coworkers (2014) showed that the presence of oleic acid does not significantly affect the physicochemical and magnetic properties of the FNPs except for concentration of oleic acid at 16 Mm. The oleic acid allegedly reduced magnetic moments at the surface of the FNPs due to its diamagnetic contribution. In addition, the presence of oleic acid bilayer would also have just about the same effect upon the magnetic properties of the FNPs and more stable colloidal suspension (Soares *et al.*, 2014).

Petcharoen and Sirivat (2012) had yielded larger oleic acid-coated iron oxide FNPs compared to the bare NPs. Nevertheless, the size of the coated FNPs can be reduced with the increment of reaction temperature. The coated FNPs exhibited superparamagnetism (33 emu/g) at room temperature and displayed encouraging stability over 1 week. Yang *et al.* (2010) on the other hand synthesized bilayer oleic acid-coated iron oxide FNPs at concentration of 5% v/v oleic acid as the modification of the FNPs was performed in an in-situ manner.

2.2 Development of iron oxide NPs on silicon substrate

The development of magnetic NPs/FNPs on the surface of substrate is a significant research topic related to technological applications. Among the materials being studied as a solid support to anchor NPs/FNPs, silicon is particularly attractive. Silicon (Si) has become one of the most essential materials in modern technology and the chemical modification of its surface has gain a lot of attention (Cattaruzza *et al.*, 2005; Li *et al.*, 2015). It is relatively cheap, high purity production and typically, because of the chemical and electrical stability of its interface with oxides (Thissen *et al.*, 2012). The unoxidized crystalline silicon especially, is considered to be an ideal substrate because of the uniformity, and homogeneity of its surface at nanometer scale (Soares *et al.*, 2014).

There have also been intensive studies on fundamental building blocks of inorganic nanoparticles coated with organic layers in nanotechnology (Thissen *et al.*, 2012 & Altavilla *et al.*, 2005) over the years. Their desirable nanoscopic size offers unique optical, magnetic, and conductive properties to quantum confined materials for fabrication of ultrahigh-density magnetic storage media or magneto-optical devices (Altavilla *et al.*, 2005).

According to Terris and Thomson (2005), self-organization quality of the NPs/FNPs is vital for data storage media and spintronic devices. Orthodox methods of nanoscale arrays fabrications are commonly practiced based on lithographic techniques (Altavilla *et al.*, 2005). Whereas unconventional new approaches introduced an application of template-directed construction of nanostructure arrays, which many had focused on the porous aluminium oxide (AAO) template and colloidal crystal template (CCT) template (Zhao *et al.*, 2015). Aside from these, there are numerous ways of promoting self-assembly of NPs/FNPs into ordered arrays (Altavilla *et al.*, 2005).

Researchers had performed various processes including Langmuir-Blodgett (Chen, 2002), spin-coating (Hong *et al.*, 2002), adsorption by dip-coating (Yoon *et al.*, 2004), and electrophoretic deposition (Maenosono *et al.*, 2003) methods. However, fabrication of stable and highly ordered NPs/FNPs over large area of substrate has yet been studied intensively. Improvement on this can be made by designing appropriate organic coatings on the FNPs to obtain strong chemical linkage with the substrate (Pichon *et al.*, 2012; Altavilla *et al.*, 2005; Cattaruzza *et al.*, 2005). Self-assembly that takes place through strong chemical linkage with silicon substrate in particular, can occur either without the presence of native oxide, SiO_2 or in the presence of SiO_2.

2.2.1 Self-assembly without the presence of native oxide, SiO_2

The self-assembly method is one of the most promising approach because of the advantageous structural stabilization by multiple covalent and hydrogen bonds (Altavilla *et al.*, 2005). It was demonstrated that linear-chain-1-carboxylic acids with unsaturated ends are suitable to act as bridges for certain applications on unoxidized silicon substrate through hydrosilylation reaction (Cattaruzza *et al.*, 2005).

Modification of oxide-free Si surface by direct attachment of organic layers to Si is a driving force to this method. This involves chemical removal of the oxide in fluoride solution (aqueous HF) leading to H-terminated Si substrate (Cattaruzza *et al.*, 2005; Thissen *et al.*, 2012). Subsequently, further functionalization process with organically coated FNPs involves transformation of H-terminated Si surfaces into organically functionalized surfaces with formation of Si-X bonds at the interface (Thissen *et al.*, 2012).

It is important to understand that the resulting H-terminated surface is fairly resistant to further chemical attack by HF because of its less polarity. Thissen *et al.* (2012), further emphasized on the significance of relative stability and yet selective reactivity of the H-terminated surface which is the quintessential component of the functionalization process. Degradation of its surface when removed from HF solution and exposed to air is only observed with charge recombination technique and initial oxidation may occur after several hours in some ambient atmospheres.

However, studies on flat and vicinal H-terminated Si(1 1 1) revealed that upon exposure to O_2, NH_3, and H_2O, reaction is only initiated at steps, dependent on step structure particularly on flat terraces at temperature above 300 ^{o}C (Zhang *et al.*, 2001). Thus, H-terminated Si surfaces are completely stable in clean gaseous environment at atmospheric pressures. Degradation in air is only possible in the presence of radicals, ozone or other reactive species that leave the surface inclined to oxidation (Thissen *et al.*, 2012).

The interfacial electrical properties and sensitivity of silicon to oxidation are determined by the quality of deposited monolayer. Specifically, high packing density is crucial in obtaining chemically and electrochemically stable surface. Nevertheless, this criterion is less important for electroactive multilayers and polymers due to their intrinsically less ordered nature. Thus, they normally give the underlying silicon surface better protection against oxidizing species instead (Fabre, 2016). Studies showed that unreactive sites that are susceptible to oxidation after the assembly of long chain linear alkene- and alkyne- were upheld at 45-50% (Wallart *et al.*, 2005; Yuan *et al.*, 2003; Sieval *et al.*, 2001) and 35-40% (Scheres *et al.*, 2011; Scheres *et al.*, 2010) respectively, such that water or oxygen is able to penetrate through the monolayer via defects or pinholes. Consequent to a significant density of electrically active surface defects, electron transfer characteristics of redox-active coated silicon surfaces would be greatly depreciated.

To alleviate this problem, it is crucial to ensure that that the monolayer is as densely packed as possible to encourage a conducive, hydrophobic environment as well as to preserve a low density of surface states. One of the successful approaches to reduce oxidation of underlying silicon is by diluting redox-center-terminated chains with electrochemically inert organic chains. With that, surface coverage of the redox center can be controlled. In addition, both quality and packing density of the resulting redox-active monolayer become liable to improvement (Fabre, 2016).

2.2.1.1 Thermal hydrosilylation

The hydrosilylation of H-terminated Si by alkyl chains is first proposed by Linford and Chidsey (1993) who introduced the attachment of covalent bond, mainly Si-C at the Si(1 1 1) surfaces. The essential element of hydrosilylation is the activation of alkene, alkyne or other unsaturated carbon compounds to allow reaction with the Si-H surface (Thissen *et al.*, 2012; Cattaruzza *et al.*, 2005) as shown below:

$$\equiv \mathrm{Si{-}H} + \mathrm{H_2C{=}CH{-}R} \longrightarrow \equiv \mathrm{Si{-}CH_2{-}CH_2{-}R}$$

Yablonovitch *et al.* (1986), quoted by Fabre (2016) claimed that interfacing technologically imperative semiconducting surfaces for instance, oxide-free hydrogenated-terminated silicon (Si-H) with high quality and stable redox-active films is an engaging policy toward functional devices for charge storage and information processing. Si-H is an appealing substrate for electrical applications because it is easy and reproducible, has definite structure with low density of electrically active surface defects, and its susceptibility to be chemically coated with organic monolayers linked through nonpolar and robust interfacial Si-C bonds (DeBenedetti and Chabal, 2013; Thissen *et al.*, 2012; Li *et al.*, 2012; Cummings, *et al.*, 2011; Ciampi, *et al.*, 2010). Organic/silicon interface which is free from native oxide, SiO_2, constitutes of an almost defect-free electrical interface which allows a direct electronic coupling between surface and organic functionality (Fabre, 2016).

According to Thissen *et al.* (2012), the primary advantage of this method is the formation of thermodynamically and kinetically stable self-assembly of the FNPs, owing to the strength and low polarity of the Si-C covalent bond. Thermal hysrosilylation is based on immersion of H-terminated Si surfaces in an anhydrous solution of suitable alkyl group compounds at temperature of approximately 150-200 ^{o}C (Thissen *et al.*, 2012).

The thermal treatment aids in removing traces water, consequently reducing the possibility of surface oxidation and promotes ordering layer of the FNPs (de Mierry *et al.*, 1990). The Si-C bond is more stable than the H-terminated surfaces once produced due to the protective self-assembly layer, even if 60-70% of the surface is still H-terminated (Thissen *et al.*, 2012).Both alkenes and alkynes were studied for hydrosilylation processes and were quantitatively compared. It was shown that alkynes were more favorably attached over alkenes (Ng *et al.*, 2009).

In a study made by Cattaruzza *et al.* (2005), 10-undecynoic acid is used as a linkage between iron oxide FNPs and silicon surface via thermal hydrosilylation reaction. These molecules bind to silicon surfaces through a covalent Si-C bond. Their free carboxylic end groups was utilized as binding sites for the attachment to other species such as iron oxide NPs (Cattaruzza *et al.*, 2005). At temperature of 5K, the saturation magnetization was displayed at 40 emu/g while coercivity was achieved at 160 Oe.

Altavilla *et al.* (2005) carried out a hydrosilylation process of immobilizing trimethoxy-7-octen-1-yl-silane functionalized iron oxide FNPs on H-terminated Si substrate. The functionalization of the ligand was initiated by a monolayer-exchange reaction which took place between the trimethoxy-7-octen-1-yl-silane and the initially functionalized oleic acid–coated FNPs. The M_s of the functionalized NPs was exhibited at 53.7 emu/g with coercivity of 46.4 Oe (Altavilla *et al.*, 2005).

The development of iron oxide FNPs on Si substrate via thermal hydrosilylation process was not given much attention in the literature. The reported self-assembly method of iron oxide NPs/FNPs on Si substrate by several published works was summarized in Table 2.2.

2.2.2 Self-assembly in the presence of native oxide, SiO_2

For the formation of self-assembled monolayers on silicon dioxide, SiO_2, three classes of molecules, namely silanes ($RSiX_3$, with x = Cl, OMe, OEt), organometallics (RLi or RMgX), and alcohols (ROH), are widely used (R, being the organic constituents) (Miozzo *et al.*, 2010). It was further claimed that the ideal surface for SAM growth is based on a clean oxide layer with high density of silanol groups (Si-OH) which are either used as anchoring sites for silanization or conversion into more reactive functions (i.e. Si-Cl or Si-Net_2) appropriate for alkylation or alkoxylation. Hence, for this purpose, the conventional RCA process and the growth of an ultra-thin (10-15 Å) layer of SiO_2 (thermally fabricated) are normally employed (Miozzo *et al.*, 2010).

In the case of organic thin film transistors reviewed by Miozzo and associates (2010), thick SiO_2 layer is commonly fabricated (thermally grown or sputtered on Si) as gate dielectric while highly doped silicon is used as both substrate and gate electrode at once. According to them, the SiO_2 avoids gate leakage currents and behaves as an effective dielectric for the capacitor. However, despite the fact that the growth of SiO_2

has been optimized to form a defect-free interface by most researchers, its top surface particularly for organic field-effect transistor is much less defined. Depending on the processing history, Si-OH defects might conjure up at the surface, leading to problematic phenomena such as interface trapping and hysteresis. Thus, the fabrication of SiO_2 usually precedes to low mobility and a high degree of variability (Miozzo *et al.*, 2010).

In a work performed by Pichon and colleagues (2012), self-assembly of iron oxide FNPs were executed using alkoxysilanes-based molecules (amine and thymine terminal groups) which resulted in Si-O-Si linkages. The trialkoxysilynated molecules undertook chemical reaction with the silanol groups at the surface of silicon to which the thymine groups experienced faster kinetics immobilization than the amine groups (Pichon *et al.*, 2012). Nevertheless, interfacial siloxane bonds, Si-O-Si, which is often derived from alkylsilane monolayers are prone to hydrolysis (Pujari *et al.*, 2014; Herzer *et al.*, 2010; Onclin *et al.*, 2005). Thus, its long-term applicability surface remains lower than the unoxidized, covalently coated silicon.

2.3 Iron oxide for metal-oxide-semiconductor (MOS) capacitor

Spinel ferrites, XFe_2O_3 constitutes a broad group of materials, where X is a trivalent transition metal ion and Fe ion is divalent. Fe_3O_4 particularly is conductive at room temperature due to a hopping mechanism. To date, the research of iron oxide as thin film and the application of this material as metal oxide semiconductor capacitor are not well-rounded because of their complex crystal structure with big unit cell and many unoccupied interstitial sites. Iron oxide thin film with its bulk properties is desirable, however it is difficult to be achieved (Cibert *et al.*, 2005).

The distribution of the Fe^{2+} and Fe^{3+} ions in the tetrahedral and octahedral sites influence the magnetic and transport properties of iron oxide. The properties of its thin film can differ significantly from the bulk, dependent strongly on deposition technique during development on substrate. It was clarified that the actual thin film of Fe_3O_4 possessed spin polarization comparable to ferromagnetic metals (Cibert *et al.*, 2005).

2.3.1 Oxide breakdown

Large enough electric field applied to the oxide layer would impose oxide breakdown which then lead to catastrophic failure. A gate voltage of approximately 30 V would produce breakdown in an oxide with thickness of 500 Å. However, a safety margin of a factor 3 is common. Hence, oxide thickness of 500 Å would have maximum safe gate voltage of 10 V. Since there may be defects in the oxide that may lower the breakdown field, safety margin is necessary (Neamen, 2012, p. 464).

The leakage current density-electric field (J-E) characteristics can be transformed from current-voltage (I-V) measurement. In order to rectify contact with an n-type semiconductor, electron was allowed to be transported over the potential barrier (Neamen, 2012, p. 404). Barrier height ϕ_B of conduction band edge between silicon and interfacial layer of oxide was extracted from Fowler-Nordheim (FN) tunneling model. The J ascribed to FN tunneling (J_{FN}) is shown in the following equations (Schroder, 2006):

$$J_{FN} = AE^2 \exp(-B/E) \tag{2.4}$$

Where,

$$A = (q^3/8\pi h\phi_B)/(m/m_{ox}) \tag{2.5}$$

and

$$B = \left[8\pi(2m_{ox}\phi_B^3)^{1/2}\right]/3qh \tag{2.6}$$

Where h is Planck constant (4.135 x 10^{-15} eV s), m_{ox} is effective electron mass in the oxidized layer, m is free electron mass. Substituting all constants into Equations 2.5 and 2.6 gives:

$$A = 1.54 \times 10^{-6}(m/m_{ox}\phi_B) \qquad 2.7$$

Where m/m_{ox} is assumed to be 0.3, and

$$B = 6.83 \times 10^{7}(m_{ox}\phi_B^3/m)^{1/2} \qquad 2.8$$

Rearranging Equation 2.4 yields:

$$\ln(J_{FN}/E^2) = \ln(A) - B/E \qquad 2.9$$

Equation 2.9 is an interpretation of a linear equation to which FN tunneling model was plotted. Where $\ln(J_{FN}/E^2)$ is the y-axis variable, $1/E$ is the x-axis variable, B is the gradient, while $\ln(A)$ is the y-intercept. Substituting the gradient and y-intercept from the graph of the FN tunneling model into Equation 2.7 and 2.8 will enable attainment of the ϕ_B.

Clark and Robertson (2007) evaluated barrier height of $BiFeO_3$ against various metals using the model of metal induced gap states (MIGSs). Their material was estimated to be over 0.9 eV. Whereas its band gap was calculated by the density-functional based screened exchange method at 2.8 eV (Clark and Robertson, 2007).

2.3.2 Electrical properties of surface coated-iron oxide FNPs

In a study conducted by Petcharoen & Sirivat (2012), electrical conductivity of 1.3×10^{-3} S/cm was obtained for bare iron oxide NPs which can be referred to a semiconducting material. The electrical conductivity of the NPs appeared 2-5 times larger than the oleic-acid coated FNPs because the oleic acid coating on the surface of the FNPs might have obstructed the electron transfer between each particle. Apart from that, as the particle size increased, the electrical conductivity was decreased due to the loose aggregation of larger FNPs. The lousy arrangement and poor packing efficiency of larger FNPs evoked a decline in contact area for the electron transferring (Petcharoen & Sirivat, 2012).

Fe_3O_4 FNPs coated with L-Histidine was synthesized by Ünal *et al.* in 2010. The *ac* conductivity of the FNPs displayed a temperature dependent behavior at high frequencies corresponding to ionic conductivity. Whereas *dc* conductivity was conformed to the Arrhenius plot with activation energy of 0.934 eV. Apart from that, permittivity measurements revealed increasing dielectric constant with increasing temperature which is fairly expected in semiconducting materials (Ünal *et al.*, 2010).

The same goes to another study conducted by Unal and coworkers in 2010 where the FNPs are of polycrystalline in nature. Both interactions between the FNPs and the coating agents in mentioned studies were constituted of carboxylate oxygen attachment (Ünal *et al.*, 2010; Unal *et al.*, 2010). According to Unal *et al.* (2010), the saliycyclic coated Fe_3O_4 initially formed a random network but the FNPs became more organized when temperature was increased steadily.

Another study conducted by Kavas *et al.* (2010) revealed that Fe_3O_4 aggregated upon PVTri coating. Glass transition temperature effect of the polymer was suspected for the conductivity and permittivity measurements. Moreover, this nanocomposite was claimed to be suitable for inductive and capacitive application as well as microwave absorbers as sharply reduced dielectric loss was revealed (Kavas *et al.*, 2010).

Table 2.2: Reported self-assembly method of iron oxide on Si substrate by several published works

Reference	Iron oxide	Method	Coating materials	Solvent	Reaction temp. /time (˚C/min)	Annealing (˚C/min)	NPs/FNPs size (nm)	Thickness of NPs/FNPs (nm)	Magnetic properties	Surface roughness (nm)
Singh *et al.*, 2015	Fe_3O_4	Monte Carlo simulations	Oleic acid	Hexane	-	-	~13	Assembled in one-dimensional filament, helices and C-shaped	~96 emu/cm^3	-
Cattaruzza *et al.*, 2005	Fe_3O_4	Hydrosilylation	Oleic acid 10-undecynoic acid	Mesitylene	180/120	-	5	5 nm- single layer 10.5 nm- bilayer	Temp: 5K; M_s: 40 emu/g H_C: 160 Oe	-
Pichon *et al.*, 2012	Fe_3O_4-γ-Fe_2O_3	Dip-coating (ultrasonic)	Oleic acid i) APTES ii) THY	THF	RT/i) 10; ii) 90	-	~10	9 nm	SP at 300 K Temp: 5K; H_C: 170 Oe	2.2
Benitez *et al.*, 2010	γ- Fe_2O_3	Spin coating	Oleic acid	Toluene	-	i) 170	20	-	SP	-
Lu, 2006	Fe_7SiO_{10}	Dip-coating	-	-	96/60	-	~10	20 nm- SiO_2 60 nm- Fe_7SiO_{10}	-	-
Cao *et al.*, 2005	NM	Dip-coating	-	-	5	500/15	~10	-	-	-
Altavilla *et al.*, 2005	Fe_3O_4	Hydrosilylation	Oleic acid Trimethoxy-7-octen-1-yl-silane	Toluene	NM/60	-	7	-	Temp: 2.5 K; M_s: 53.7 emu/g H_C: 46.4 Oe	-
Prabhakaran *et al.*, 2003	Fe_2O_3	Dip-coating (ultrasonic)	-	Ethanol	NM	400 & 750	10	-	-	-

CHAPTER 3: METHODOLOGY

3.1 Introduction

The methodology is divided into two parts; i) synthesis and ii) self-assembly of the functionalized Fe_3O_4-γ-Fe_2O_3 nanoparticles (FNPs) on SiO_2/n-Si structure. Several morphological and electrical characterizations were performed on the synthesized and self-assembled FNPs. Figure 3.1 and 3.2 give overviews of the methodology in schematic flow charts representing part i and ii respectively.

3.1.1 Synthesis

In the first part, synthesis of bare iron oxide NPs was performed by co-precipitation method. Iron oxide NPs in this paper were synthesized by co-precipitation because the process is organic solvent-free (Tangwatanakul *et al.*, 2017; Lin *et al.*, 2017). Surfaces of the bare NPs were ex-situ coated with different concentrations of oleic acid and a fixed concentration of 4-pentynoic acid.

3.1.1.1 Materials

All chemicals were of analytical grade (purity>99%) and were used without further purification. Iron (II) chloride tetrahydrate ($FeCl_2 .4H_2O$), Iron (III) chloride hexahydrate ($FeCl_3 .6H_2O$), and ammoniun hydroxide (NH_4OH) 28% were purchased from Merck. Whereas oleic acid, 4-pentynoic acid, hexane (99%) and ethanol (90%) were purchased from Sigma-Aldrich. Deionized water was used as solvent and for rinsing purpose.

3.1.1.2 Synthesis of bare NPs

In the first part, bare and functionalized iron oxides were synthesized. Initially, 50 ml deionized water was added in a beaker and heated to 60 ˚C. Then, $FeCl_2.4H_2O$ and $FeCl_3$.6H2O were added into the beaker with molar ratio of 1:1.5. The mixture was mechanically stirred at 500 rpm. While the mixture was continuously stirred at 500 rpm (60 ˚C), 350 ml of 3 M NH_4OH was added gradually at 20 ml/min using a burette. The initial brownish precipitation gradually turned black throughout the process. The black precipitation was assumed to be magnetic iron oxide.

After all of the NH_4OH had drained into the beaker, the mixture was kept stirred at 500 rpm (60 ˚C) for 1 hour. Next, the magnetic iron oxide was allowed to settle down to the bottom of the beaker. The NH_4OH was decanted and the precipitate was washed with 2 L deionized water. Commercial magnets were stacked together on a base where the beaker was placed onto it. This allowed attraction between the magnets and the black magnetic precipitate which consequently kept the precipitate to settle at the bottom of the beaker while excess water was decanted. Sample which was labelled as IO is the bare iron oxide NPs that was used as a control, stored in slurry form at 4 ˚C to minimize oxidation rate of the NPs. Table 3.1 summarized the first part of methodology.

3.1.1.3 Synthesis of FNPs

First of all, the bare IO NPs was altered to pH 12 by adding corresponding amount of NH_4OH. Then, for 15 g total solid content of the bare iron oxide slurry, oleic acid was added at concentration of 0.2, 0.4, 0.6, and 0.8 g/g oleic acid to iron oxide. The mixture was stirred with glass rod to allow thorough coverage of oleic acid onto the surface of the iron oxide NPs. More excess water was decanted from the slurry after the addition of oleic acid. The iron oxide was also washed with ethanol, followed by hexane to remove any excess oleic acid. Sample labelled as 0.8 is another control that was ex-situ coated with only oleic acid, intended to compare with another sample of similar concentration of ex-situ oleic acid-coated iron oxides NPs but was functionalized with 4-pentynoic acid. This concentration was preferred because preliminary test showed that, zeta potential of 0.8 g/g oleic acid to iron oxide was established at the greatest hydrodynamic stability (-62.01 ± 0.03 mV) compared to the other concentrations. Greater hydrodynamic stability encourages higher chances for a successful functionalization of surfactants (Jiang *et al.*, 2014).

Next, each 5 g total solid content of 0.2, 0.4, 0.6, and 0.8 g/g oleic acid to iron oxide slurry was placed into separate beaker. Each was added with a fixed amount of 1.63 mmol 4-pentynoic acid. The mixture was heated at 60 ˚C under nitrogen gas, N_2 and was continuously stirred for 10 hours to allow a complete functionalization of the 4-pentynoic acid with the iron oxide FNPs. The 4-pentynoic acid was chosen because it has terminal alkyne that would bond with SiO_2 and form linkages with the NPs. The terminal alkyne is the prime mover to the self-assembly that was anticipated between the FNPs and the SiO_2. Samples labelled P-0.2, P-0.4, P-0.6, and P-0.8 were the final products of the ex-situ oleic acid-coated iron oxide NPs, functionalized with 4-pentynoic acid. After the samples were left to cool, they were stored at 4 ˚C in slurry form. Before the samples were used for self assembly and characterizations purpose, they were ensured to be in a condition of pH 12.

3.1.2 Self-assembly of FNPs on SiO_2/n-Si structure

In the second part, self-assembly of the functionalized Fe_3O_4-γ-Fe_2O_3 FNPs was performed. SiO_2 was grown on the surface of Si substrate with the applied heat treatment during the self-assembly through thermal oxidation process. The FNPs were self-assembled on top of the SiO_2.

Initially, 1 x 1 cm^2, n-type, (100)-oriented, 1–10 Ω cm Si substrates were cleaned by Standard Radio Corporation America (RCA) cleaning procedures. Right after that, 3 µL of the functionalized NPs were drop casted onto the substrates using a micropipettor (2-20 µL, Eppendorf). The sample was then heated up in a Carbolite CTF tube furnace with 10 °C/min heating rate and 150 mL/min argon gas flow rate at different temperatures of 70 °C, 150 °C, 200 °C, and 300 °C for 60 min. Heating at stated temperature range was meant to observe any consequences to the surface of substrate as well as morphological and electrical characteristics of the FNPs film.

Table 3.1: Summary of the first part methodology (synthesis)

Sample ID	Concentration of oleic acid to iron oxide (g/g)	Functionalization of 4-pentynoic acid (1.63 mmol)
IO	0.0	x
0.8	0.8	x
P-0.2	0.2	√
P-0.4	0.4	√
P-0.6	0.6	√
P-0.8	0.8	√

Remarks: x – Not applied √ - Applied

3.1.3 Characterizations

Morphology of samples IO, 0.8, P-0.2, P-0.4, P-0.6, and P-0.8 which were synthesized in the first part were characterized by PANalytical Empyrean X-ray diffractometer (XRD) with CuKα (1.5406 Å) as radiation source in a scanning range of 2θ=20˚-70˚. Transmission electron microscopy (TEM) of LIBRA machine Model 120, TEMeCarl Zeiss, was used to take TEM images of only the as prepared sample P-0.4. Thermal decomposition analysis was also implemented using a simultaneous Thermogravimetric and Differential Thermal TGA/SDTA851 Ultramicro Balance (Mettler Toledo). Mass loss was monitored from room temperature to approximately 980 ˚C under N_2 gas flow. Meanwhile, functional groups were characterized by Fourier transform infrared spectroscopy (FTIR) spectrometer (Bruker Tensor27) in the range of 400 to 4000 cm^{-1}. Zetasizer Nano ZS analyzer (ZEN 3500, Malvern) was employed to investigate dispersibility of the NPs in aqueous medium via hydrodynamic particle size distribution (PSD), and zeta potential (ZP).

Morphology of the as prepared films which were self-assembled at 70, 150, 200, and 300 ℃ in the second part were characterized using PANalytical Empyrean X-ray diffractometer (XRD) with CuKα (1.54 Å) as radiation source in a scanning range of $2\theta=20^{\circ}-70^{\circ}$ operating at 45 kV and 40 mA. Phase confirmation was executed using Horiba XploRA Raman microspectrometer with 532 nm excitation of an Ar+ laser source with maximum output power of 60 mW. The spectra were collected using 6 mW laser power with laser spot less than 2 µm and 20 s exposure time in a spectral range of 200-1000 cm^{-1}. Functional groups that existed were determined by Bruker Tensor27 Attenuated Total Reflectance Infrared (ATR-IR) spectrometer in the range of 400-4000 cm^{-1}. Linear baseline correction was slightly applied.

Magnetic properties of bare Fe_3O_4-γ-Fe_2O_3 NPs, functionalized Fe_3O_4-γ-Fe_2O_3 FNPs, and the deposited Fe_3O_4-γ-Fe_2O_3 FNPs film on Si substrate were measured at room temperature (298 K) using a Lake Shore Model 736 VSM Controller vibrating sample magnetometer (VSM).

Surface characterizations concerning distribution of the FNPs and thickness of the film were analyzed by Ultra-high Resolution Scanning Electron Microscope SU8040 Field Emission Scanning Electron Microscope (FE-SEM) with an accelerating voltage of 5 kV. Surface topography and root-mean-square roughness were examined by Hitachi AFM5100N atomic force microscopy (AFM) with dynamic force mode (DFM); 1 µm × 1 µm scanned surface areas.

Electrical characterization of the as prepared film was investigated by fabricating MOS capacitor test structures with defined square area of 9 x 10^{-4} cm^{2} (0.03 cm ×

0.03 cm). 100 nm-thick aluminium (Al) (Kurt J. Lesker, USA, 99.9995 % purity) was sputtered on top of the film using TF 450 physical vapour deposition RF sputtering system. The same thickness of Al film was sputtered on the backside of the Si substrate, serving as Ohmic back contact. BPW-800 8" probe station along with Keithley 4200 semiconductor characterization system were used to conduct the current–voltage measurements. The resultant MOS structure of the fabricated device is shown in Figure 3.3.

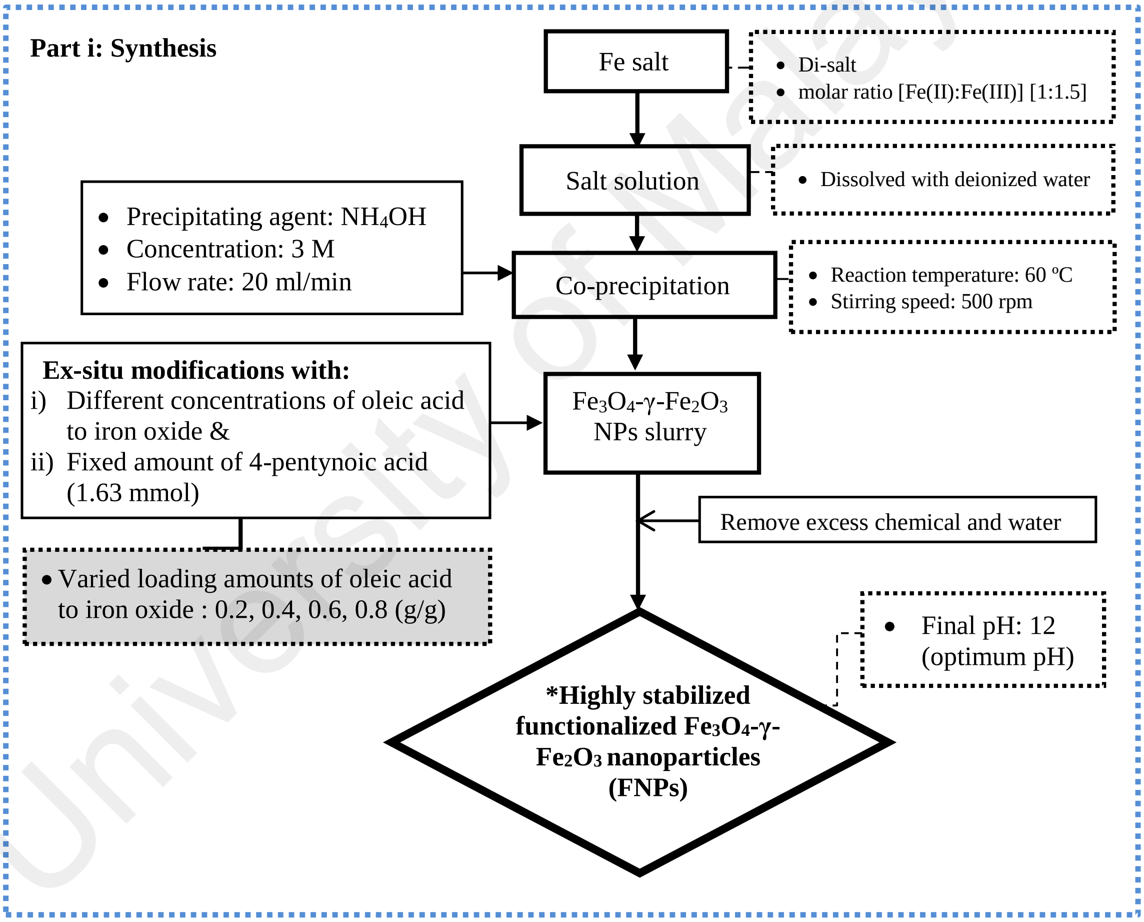

Figure 3.1: Flow chart of methodology (part i)

Remarks:
▨ Parameters that were varied.
***** Characterized by XRD, TGA-DTA, FTIR, Zetasizer » **Objective 1**.

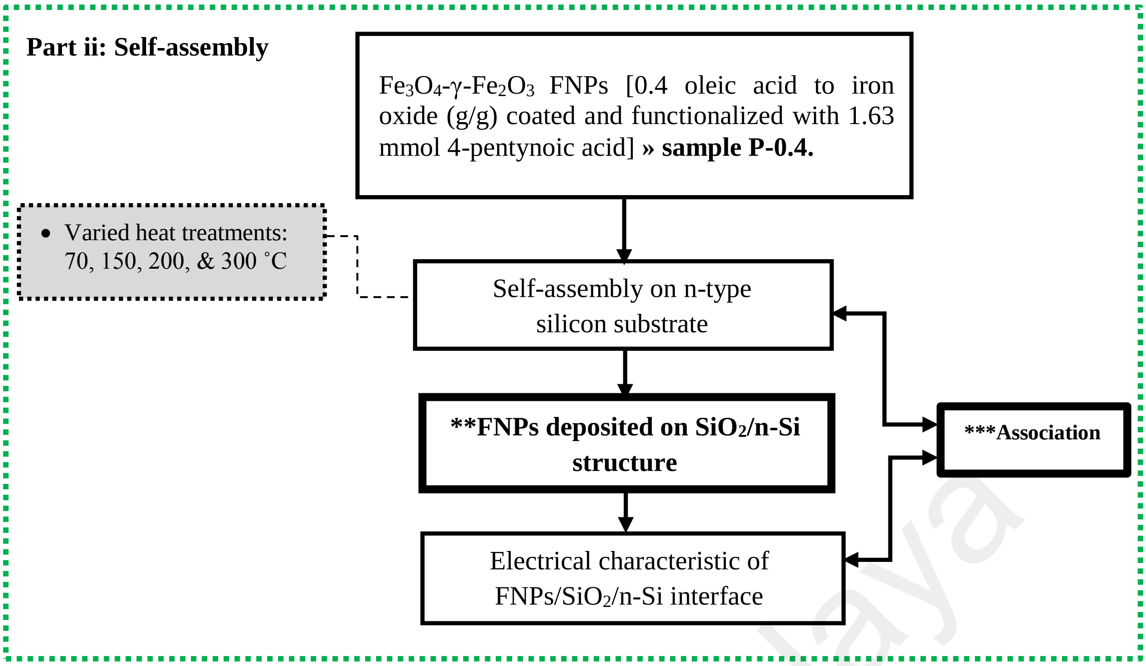

Figure 3.2: Flow chart of methodology (part ii)

Remarks:

▨ Parameters that were varied.

** Characterized by XRD, Raman, ATR-IR, VSM, AFM, & FE-SEM » **Objective 2**.

*** Characterized by semiconductor parameter analyzer (current-voltage (I-V) measurement) » **Objective 3**.

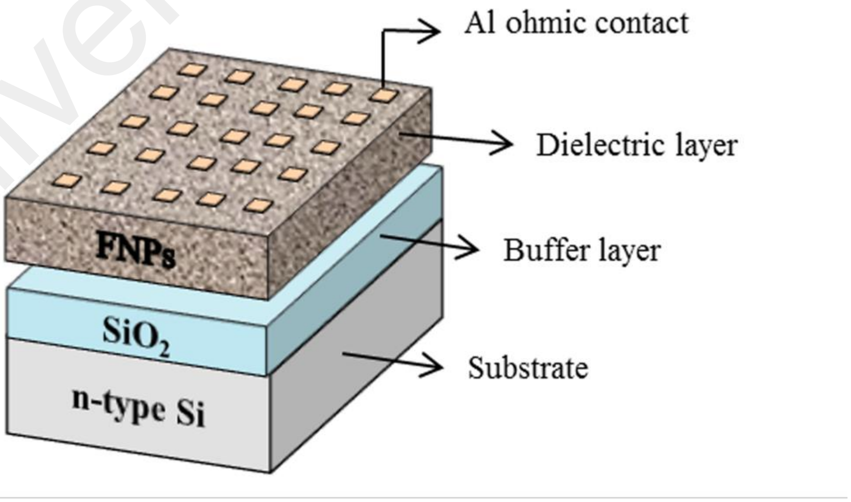

Figure 3.3: The fabricated Fe_3O_4-γ-Fe_2O_3 FNPs/SiO_2/n-type Si structure

CHAPTER 4: RESULTS AND DISCUSSION

4.1 Introduction

This chapter is divided into two parts; the synthesis of functionalized Fe_3O_4-γ-Fe_2O_3 nanoparticles (FNPs) and self-assembly of the FNPs on SiO_2/n-Si structure.

4.1.1 Synthesis of FNPs

The first part discusses on microstructural study, thermal decomposition analysis, functionalization of surfactants, hydrodynamic particles size distribution and stability in polar basic medium, as well as mechanisms of the synthesized FNPs.

4.1.1.1 Microstructural study

Figure 4.1 shows XRD patterns of the iron oxides NPs and FNPs. All peaks of the six samples showed compatible match to that of the standard Fe_3O_4 XRD diffraction (JCPDS Card #19-0629) (Li *et al.*, 2015). Six characteristic peaks corresponding to diffracting planes (2 2 0), (3 1 1), (4 0 0), (4 2 2), (5 1 1), and (4 4 0) were observed in the patterns which are in agreement with magnetite crystal with a cubic spinel structure (Jiang *et al.*, 2014; Castelló *et al.*, 2015).

According to Jiang *et al.* (2014), analysis of the whole pattern fitting approach in which all peaks contribute to determine the crystallite mean size is more reliable than the “single peak” approach. Hence, in this analysis, all peaks obtained were considered in the calculations to determine not only mean crystallite size, *D*, but also mean lattice constant, *a*. The peaks were profile fitted with pseudo-Voigt profile shape function using HighScore Plus (version 3.0). The lattice constants, *a*, were calculated using cubic geometry Equation 4.1, where a is the lattice constant (Å), and d_{hkl} is the interplanar spacing between two closest parallel planes with the same Miller indices, h k l (Å) (calculated from the Bragg's equation, $\lambda = 2d \sin\theta$).

$$a = \mathrm{d}_{hkl} \sqrt{h^2 + k^2 + l^2} \qquad 4.1$$

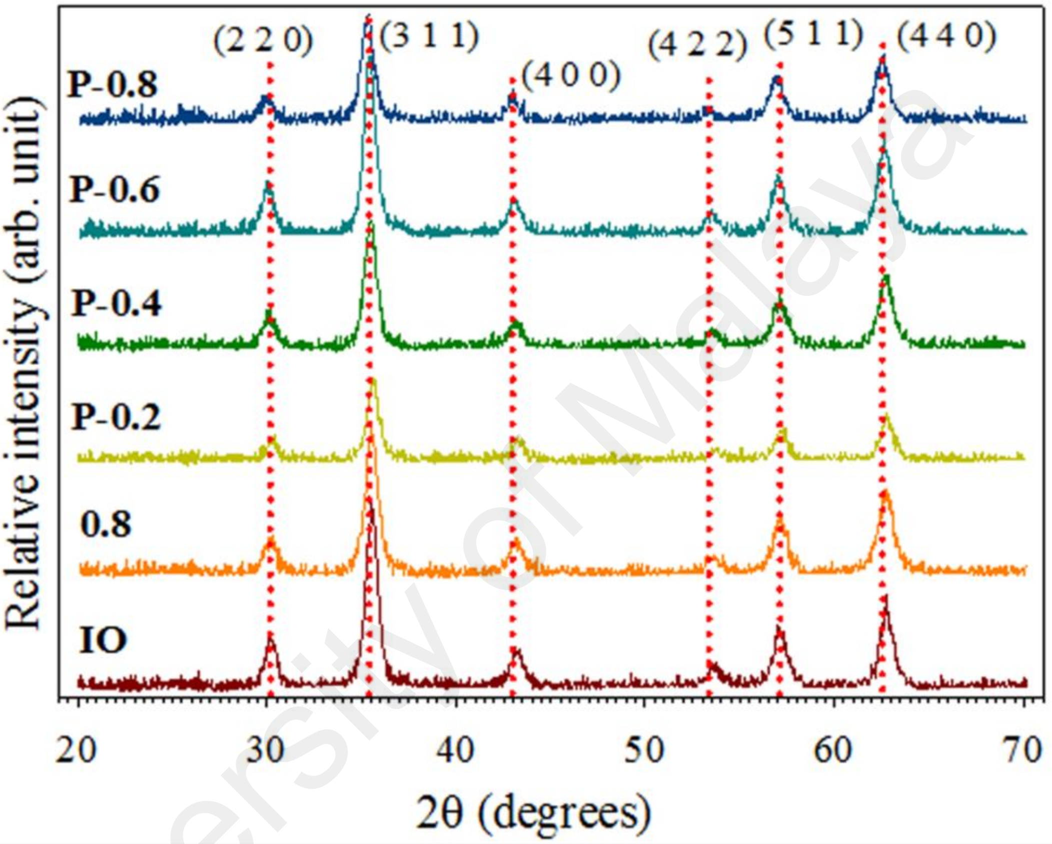

Figure 4.1: XRD patterns of the samples

According to Mote *et al.* (2012), breadth of the Bragg peak is not only contributed by sample but also by instrument. Thus, diffraction pattern from the line broadening of standard LaB_6 was collected to determine the instrumental broadening. Subsequently, Equation 4.2 was used for instrumental broadening corrections. Debye-Scherrer Equation 4.3 was used to estimate crystallite size with K = 0.9 and width at half-maximum peak represented as β_{hkl}. Table 4.1 shows the mean crystallite sizes of the samples.

$$\beta_{hkl} = \sqrt{(\beta_{hkl})^2{}_{observed} - (\beta_{hkl})^2{}_{instrument}} \tag{4.2}$$

$$D = \mathrm{K}\lambda/(\beta_{hkl}\cos\theta) \tag{4.3}$$

Table 4.1: Mean lattice constants and mean crystallite sizes of the samples

Sample	OA/IO (g/g)	4-pentynoic acid (1.63 mmol)	Mean crystallite size, D (nm ± $\sigma_{\bar{x}}$)
IO	0.0	x	10.3 ± 1.3
0.8	0.8	x	9.0 ± 0.4
P-0.2	0.2	√	14.5 ± 2.2
P-0.4	0.4	√	9.7 ± 0.7
P-0.6	0.6	√	11.1 ± 0.6
P-0.8	0.8	√	9.6 ± 2.0

Remarks: x – Not applied √ - Applied

Fig. 4.2 shows Transmission Electron Microscopy (TEM) image of the as prepared sample P-0.4 and particle size distribution calculated from the image. Other than because sample P-0.4 was successfully functionalized with 4-pentynoic acid, it was chosen for TEM characterization due to the highest hydrodynamic stability it able to sustain, justified by its highest zeta potential (ZP) at approximately -75 mV and its narrowest particle size distribution (PSD) at 35.68 nm compared to the other samples as seen in Fig. 7. The attained mean particle size of sample P-0.4 at 10.94 ± 0.24 nm from TEM analysis is complementary to the mean crystallite size of sample P-0.4 at 10 ± 1 nm obtained from XRD.

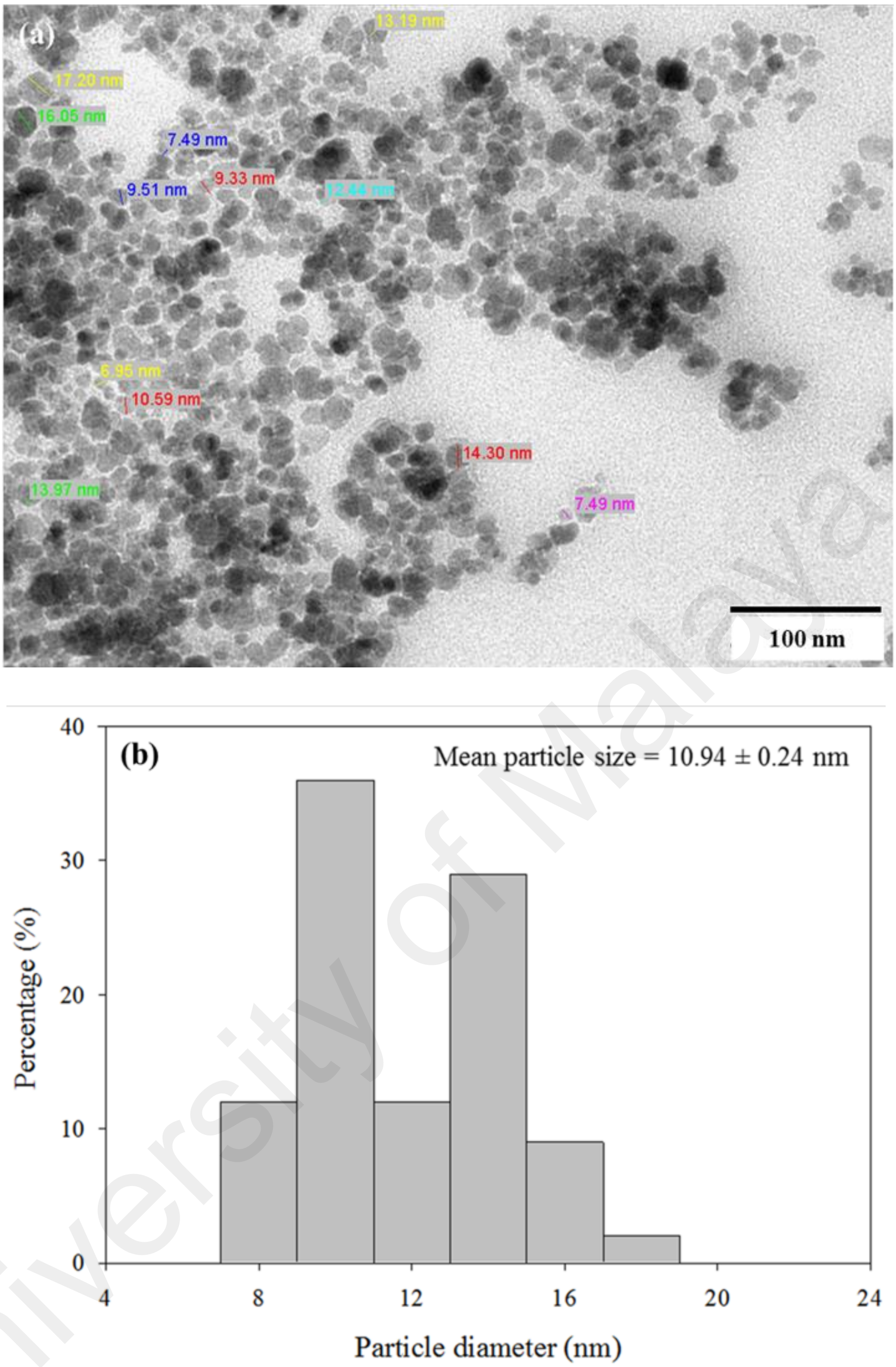

Figure 4.2: (a) TEM image of the as prepared sample P-0.4. Magnification 31,500 x (b) Particle size distribution calculated from TEM image of the as prepared sample P-0.4

4.1.1.2 Thermal decomposition analysis

Thermal decomposition analysis was carried out using Thermogravimetric and Differential thermal analysis (TGA-DTA) at a range of room temperature to approximately 980 ˚C. Figure 4.3 (a) shows TGA and DTA curves aimed at distinguishing the bare iron oxides NPs with the oleic acid-coated FNPs as well as the one that was functionalized with both oleic acid and 4-pentynoic acid. Meanwhile, Figure 4.2 (b) is intended to investigate the influence of different concentrations of oleic acid-coated iron oxide FNPs. Both of the bare iron oxide NPs (sample IO) and the iron oxide FNPs coated by the least concentrated oleic acid (sample P-0.2) demonstrated two steps of weight loss which are indicated by I and II. Meanwhile, samples 0.8, P-0.4, P-0.6, and P-0.8 displayed three steps weight losses which are indicated by I, II, and III.

Previous studies had reported the first weight loss observed below 200˚C as the dissipation of water and other solvents (Castelló *et al.*, 2015; Ang *et al.*, 2014; Petcharoen & Sirivat, 2012). In this study, the first weight loss for bare iron oxide was accounted for hydroxyl group (OH) of water, functionalized to the bare iron oxide NPs; a repercussion of insufficient recrystallization of the NPs (Yang *et al.*, 2010; Qian *et al.*, 2008). On the other hand, first weight losses of the coated FNPs signify the elimination of solvents (residual ethanol and hexane). All samples revealed endothermic reactions at this stage. Exceptionally, the bare iron oxide NPs was also accompanied by an exothermic event at about 140˚C. At such particular temperature, the bare iron oxide is believed to have endured a phase transformation into maghemite (γ-Fe_2O_3) with a slight 1% weight gain.

At the second stage of weight loss, the bare sample IO was subjected to a uniformly continuous phase transformation into hematite (α-Fe_2O_3) corresponding to a steady exothermic peak as temperature elevated from approximately 220˚C to 540˚C despite the insignificant weight gain. Besides, the slight bump at about 560˚C is an indication of γ-Fe_2O_3-α-Fe_2O_3 recrystallization (Yousefi *et al.*, 2013). The sudden drop of DTA at 580˚C onwards shows that sample IO experienced decay of its NPs.

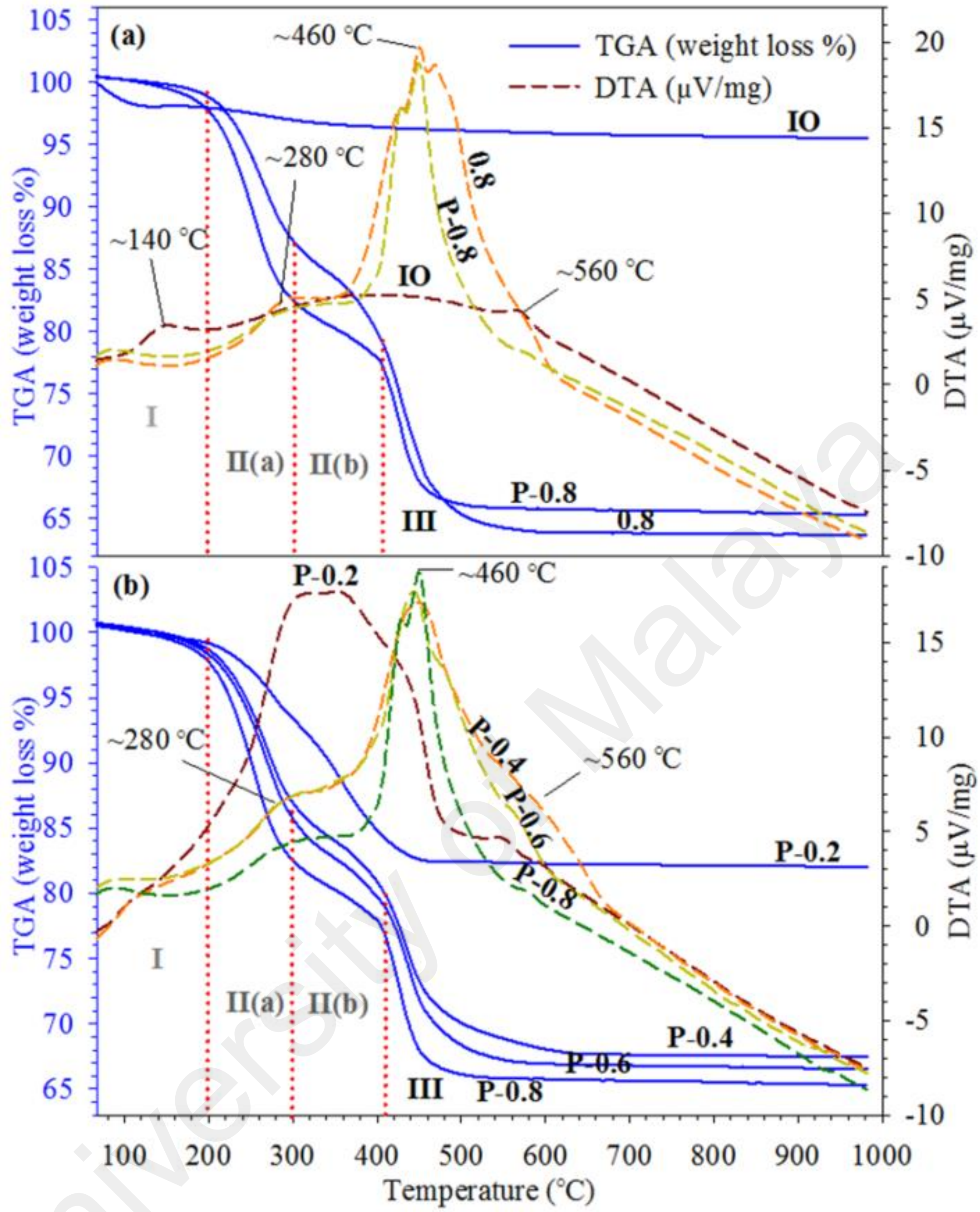

Figure 4.3: TGA and DTA of (a) IO, 0.8 and P-0.8. (b) different concentrations of oleic acid-coated iron oxide FNPs

In the case of coated iron oxides, the weight loss is split into two divisions of surfactants decompositions; II(a) and II(b). Previous studies proposed chemisorption and physisorption of oleic acid at the surface of iron oxides, representing primary layer and secondary layer respectively (Petcharoen & Sirivat, 2012). While the primary layer oleic acid formed ionic bonding between its COO^- and Fe^+ of the iron oxide, the secondary layer oleic acid formed interpenetration layer with the tails of the primary layer (Yang *et al.*, 2010). As a result, two separated weight losses were observed corresponding to the secondary layer and primary layer of the oleic acid. In this study, the first weight loss division, II(a) was observed between 200-300˚C attributed to the decomposition of physisorbed secondary layer oleic acid whereas the second weight loss division, II(b) was reckoned as the decomposition of chemisorbed primary layer oleic acid between 200-400˚C. Comparable observations were also observed by Yang *et al.* (2013). From the thermal analysis, plausible chemical structures for both of the NPs and FNPs can be anticipated as shown in Figure 4.4.

Nevertheless, among the coated iron oxides, only sample P-0.2 ruled out the notion of the two steps weight loss of surfactants suggesting that sample P-0.2 was coated merely with primary chemisorbed oleic acid. Hence, this occurrence proposes that only at certain sufficient concentration of oleic acid would the bilayer of oleic acid form. Furthermore, at this stage of weight loss, an exothermic reaction at approximately 280˚C was acknowledged for the transformation of the coated iron oxides into γ-Fe_2O_3 phase despite the unobserved associated weight gain (Castelló *et al.*, 2015). This might be due to significant weight loss of the surfactants.

Sample P-0.2 behaved differently from other coated samples as its broad exothermic peak extended from 280˚C to 460˚C with a small weight gain. Besides, as sample P-0.2 was surrounded by limited concentration of oleic acid, decaying of its iron oxide FNPs occurred at about the same temperature range of its surfactant decay. Sample P-0.2 exhibited recrystallization of its FNPs at ~560˚C similar to sample IO and was annihilated soon after.

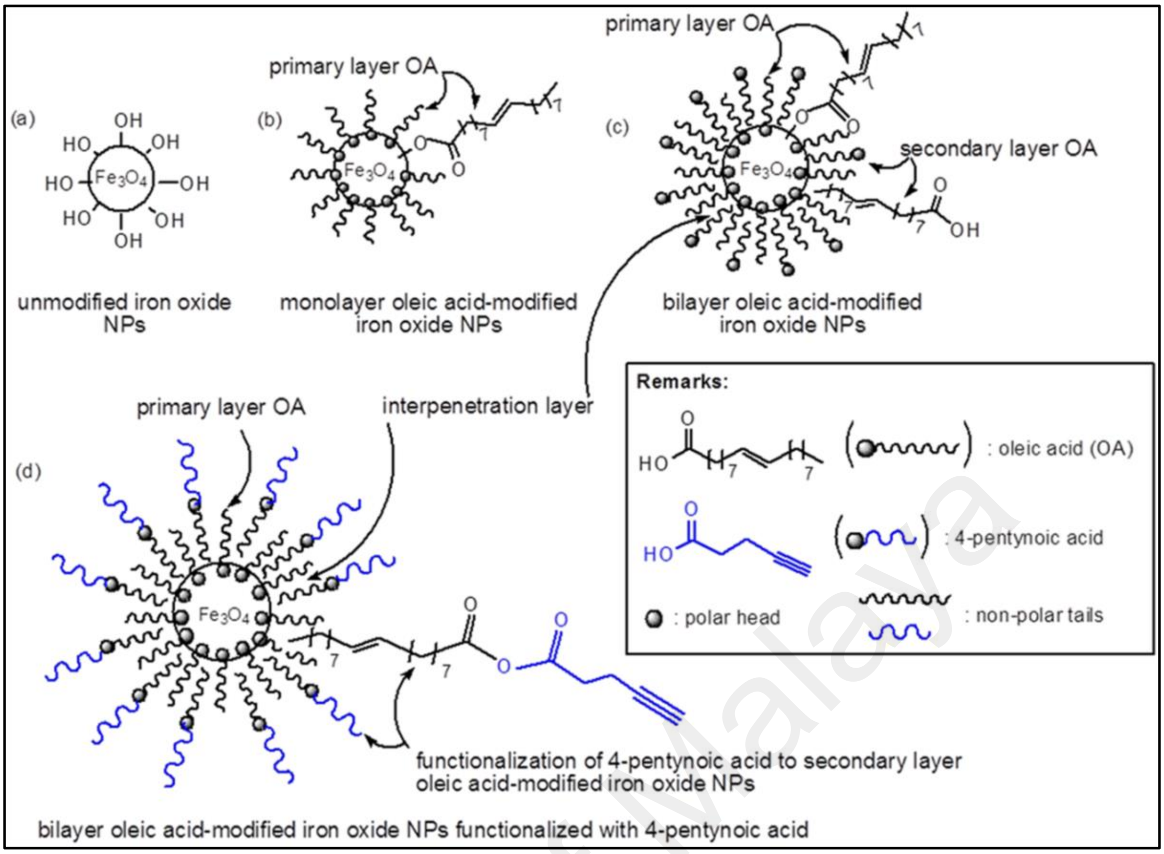

Figure 4.4: Illustrations on (a) bare iron oxide NPs (b) monolayer oleic acid-coated iron oxide FNPs (c) bilayer oleic acid-coated iron oxide FNPs (d) bilayer oleic acid-coated iron oxide FNPs functionalized with 4-pentynoic acid

In addition, the weight loss of surfactants for sample P-0.2, P-0.4, P-0.6 and P-0.8 were accounted at escalating concentration of 16%, 19%, 20% and 22% respectively. The proportional increment of weight loss percent to the increasing concentration of oleic acid coating evidently justified that diverse concentration of oleic acid was indeed successfully functionalized to the bare NPs. Consequently, the concentration of oleic acid functionalized to the Fe_3O_4-γ-Fe_2O_3 influenced the magnitude of the FNPs phase transformation. More substantial concentration of oleic acid functionalized to the iron oxide would better impede the phase transformation. This theory is proven most suggestively by sample P-0.8 (most concentrated oleic acid-coated FNPs) which exhibited the least phase transformation compared to the rest of the coated samples.

In contrast, sample P-0.2 (least concentrated oleic acid-coated FNPs) revealed the most extensive phase transformation. The third stage of weight loss was displayed by the sufficiently oleic acid-coated iron oxide FNPs which exhibited significant deterioration of FNPs supplemented by phase transformation into α-Fe_2O_3 at ~460˚C. The FNPs recrystallization magnitude of γ-Fe_2O_3-α-Fe_2O_3 displayed inverse relationship with the concentration of oleic acid at ~560˚C. This occurrence suggests that the presence of oleic acid hampers the recrystallization of the FNPs as well.

On top of that, to facilitate the understanding of 4-pentynoic acid functionalization on the iron oxide via oleic acid, weight loss percent difference of the surfactant between samples 0.8 (17%) and P-0.8 (22%) was considered. Even though both samples were ex-situ coated with the same concentration of oleic acid, sample P-0.8 experienced 5% more weight loss than sample 0.8. Thus, this finding suggests that 4-pentynoic acid was indeed functionalized to the iron oxide via oleic acid (Figure 4.4 (d)).

4.1.1.3 Functionalization of surfactants

Functionalization of surfactants was analyzed using FTIR to investigate potential bonding characteristics that occurred between the Fe_3O_4-γ-Fe_2O_3 FNPs and the surfactants. FTIR spectra of the NPs and FNPs are shown in Figure 4.5.

According to Waldron (1955), bands between 800-250 cm^{-1} are assigned to vibrations of ferrite ions inside the tetrahedral sites of its inverse spinel structure. All samples confirmed vibration of Fe^{3+}-O bond at observe bands of approximately 540-570 cm^{-1} (Petcharoen & Sirivat, 2012; Li *et al.*, 2015). Bands at 540 cm^{-1} were spotted for the bare iron oxide, sample IO and the least concentrated oleic acid-coated iron oxide FNPs, sample P-0.2.

However, as the concentration of oleic acid was increased, blue shifts of this bond (549 cm^{-1}, 550 cm^{-1}, and 570 cm^{-1}) were observed. This occurrence can be associated to the increasing movements of magnetic ions into the tetrahedral sites proportional to the concentration of oleic acid. Furthermore, the applied heat over extensional reaction during the functionalization of 4-pentynoic acid to the iron oxide may have perfected the inverse spinel structure (Li *et al.*, 2015). Li *et al.* (2015) reported Fe^{2+}-O bands accounted for maghemite, γ-Fe_2O_3 and hematite, α-Fe_2O_3 at 635 cm^{-1} and 475 cm^{-1} respectively. These bands were not observed for any of the spectra, suggesting that all samples exist mostly in magnetite, Fe_3O_4 phase.

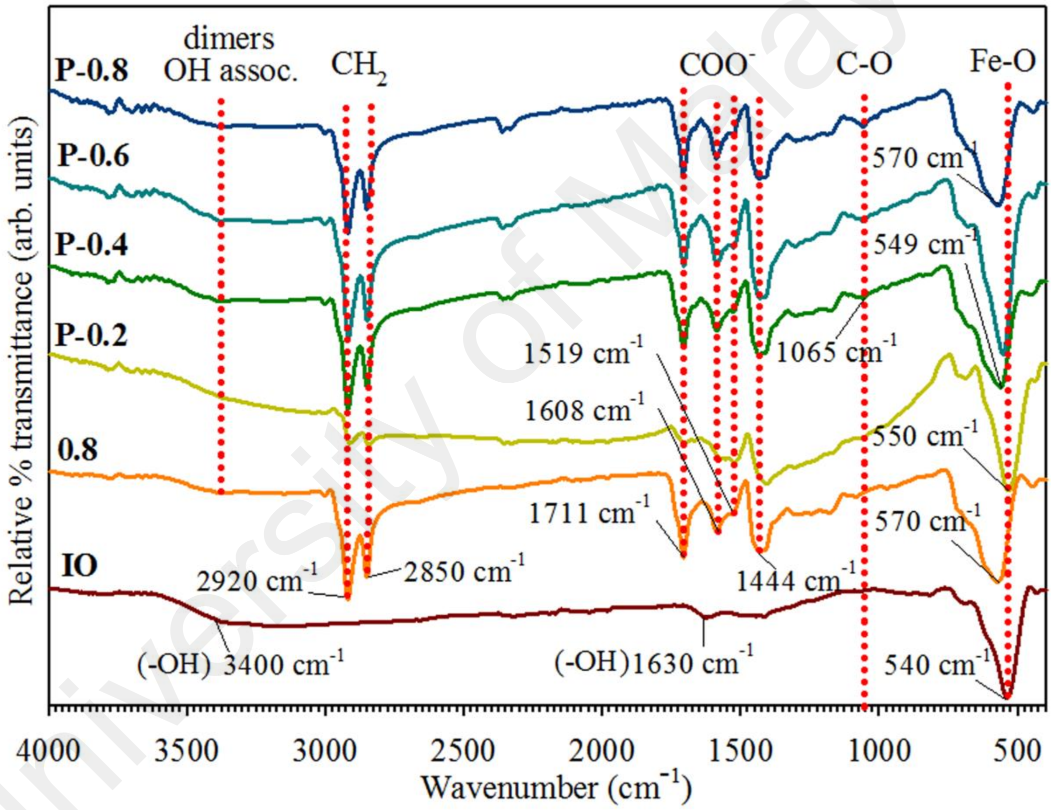

Figure 4.5: FTIR spectra of the samples

Furthermore, coating of oleic acid on the surface of bare Fe_3O_4-γ-Fe_2O_3 NPs was confirmed by FTIR. According to Lu *et al.* (2002), characteristic IR bands for metal carboxylates of asymmetrical and symmetrical vibrations are in the range of 1650-1510 cm^{-1} and 1400-1280 cm^{-1} respectively. Figure 4.6 shows the probable coordination modes that were envisioned for the iron carboxylates of the samples. Iron oxides that were coated with oleic acid alone or functionalized together with 4-pentynoic acid showed bands at υ(COO^-) regions; 1711, 1608, 1519, 1444 cm^{-1}. According to Lu *et al.* (2002), band at 1711 cm^{-1} is designated either to the C=O of oleic acid or the unidentate carboxylate asymmetric vibrations. Though, the probability of the latter occurrence is unlikely.

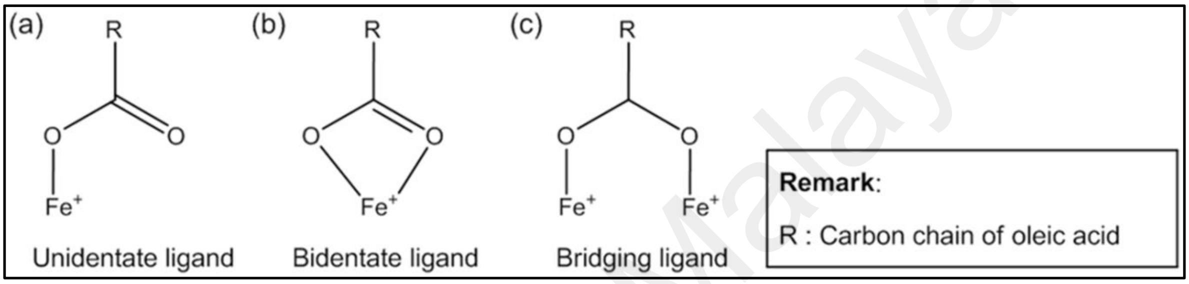

Figure 4.6: Types of Fe^+ carboxylate coordination modes

Additionally, the carboxylate coordination mode can be determined by the wavenumber position difference of the υ(COO^-) bands, Δυ, in 1300-1700 cm^{-1} regions. For unidentate ligand, bidentate ligand and bridging ligand, the Δυ, is > 200 cm^{-1}, < 100 cm^{-1}, and 140-200 cm^{-1} respectively (Bronstein *et al.*, 2007). According to the peaks shown in Figure 4.4, the Δυ between 1519 and 1444 cm^{-1} was deliberated by 75 cm^{-1}, indicating bidentate coordination. Nevertheless, according to Bronstein and co-workers (2007), 1444 cm^{-1} band identity is quite ambiguous because it may be demonstrating an overlapping of the carboxylate stretching with δ(CH_2) scissoring bands. The peaks at 1608 cm^{-1} and 1519 cm^{-1} were presumed to be a doublet resulting from band splitting. Hence, the Δυ between each peak with the 1711 cm^{-1} and 1444 cm^{-1} bands indicate bidentate and bridging coordination modes (Bronstein *et al.*, 2007).

Besides, the stretching vibration of symmetric ($υ_s$) and asymmetric ($υ_{as}$) CH_2 bonds corresponding to carbon chain of oleic acid functionalized to the iron oxides was observed at 2850 cm^{-1} and 2920 cm^{-1} band respectively (Yang *et al.*, 2010; Soares *et al.*, 2014). This further confirms the attachment of oleic acid to the NPs. Contrarily, pure oleic acid CH_2 (υ_s) was credited at 2854 cm^{-1} whereas the CH_2 (υ_{as}) was observed at 2925 cm^{-1}. When these FNPs were compared to pure oleic acid, red shifts of these bands were acknowledged. This is subjected to the way the hydrocarbon chains of oleic acid surrounded the iron oxide FNPs which is assumed to be in a closed-packed crystalline state; an indication of a comprehensive modification of the FNPs with oleic acid (Aliakbari *et al.*, 2015).

Furthermore, the vibration of $\upsilon(COO^-)$ and $\upsilon(CH_2)$ for sample P-0.2 were less intense compared to the other ex-situ oleic acid-coated FNPs. This reaffirms, the existence of a mere monolayer oleic acid surrounding the FNPs of sample P-0.2 compared to the bilayer oleic acid surrounding the other ex-situ coated FNPs as justified by prior thermal decomposition analysis. Stretching vibration of υ(O-H) at 3400 cm^{-1} were also observed for all samples. The bare iron oxide NPs was accompanied by another υ(O-H) at 1608 cm^{-1} which were believed to represent the readily embedded hydroxyl group on the NPs during co-precipitation (aqueous medium) as reported by Yang and coworkers (2010). This finding is also supported by the preceding thermal decomposition analysis. In contrast to the coated iron oxide FNPs, the exhibition of υ(O-H) at approximately 3400 cm^{-1} indicates formation of oleic acid's dimers. Sample P-0.2 demonstrated a rather steeper shoulder at this particular band. In fact, the $\upsilon(COO^-)$ intensities of the carboxylate bonds of sample P-0.2 were weaker than the rest of the oleic acid-coated FNPs. Thus, it could be presumed that at scarce concentration, oleic acid was more inclined to form dimers among its molecule than to be functionalized to the hydroxyl group of the FNPs.

Vibrational band of υ(C-O) at 1065 cm^{-1} was observed for all samples that were functionalized with 4-pentynoic acid. This band represents acid anhydride stretching between the functionalized secondary layer oleic acid and the 4-pentynoic acid (Pavia *et al.*, 1996). 1800 and 1740 cm^{-1} vibration bands of the asymmetric and symmetric stretch of anhydride C=O bonds cannot be confirmed due to overlapping with the Fe+ carboxylate bands. Sample P-0.2 did not experience any vibration at such region since there were no binding sites available for the 4-pentynoic acid to be functionalized on the monolayer oleic acid-coated iron oxide NPs. This consequently authenticates the proposed chemical structures of the samples in Table 4.2. Peak assignments to the reported IR bands are also associated.

Sample P-0.4 was also analyzed for proton (1H) NMR (Appendix A). Despite being washed with solvents, the sample was not thoroughly purified. For this reason, it was dissolved in a very small amount in $CDCl_3$ to avoid turbidity. The 1H-NMR spectrum is reported as 1H NMR (300MHz, $CDCl_3$) δ 2.19 (1H, s), 1.61 (3H, t). The singlet and triplet chemical shifts correspond to terminal alkyne of 4-pentynoic acid and methyl group of the primary layer oleic acid respectively (Skoog *et al.*, 2007). Because of poor sensitivity, only these two chemical shifts were able to be recorded which represent the periphery functional groups protruding outward from the spherical nature of the sample. Despite the undetected chemical shift of anhydride, the chemical shift at 2.19 ppm representing terminal alkyne of 4-pentynoic acid designates the successful functionalization of 4-pentynoic acid.

Table 4.2: Proposed chemical structures of the samples; plausible functional groups ssociated

Sample	Chemical structure	Peak assignment	IR-band (cm^{-1})
IO	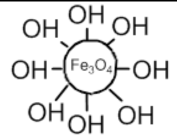	υ(Fe-O) υ(O-H) δ(O-H)	540 1630 3400
0.8	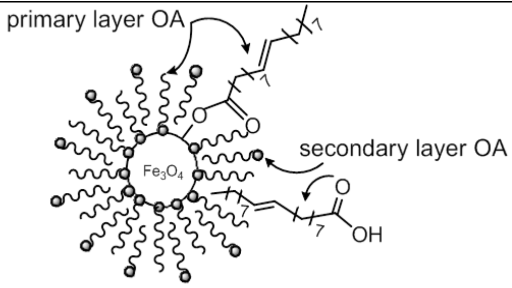	υ(Fe-O) υ(COO) υ(COO) υ(COO) υ(COO) υ_s(CH$_2$) υ_{as}(CH$_2$)	570 1444 1519 1608 1711 2850 2920
P-0.2	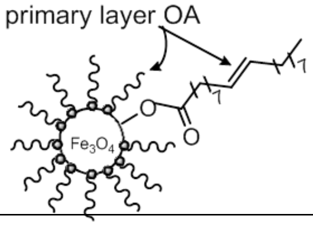	υ(Fe-O) υ(COO) υ(COO) υ(COO) υ(COO) υ_s(CH$_2$) υ_{as}(CH$_2$)	550 1444 1519 1608 1711 2850 2920
P-0.4 P-0.6 P-0.8	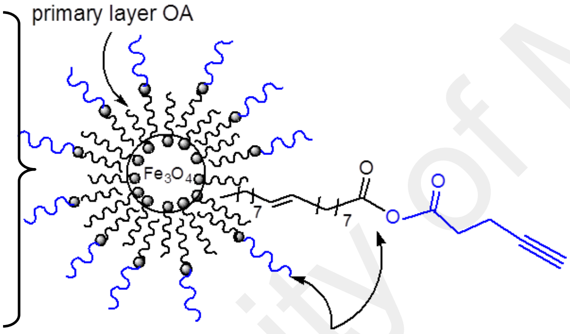 functionalization of 4-pentynoic acid to secondary layer oleic acid-modified iron oxide NPs	υ(Fe-O) υ(C-O)acid anhydride υ(COO) υ(COO) υ(COO) υ(COO)unidentate υ_s(CH$_2$) υ_{as}(CH$_2$)	549-570 1065 1444 1519 1608 1711 2850 2920
-	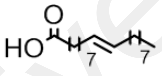 oleic acid 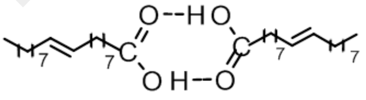 dimer of oleic acid	δ(O-H)out-of-plane υ(C-O) δ(O-H)in-plane υ(C=O) υ(C-H) υ(C-H) υ(O-H) dimer	937 1285 1463 1715 2854 2925 2800-3300
-	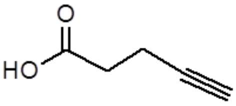 4-pentynoic acid	δ(C≡C-H) υ(C-O) υ(C=O) υ(C≡C) υ(C-H) υ(C-H) υ(C≡C-H)	636 1212 1740 2100 2850 3025 3290

4.1.1.4 Hydrodynamic particle size distribution and stability

Figure 4.7 shows PSD of the samples. Boxplot interpretations were generated to better express the distributions of the particle sizes. All samples were diluted to 0.1 g/L in deionized water and altered back to their originally acidic environment (pH 12). These samples were characterized for particle size distribution (PSD) and zeta potential (ZP). Commonly, the PSD is expressed by implying the diffusion speed of NPs or FNPs caused by Brownian motion which is in turn, measured by dynamic light scattering (DLS) (Finsy, 1994). Unlike number distribution, volume and intensity distributions are biased toward bigger size particles since they consider volume of the particles and light scattering which is greater emitted by larger size particles respectively.

Therefore, in this study, number distribution of hydrodynamic particle was chosen to yield peaks that were influenced by number of particles present in the polar basic medium (*Zetasizer Nano User Manual*, 2007, p. 13.6). On the other hand, stability of NPs dispersed in any aqueous medium can be defined by zeta potential which interprets the potential difference between the slipping plane in the electronic double layer and the bulk potential.

The PSD of all the samples were observed within approximately similar range of 24-156 nm. They were skewed to larger particle sizes but only with small number %. Nonetheless, the interquartile range was taken into account since it is the most significant robust measure of scale (Graham & Ian, 1996). The interquartile ranges of the samples were accentuated toward smaller range particle size with median being within 48-68 nm. Conspicuously, sample P-0.4 displayed the best PSD followed by sample 0.8, both with their closely distributed particle sizes.

Table 4.3 reveals the trends of mean hydrodynamic particle size distribution and zeta potential (ZP) of the iron oxide NPs and FNPs. It is well established that stability dividing line for hydrodynamic particles is accredited at ±30 mV. Zeta potential exceeding this value signifies even more stable medium (Hunter, 1988). Generally, the infused magnetic fields between the iron oxide NPs trigger more flocculation hence, instigate quicker agglomeration. Moreover, without proper surface coating, the NPs would aggregate and form large cluster resulting in increased particle size (Wu *et al.*, 2008).

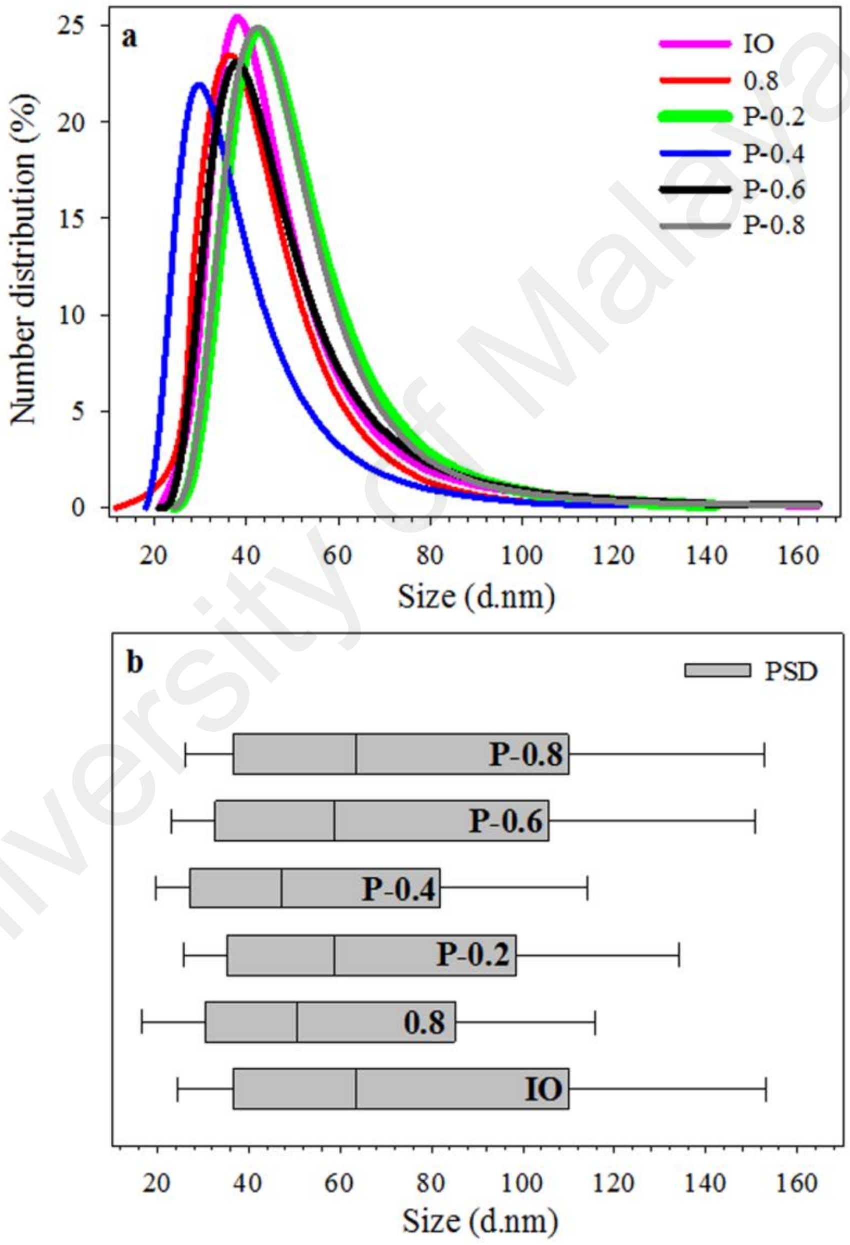

Figure 4.7: Distributions of (a) Number % particle size (PSD) (b) Number % particle size (PSD) using box plot interpretation

Table 4.3: Mean PSD and ZP of the samples

Sample	**OA/IO (g/g)**	**4-pentynoic acid (1.63 mmol)**	**Mean PSD (nm ± $\sigma_{\bar{X}}$)**	**Mean ZP (mV ± $\sigma_{\bar{X}}$)**
IO	0.0	x	44.73 ± 0.85	-42.08 ± 0.18
0.8	0.8	x	41.19 ± 1.53	-62.01 ± 0.03
P-0.2	0.2	√	48.08 ± 0.29	-47.70 ± 0.03
P-0.4	0.4	√	35.68 ± 0.03	-75.61 ± 0.56
P-0.6	0.6	√	44.79 ± 0.04	-54.01 ± 0.14
P-0.8	0.8	√	47.55 ± 0.12	-68.10 ± 0.88

Remarks: x – Not applied √ - Applied

When the samples were altered to pH 12, the NPs and FNPs tend to acquire more positive charges (cation NH_4^+) from dissociations of ammonia solution. Hence, the built up ionic salts encouraged the NPs and FNPs to repel one another preventing flocculation and promoted more dispersity in the polar basic medium. This permits a thorough ex-situ modification of the bare iron oxide NPs with the surfactants.

The bare iron oxide, sample IO demonstrated the least favorable ZP at -42.08 mV which explains the marginally wider distribution of its size particles. This also set off quite large mean PSD at 44.73 nm. Although sample IO is reasonably stable, it is the least stable NPs presented in the polar, basic medium compared to other surface modified iron oxide FNPs. Because of inadequate concentration of oleic acid, sample P-0.2 exhibited similar fate of ZP (-47.70 mV) as the non-polar hydrophobic tail of oleic acid extended out in the polar basic medium. This complements its exhibition as the largest mean PSD (48.08 nm) among the iron oxide NPs and FNPs.

It is apparent that both sample IO and P-0.2 were more prone to earlier agglomeration than the rest. Contrariwise, samples that were sufficiently coated with oleic acid showed more encouraging ZP at estimated -54 mV to -75 mV. This manifestation deduces that aside from the role of pH, the stearic hindrance contributed by the functionalized surfactants helps in reducing potential flocculation.

Comparison between sample 0.8 and P-0.8 suggests that functionalization of 4-pentynoic acid to iron oxide reasonably increased mean PSD at 41.12 nm to 47.55 nm respectively, despite the improvement of ZP from -62.01 mV to -68.10 mV after functionalization of 4-pentynoic acid for sample P-0.8. Nonetheless, zeta potentials of the FNPs are reckoned as reassuring due to the functionalized surfactants in an elevated pH 12 medium.

The mean hydrodynamic particle sizes of the NPs and FNPs are bigger than the mean crystallite sizes because inorganic core and the organic coating (functionalized materials) along with the solvent layer attached to the NPs and FNPs were taken into accounts in the PSD analysis as it moves under the influence of Brownian motion. In contrast, mean crystallite size deliberated only inorganic core of the NPs and FNPs (Hackley & Clogston, 2011). The mean hydrodynamic particle size distribution is meant to merely complement the zeta potential hence, correlation with the mean crystallite size is non beneficial.

4.1.1.5 Mechanisms

The 1.5 molar ratios of ferric ion and ferrous ion yield 10 ± 2 nm mean crystallite size and stable NPs in a polar basic medium at pH 12. Ex-situ oleic acid modifications of iron oxide FNPs were conducted first, followed by functionalization of 4-pentynoic acid to the FNPs. The NPs and FNPs were altered to pH 12 for both reactions. This created salts which promoted more repulsion between the NPs and FNPs hence enhanced dispersity. A good dispersion of NPs in an aqueous medium allowed a thorough coating of oleic acid to the surface of iron oxide NPs as well as the functionalization of the 4-pentynoic acid. The oleic acid formed esterification with hydroxyl group that were readily embedded on the surface of the bare Fe_3O_4-γ-Fe_2O_3 NPs.

Two plausible types of oleic acid coatings were produced for the ex-situ modifications of different oleic acid concentrations as shown in Appendix B (i) and (ii). Monolayer oleic acid-coated iron oxide FNPs was supposedly produced for FNPs that were ex-situ coated with 0.2 g/g oleic acid to iron oxide. Whereas the greater concentration ratios of 0.4, 0.6 and 0.8 g/g produced bilayer oleic-acid coated iron oxide FNPs. Interpenetration layer was formed between hydrophobic tails of the primary layer and secondary layer oleic acid in this reaction as illustrated in Figure 4.3.

Functionalization of 4-pentynoic acid was performed for all of the ex-situ oleic acid-coated iron oxide FNPs (monolayer and bilayer). With the assistance of heat treatment at 60˚C the 4-pentynoic acid was functionalized to the secondary layer oleic acid forming acid anhydride. The ionic bonds $-COO^{-}\ NH_4^{+}$ that were initially formed, were broken down when higher temperature was applied, causing the COO^{-} to become a nucleophile that subsequently attacked -COOH of 4-pentynoic acid as illustrated in Appendix C and D. Essentially, the existence of bilayer oleic acid coating on the iron oxide at 60 ˚C in pH 12 basic medium enables a successful functionalization of 4-pentynoic acid via nucleophilic substitution as seen in Appendix C.

Therefore, only FNPs that yielded bilayer oleic acid were believed to have been successfully functionalized with 4-pentynoic acid. The ex-situ monolayer oleic acid-coated iron oxide FNPs produced by 0.2 g/g oleic acid to iron oxide was not successfully functionalized with 4-pentynoic acid. There were no binding sites available on the monolayer oleic acid for the attachment of 4-pentynoic acid as only hydrophobic tail

($-CH_3$) of the oleic acid protruded outwards. Besides, the chemical structures envisioned create an understanding that greater concentration of oleic acid, prior ex-situ modification along with functionalization of 4-pentynoic acid would generate bigger micelle.

4.1.2 Self-assembly of FNPs on SiO_2/n-Si structure

The second part discusses on microstructural study, phase determination, chemical interactions at the FNPs/SiO_2/Si interfaces, magnetic properties, surface morphology, and electrical properties of the self-assembled films. Sample P-0.4 from the first part was chosen for self-assembly because it retains the greatest hydrodynamic stability and was successfully functionalized with 4-pentynoic acid.

4.1.2.1 Microstructural study

XRD patterns of the as prepared films are shown in Figure 4.8. Diffraction peaks of the FNPs spinel structure were indexed to hkl (220), (311), (400), (511), (440), (533), and (622). Comparisons with magnetite (JCPDS card #19-0629) and maghemite (JCPDS card #39-1346) indicate that the structure is intermediate. Traces of SiO_2 corresponding to cristobalite phase (JCPDS card #39-1425) indexed to (3 0 2), (2 2 3) and (2 1 4) as well as quartz (JCPDS card #46-1045) of hkl (3 0 2) were found in the diffraction peaks. The SiO_2 was developed on the substrate, indicating surface oxidation of the Si surface.

Based on the corresponding peaks intensities, oxidation rate of the substrate increased proportionally with heating temperature. The peaks were profile fitted with pseudo-Voigt profile shape function using HighScore Plus (version 3.0d). The integral breadths were corrected for instrumental broadening using standard Si. Mean crystallite sizes of 8 ± 1 nm were acquired by Debye-Scherrer method for roughly all samples. 70-300 ˚C heat treatments did not provide significant differences to crystallite sizes of the FNPs. Moreover, crystallite sizes of the FNPs are relatively the same before (9.7 ± 0.7) and after (8 ± 1 nm) the self-assembly.

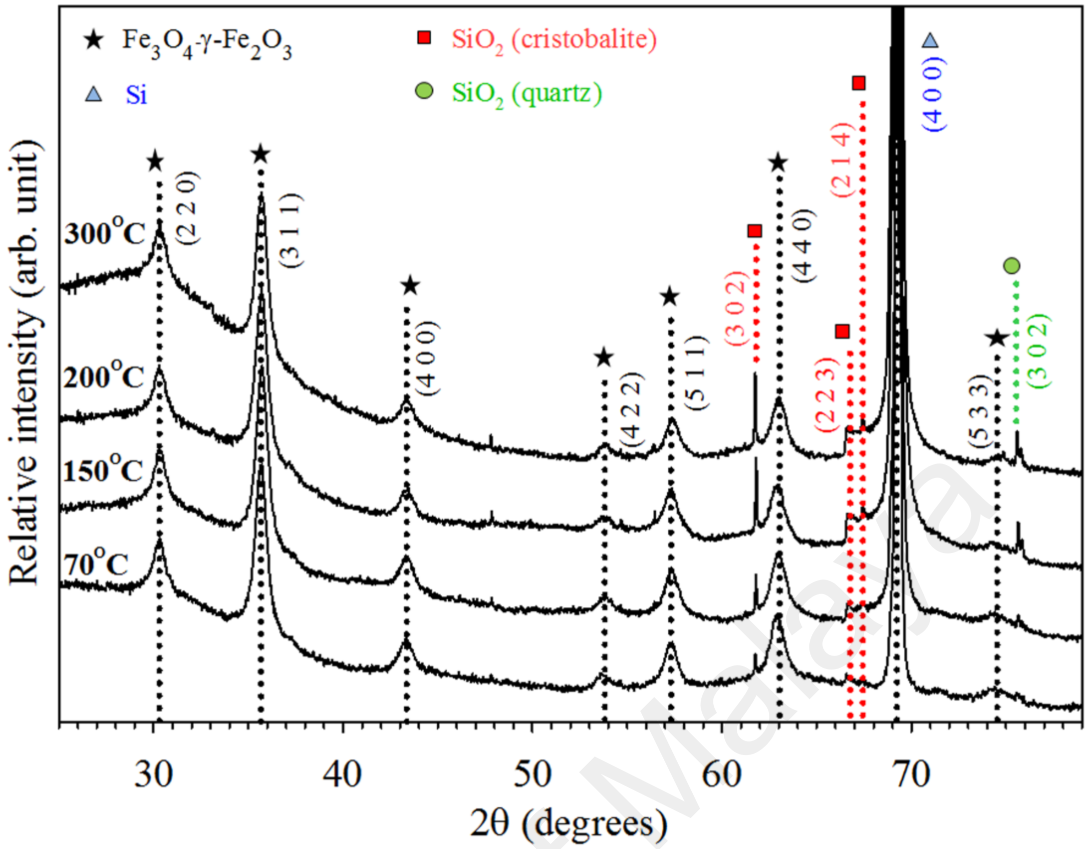

Figure 4.8: XRD diffraction patterns of the as prepared films

4.1.2.2 Phase determination

Phase determination of the samples was confirmed by Raman spectra analysis (Figure 4.9). The main magnetite (Fe_3O_4) band which was agreed upon by literature varied between 661-676 cm^{-1} (Li *et al.*, 2012; Li *et al.*, 2010; Hanesch, 2009). Different laser wavelengths and powers used by different researches in their studies might have caused such variation. Besides, bands at 730, 512, 486 and 350 cm^{-1} were reportedly assigned to maghemite (γ-Fe_2O_3) (Roth *et al.*, 2015; Li *et al.*, 2012; Guo *et al.*, 2011; Li *et al.*, 2010; Raman *et al.*, 1998). Bands observed at 380 cm^{-1} and 480 cm^{-1} in this study closely conform to γ-Fe_2O_3. These bands became more prominent with increasing heating temperature of the samples.

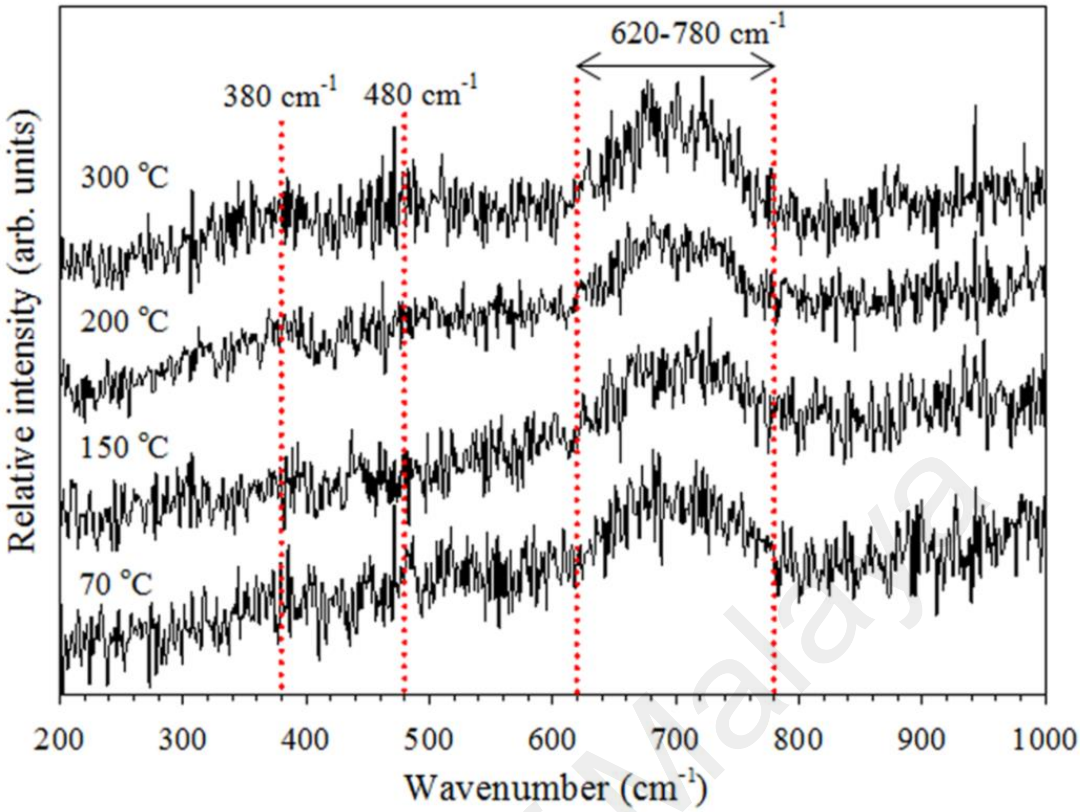

Figure 4.9: Raman spectra of the as prepared films

In addition to that, previous studies identified a characteristic broad band amid 673 cm^{-1} and 722 cm^{-1} as mixture of Fe_3O_4 and γ-Fe_2O_3 (Hanesch, 2009). The appearance of a broad band at 620-780 cm^{-1} in this study indicates the coexistence of Fe_3O_4 and γ-Fe_2O_3 for all samples which conforms to the XRD analysis. Besides that, bands at 225 cm^{-1} and 290-300 cm^{-1} used for identification of hematite (α-Fe_2O_3) (Hanesch, 2009) were not visible in the spectra verifying that the as prepared Fe_3O_4-γ-Fe_2O_3 films did not transform into α-Fe_2O_3.

4.1.2.3 Chemical interactions at the FNPs/SiO_2/Si interfaces

ATR-IR spectra of the samples are shown in Figure 4.10. CH_2 asymmetric and symmetric stretching vibrations were found at 2918 cm^{-1} and 2850 cm^{-1} respectively (Pujari *et al.*, 2012).

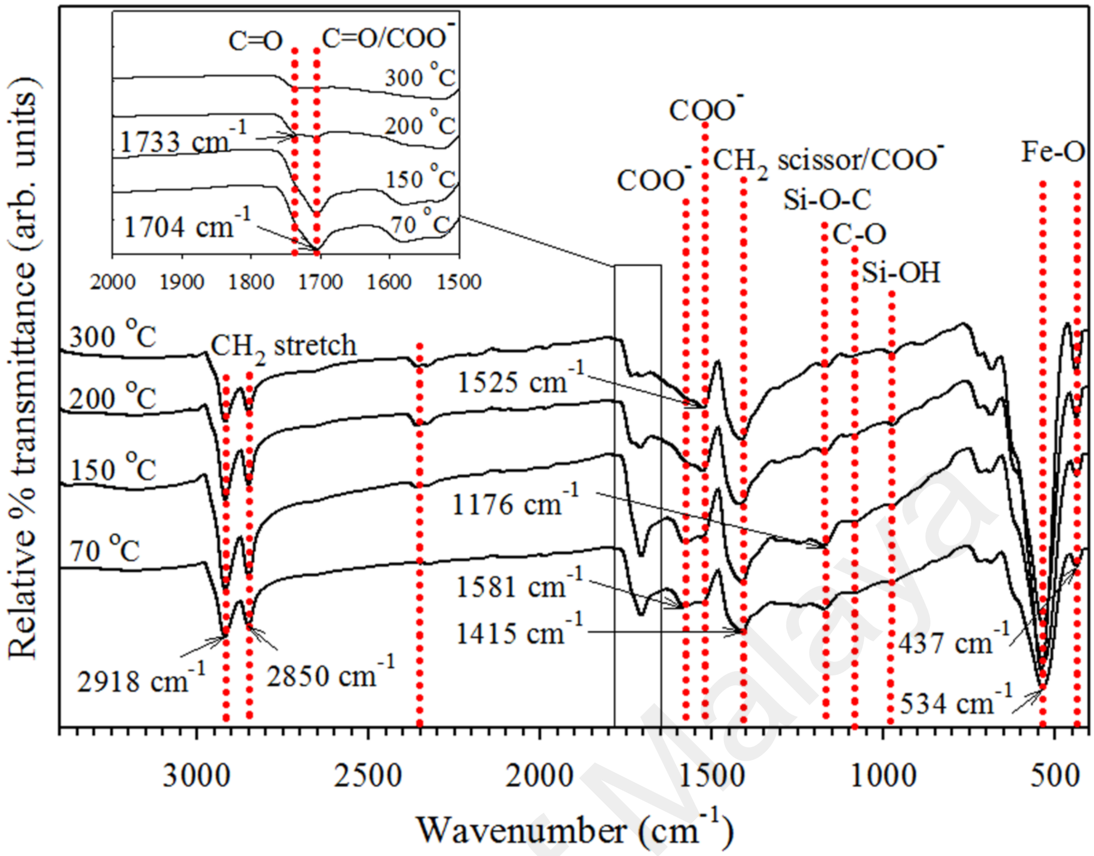

Figure 4.10: ATR-IR spectra of the as prepared films. The inset displays closer looks of vibrational frequencies of acid anhydride υ(C=O) and iron carboxylate υ(COO$^-$)

In comparisons, bands at 1704, 1581, 1525, and 1415 cm^{-1} were assigned to υ(COO$^-$) stretch of iron carboxylates (Do *et al.*, 2013; Yang *et al.*, 2010; Brostein *et al.*, 2007; Lu & Miller, 2002). However, these vibrational frequencies might be brought up by overlapping of different functional groups. For instance, the inset shows a shoulder band at 1733 cm^{-1} corresponding to asymmetric $υ_{as}$(C=O) stretch of acid anhydride (refer Figure 4.11) whereas vibrational band at 1704 cm^{-1} is assigned to an overlapping of acid anhydride symmetric C=O stretch (Pavia *et al.*, 1996) and COO$^-$ stretch (Lu *et al.*, 2002; Bronstein *et al.*, 2007). The same goes to vibrational band at 1415 cm^{-1} which could be resulted from overlapping of COO$^-$ stretch and CH$_2$ scissor mode (Bronstein *et al.*, 2007).

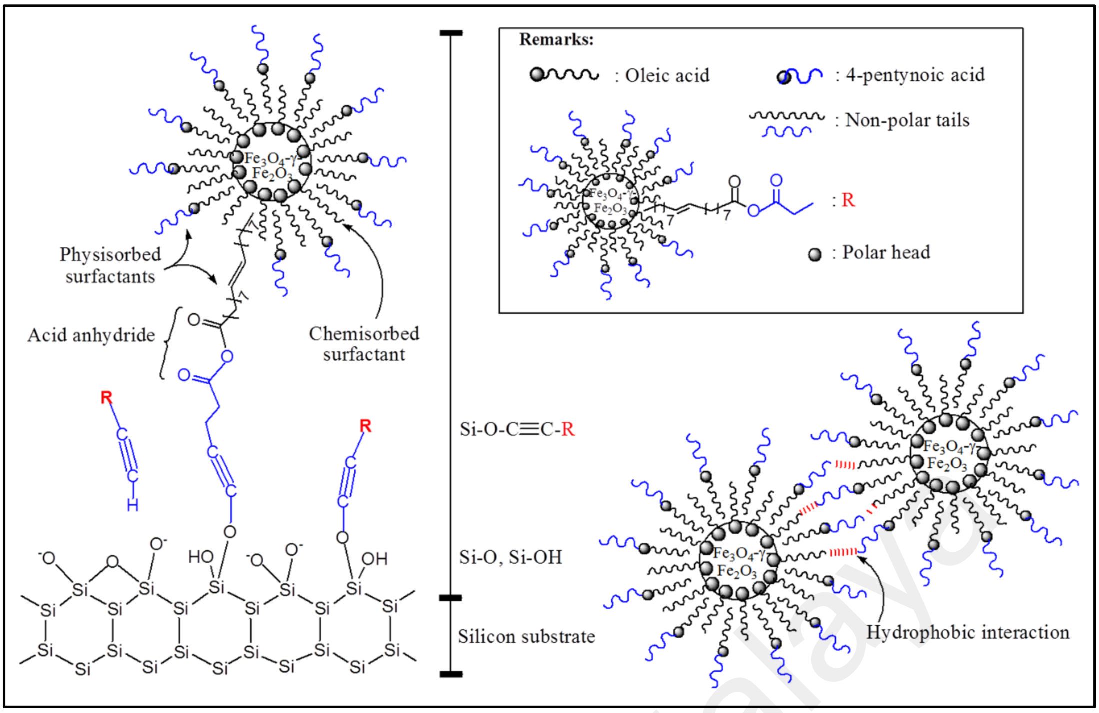

Figure 4.11: Self-assembly of the FNPs

Besides, vibrational Si-O, Si-O-C (Ruhai *et al.*, 2010), and Si-OH (Guo & Ying, 2002) stretch appeared at 1241 cm^{-1}, 1176 cm^{-1}, and 976 cm^{-1} respectively. These identified bands enabled self-assembly illustration of the FNPs as shown in Figure 4.11 (a). Apart from covalent interactions at the interface, the Fe_3O_4-γ-Fe_2O_3 FNPs were expected to exhibit hydrophobic interactions between one another (Figure 4.11 (b)). Peak assignment to 1085 cm^{-1} is contributed by υ(C-O) stretch (Ruhai *et al.*, 2010) of the acid anhydride. Whereas vibrational bands at 437 cm^{-1} and 534 cm^{-1} were appointed to Fe-O stretch which is in agreement with Waldron (1955).

Weaker vibrational intensities of bands around 1800-1000 cm^{-1} for samples heated at 300 ˚C and 200 ˚C give an impression that the physisorbed surfactants were disintegrated from the FNPs. Intensities of υ_{as} and υ_s(C=O) stretch as well as υ(C-O) stretch of the acid anhydride are particularly highlighted. Subsequently, υ(Si-O-C) stretch became weaker. This signifies more disintegrated bonding of the Si-O-C as heating temperature elevated. Likewise, a frailer stretching of Si-O bond and a stronger υ(Si-OH) stretch for the respective samples suggest that more of the latter bonding was developed as results to the physisorbed surfactants disintegration.

4.1.2.4 Magnetic properties

The magnetization curves of the samples are shown in Figure 4.12. A portion of the curve in close vicinity (inset of Figure 4.12) displays subtle ferromagnetic properties with narrow hysteresis loops for the three samples.

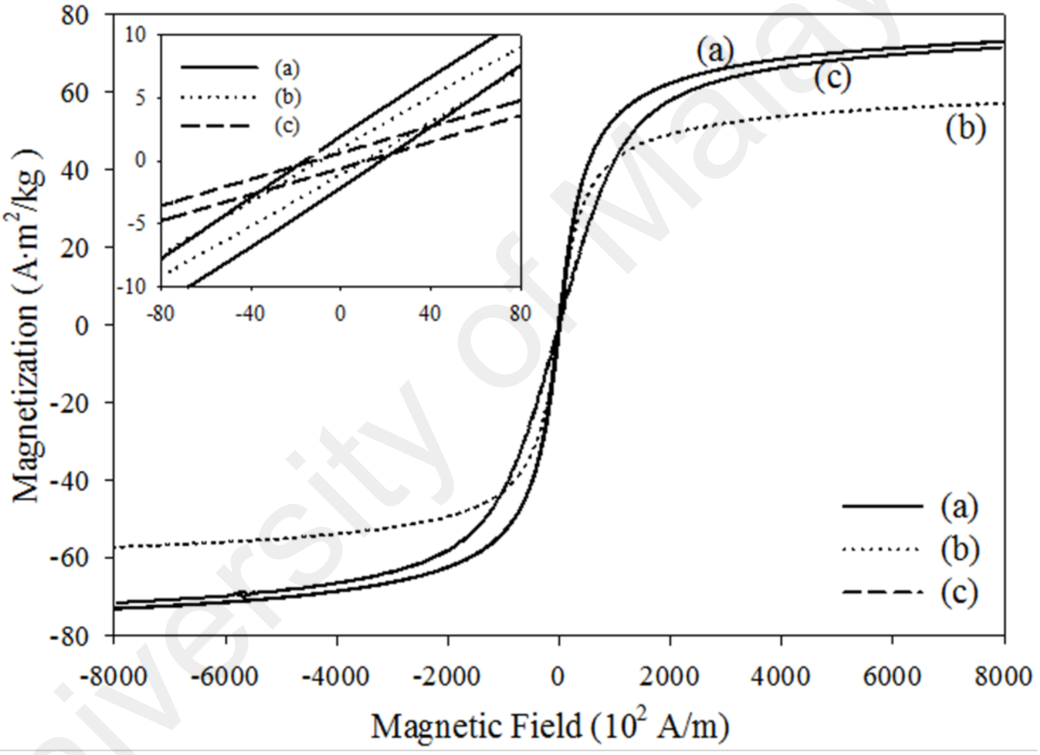

Figure 4.12: Magnetization curve at 298 K of (a) bare Fe_3O_4-γ-Fe_2O_3 (b) functionalized Fe_3O_4-γ-Fe_2O_3 (c) FNPs deposited on Si substrate heated at 300 ˚C.

Magnetic properties of bare Fe_3O_4-γ-Fe_2O_3 NPs, functionalized Fe_3O_4-γ-Fe_2O_3 FNPs, and deposited functionalized Fe_3O_4-γ-Fe_2O_3 FNPs on Si substrate (as prepared film) were investigated at 298 K in an applied magnetic field from -8 to 8 kG. The Si substrate, to which the as prepared film was assembled, was cut into surface area of 0.7 cm x 0.7 cm using diamond cutter. This is to ensure that the as prepared sample would fit the sample holder of vibrating sample magnetometer (VSM). In order to investigate the difference between magnetic properties of the deposited Fe_3O_4-γ-Fe_2O_3 FNPs film with the bulk FNPs, the as prepared sample was characterized altogether with its substrate. A known mass of the deposited film was retrieved to establish such investigation.

Saturation magnetization, (M_s) of sample (a), (b), and (c) were attained at 74.157, 58.002, and 71.527 A·m^2/kg respectively. M_s of the functionalized Fe_3O_4-γ-Fe_2O_3 FNPs (b) appeared lower than the bare Fe_3O_4-γ-Fe_2O_3 NPs (a). This implies that the presence of functionalized surfactants reduced magnetic moments at the surface of the FNPs which was also observed in a study conducted by Soares *et al.* (2014). Nevertheless, $M_s$of the deposited Fe_3O_4-γ-Fe_2O_3 FNPs film on Si substrate (c) increased suggestively, close to that of the bare NPs' (a). This could be associated to the increased crystallinity of the FNPs when heat treatment at 300 ˚C was introduced to the Fe_3O_4-γ-Fe_2O_3 film. Besides, the increment of $M_s$could be an indication of physisorbed surfactants disintegration from the FNPs as acknowledged previously in IR analysis. Nonetheless, sample (c) attained slightly lower value of M_s than the bare NPs (a) due to diamagnetic contribution of Si.

Coercivity (H_{ci}) of sample (a), (b), and (c) were acquired at 1415.444, 861.267, and 929.942 A/m respectively. H_{ci} values of the investigated samples showed similar trend as the M_s. This can also be attributed to the increasing crystallinity (Zhu *et al.*, 2007) of the FNPs as a consequence of heat treatment given to the deposited Fe_3O_4-γ-Fe_2O_3 film. In a nutshell, saturation magnetization and coercivity of the samples can be increased by increasing crystallinity of the Fe_3O_4-γ-Fe_2O_3 NPs by means of heat treatment.

4.1.2.5 Surface morphology

Two-dimensional (2D) surface topographies of the as prepared films are displayed in Figure 4.13. Overall, surface topographies of the samples were broken with prominences. Larger lumps of FNPs, resulted from greater aggregation were developed at the surface of films heated at 150 ˚C and 70 ˚C. In contrast, samples that were heated at higher temperatures showed more disseminated distribution of FNPs, resulting from the disintegration of the physisorbed surfactants.

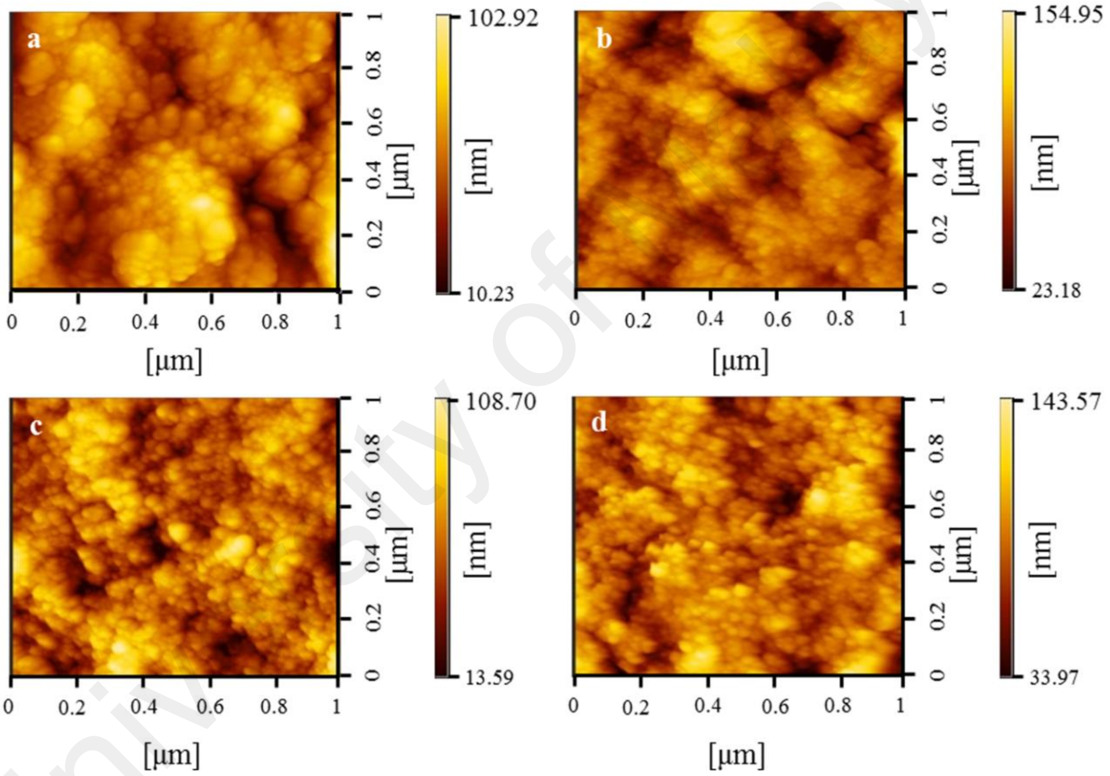

Figure 4.13: Two-dimensional (2D) surface topographies of the as prepared films heated at (a) 70 ˚C, (b) 150 ˚C, (c) 200 ˚C, and (d) 300 ˚C

As illustrated in Figure 4.11, the hydrophobic interactions between physisorbed surfactants encouraged more aggregation of the FNPs compared to the samples without such interactions. While Figure 4.14 demonstrates the corresponding root mean square (RMS) roughness of the as prepared films. Heating of samples at different temperatures

(70-300 ˚C) gives significant distinctions to the RMS roughness of the deposited Fe_3O_4-γ-Fe_2O_3 films. While the highest RMS roughness was demonstrated by the sample heated at 150 ˚C (18.12 ± 7.13 nm), the lowest RMS roughness was exhibited by the sample heated at 200 ˚C (12.99 ± 4.39 nm) with more or less the same value as the one that was heated at 300 ˚C (13.58 ± 4.03 nm).

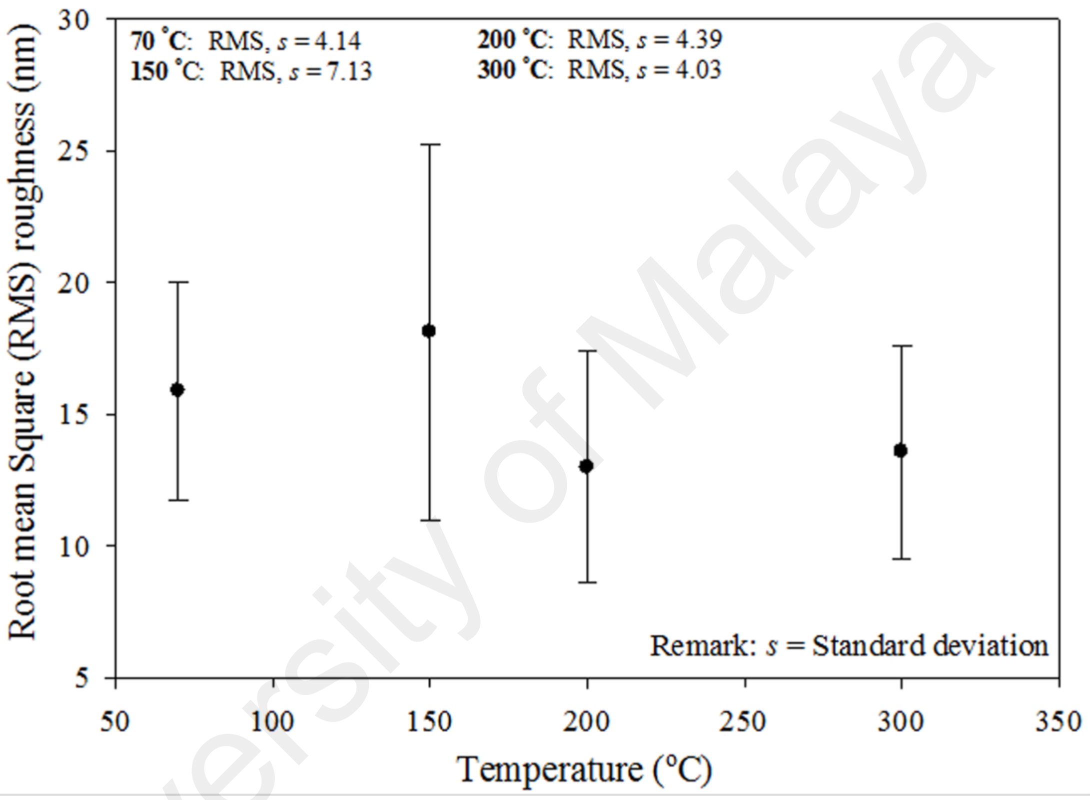

Figure 4.14: Root mean square (RMS) roughness of the as prepared films

Samples which experienced physisorbed surfactants disintegration (samples heated at 300 ˚C and 200 ˚C) showed lower RMS roughness than the ones with physisorbed surfactants remained intact (samples heated at 150 ˚C and 70 ˚C). Evidently, RMS roughness of the samples was influenced by the presence of the physisorbed surfactants. Concisely, the deposited FNPs experienced less aggregation in the absence of the physisorbed surfactants most likely stimulated by the hydrophobic interactions.

FE-SEM investigation indicated distribution of non-uniformly aggregated NPs across the Si substrate for all the as prepared films. This was represented by the sample heated at 150 ˚C as shown in Figure 4.15 (a). The FNPs were unevenly distributed with formations of vales (dotted lines in Figure 4.15 (a)), signifying non-uniformed accumulations of FNPs. Figure 4.15 (b) displays cross-section of the as prepared film to which the surface of the deposited NPs appeared coarse and grainy (dotted lines in Figure 4.15 (b)). With reference to the cross-section image, it is indisputable that the overall RMS roughness values of the samples were remarkably large. Thickness of the deposited film for all samples is acquired at 12.6 μm (represented by the sample heated at 150 ˚C) as exhibited by the cross-section analysis of FE-SEM in Figure 4.15 (b). 70-300 ˚C heat treatments did not give any dissimilarity to the thickness of the deposited film.

4.1.2.6 Electrical properties

J-E plot (Figure 4.16) was transformed from current-voltage (I-V) measurements, acquired from computer-controlled SPA system. The acquired thickness from Figure 4.15 was used in the retrieval of leakage current density-electric field (J-E) characteristic of the samples. Approximation of the E value was estimated by the following equation, where V_g is the gate voltage, V_{FB} is the flatband voltage and t_{ox} is the total thickness of the Fe_3O_4-γ-Fe_2O_3 FNPs film (Schroder, 2006):

$$E = V_g - V_{FB}/t_{ox} \qquad 4.4$$

All of the samples demonstrate one-step oxide breakdown field (E_B). Sample heated at 150 ˚C reveals the highest E_B followed by the samples heated at 70 ˚C, 200 ˚C, and 300 ˚C (the lowest E_B) with distinguished values of 2.58 x 10^{-3}, 1.83 x 10^{-3}, 1.42 x 10^{-3}, and 1.08 x 10^{-3} MV/cm respectively. This variation can be related to surface roughness

(RMS) of the samples. With the highest RMS value at 18.12 ± 7.13 nm, the sample heated at 150 ˚C showed the most encouraging E_B. Whereas the sample heated at 300 ˚C with lower RMS value of 13.58 ± 4.03 nm demonstrated the lowest E_B.

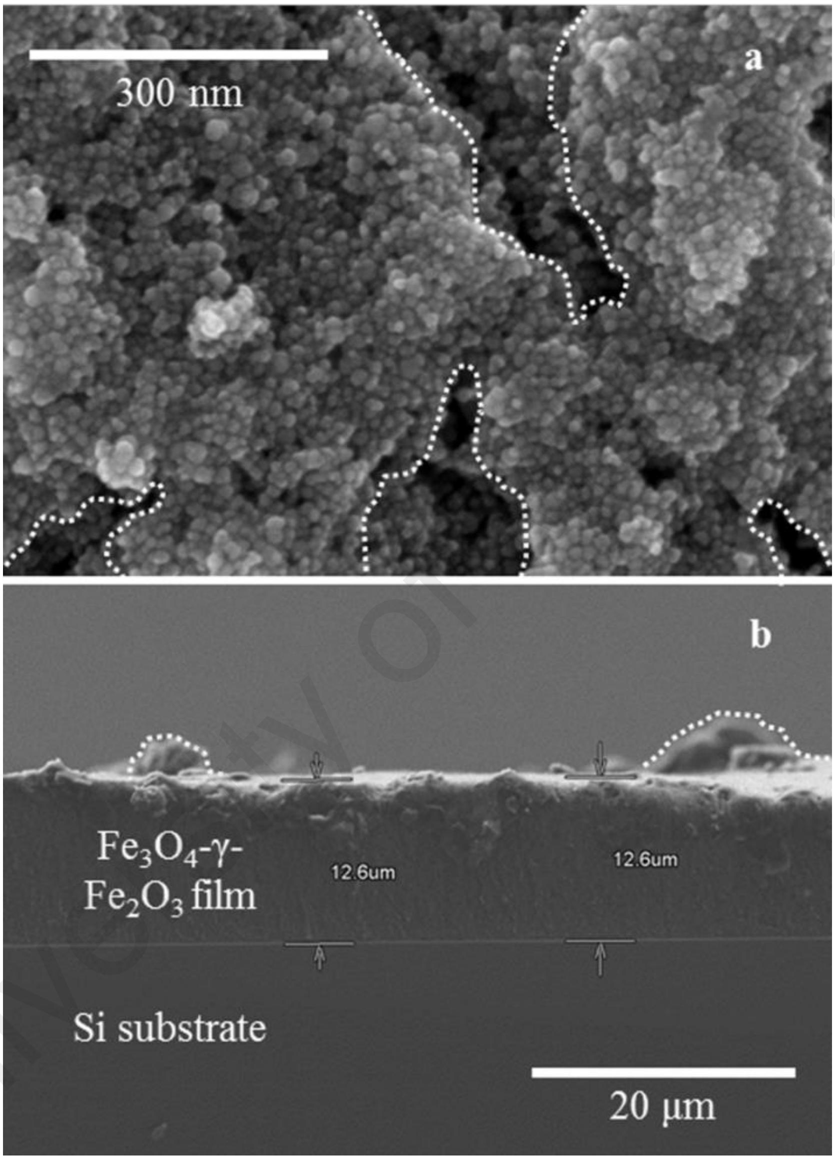

Figure 4.15: FE-SEM image of (a) the as prepared film (heated at 150 ˚C) (b) cross section of the as prepared film (heated at 150 ˚C) with 12.6 µm thickness of FNPs

Comparatively, surface roughness of the as prepared films corresponds to aggregations of Fe_3O_4-γ-Fe_2O_3 FNPs especially at the surface of the film. Hence, FNPs that were molded into greater aggregations with respect to higher RMS roughness, showed higher oxide breakdown field (sample heated at 150 ˚C). The closer each FNP to another aids in the enhancement of electrical breakdown field of the samples. Opposing to this, heating of sample at 300 ˚C had resulted in declination of surface roughness as a subsequent effect to detachment of aggregated FNPs, resulted from physisorbed surfactants disintegration. These may lead to deterioration of oxide breakdown field of the sample.

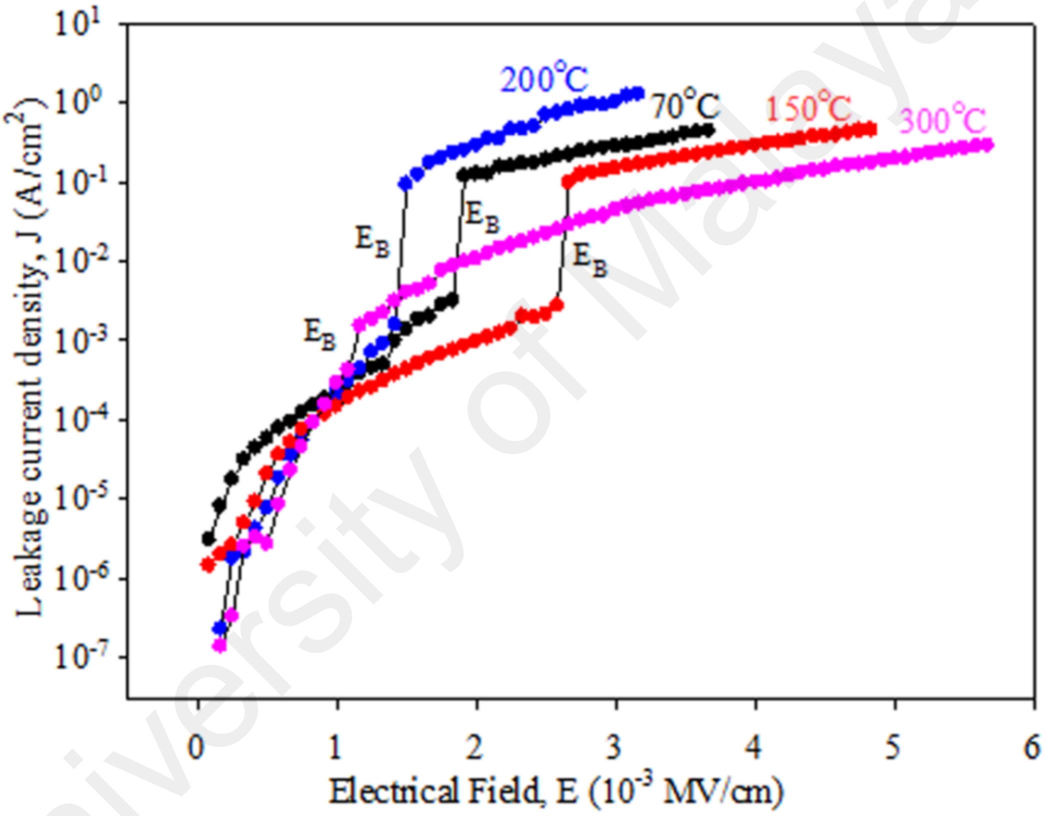

Figure 4.16: J-E characteristics of the as prepared films

Aside from lesser aggregation of FNPs leading to lower RMS roughness, physisorbed surfactants disintegration stimulated another cumulative effect; the breaking down of Si-O-C linkage as suggested in the IR analysis. Succeeding as the most astounding physisorbed surfactants disintegration, sample heated at 300 ˚C developed the least formation of Si-O-C bonds between the substrate and the physisorbed 4-pentynoic acid. Furthermore, as seen in the IR spectra, heating of samples at 300 ˚C and 200 ˚C had induced more formation of Si-OH defects. This triggered interface trapping hence, more depreciation of electrical breakdown field.

Evidently, the establishment of linkages between the functionalized Fe_3O_4-γ-Fe_2O_3 FNPs and the substrate through Si-O-C bonding assists in the improvement of oxide breakdown field (samples heated at 150 ˚C and 70 ˚C). Hence, it can be deduced that self-assembly of the functionalized Fe_3O_4-γ-Fe_2O_3 FNPs had induced chemical interactions (linkages) at the interface, counterbalancing the surface dipole that normally present within a non-coated interface. This consequently, permits a better energy alignment as suggested by Miozzo *et al.* (2010).

Barrier height (ϕ_B) of conduction band edge between Si and Fe_3O_4-γ-Fe_2O_3 FNPs was extracted from Fowler-Nordheim (FN) tunneling model shown in Equation 4.5. FN tunneling corresponds to the flow of electron through a triangular potential barrier into conduction band of an insulator (Schroder, 2006).

$$\ln(J_{FN}/E^2) = \ln(A) - B/E \qquad 4.5$$

Figure 4.17 displays a linear FN plot of $\ln(J_{FN}/E^2)$ against $1/E$. While A was yielded from intercept of the plot, B was extracted from gradient of the slope. Electron effective mass of high κ oxide was assumed to be $0.3m$ in the calculation of ϕ_B (Goh *et al.*, 2016). The calculated ϕ_B is presented in the inset of Figure 4.17. The obtained values of ϕ_B ranged from 0.19-0.38 eV. Sample heated at 150 ˚C attained the highest barrier height among the as prepared films (0.38 eV). In comparison to the calculated barrier height of Fe_3O_4/n-Si reported by Deniz *et al.* (2016) at 0.83 eV, the barrier heights attained by the Fe_3O_4-γ-Fe_2O_3 FNPs film in this study are lower.

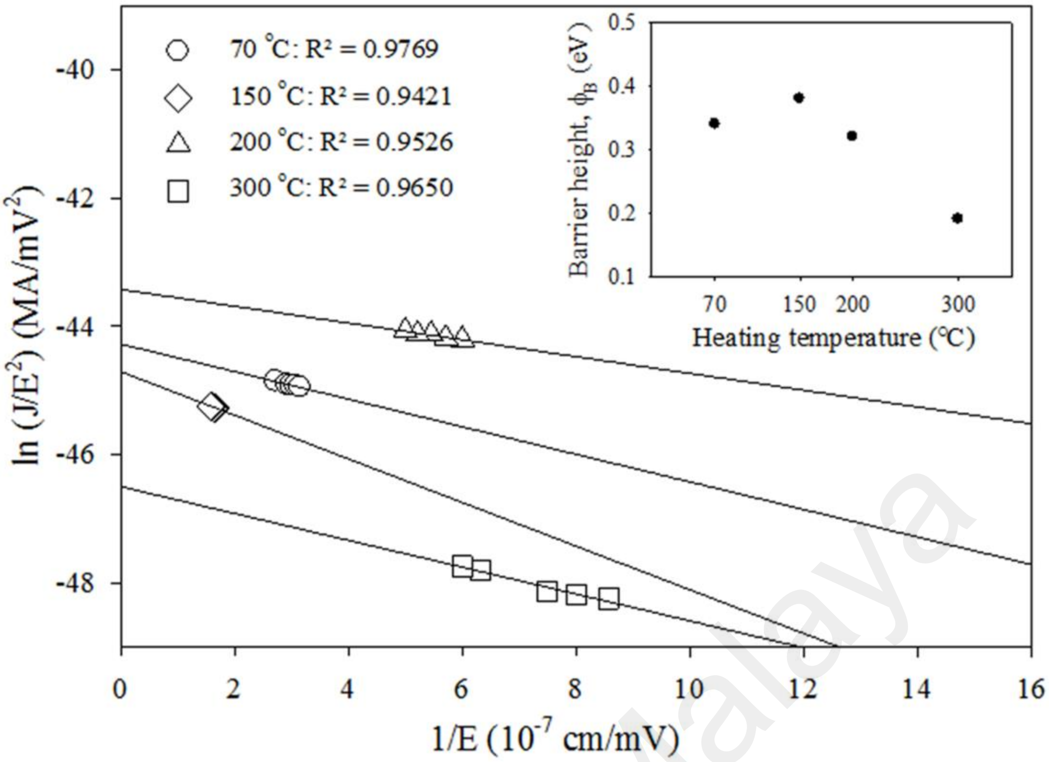

Figure 4.17: FN tunneling linear regression plot [ln(J/E2) – 1/E] of the as prepared films. The inset displays the barrier heights as a function of heating temperatures of the samples

Overall, functionalizing Fe_3O_4-γ-Fe_2O_3 with 4-pentynoic acid does not pose significantly favorable criteria to the capacitor in terms of oxide breakdown field and barrier height despite the kinetically stable self-assembly owing to the Si-O-C covalent bond. The Si-OH defects might be the factor that depreciate the oxide breakdown field, hence the unimpressive barrier heights generally, for all samples.

CHAPTER 5: CONCLUSIONS AND RECOMMENDATIONS

5.1 Conclusions

In the first part of the study, investigation on relationship between ex-situ modifications of synthesized iron oxide nanoparticles (FNPs) using different oleic acid concentrations with the functionalization of 4-pentynoic acid was performed. As oleic acid concentrations increased prior ex-situ modification, mean lattice constants shifted to more magnetite prominent. At limited concentration of surfactant (0.2 g/g oleic acid to iron oxide), the size of FNPs tends to become bigger than the bare iron oxide or the ones that were ex-situ coated with higher concentration of oleic acid. Monolayer oleic acid-coated iron oxide FNPs was produced for the functionalization of 0.2 g/g oleic acid to iron oxide. Whereas the higher concentration of oleic acid produced bilayer oleic acid-coated iron oxide FNPs with interpenetration layer formed between hydrophobic tails of the primary layer and secondary layer oleic acid. Hence, functionalization of 4-pentynoic acid was only successful for the bilayer oleic acid-coated iron oxide FNPs since the 4-pentynoic acid would only bind to the hydrophilic head of the secondary layer oleic acid. Moreover, stability of the NPs and FNPs in polar medium at pH 12 varied at encouraging zeta potentials of -42 to -75 mV. The mean hydrodynamic particle size distributions of the NPs and FNPs were achieved at approximately 35-48 nm. In this study, the main key to a successful functionalization of 4-pentynoic acid to the oleic acid-coated iron oxide FNPs is the concentration of oleic acid prior ex-situ modification. This is essential as the 4-pentynoic acid acts as the prime mover of the iron oxide nanoparticles’ development on silicon substrate. Sample P-O.4 is the best sample to which 0.4 g/g oleic acid to iron oxide concentration permits the sample to achieve the most optimum dispersity in aqueous medium. Moreover, taking into accounts of its successful 4-pentynoic acid functionalization, sample P-0.4 was chosen for self-assembly on SiO_2/n-Si structure in the second part.

In the second part of the study, investigation on association between self-assembly of 4-pentynoic acid functionalized Fe_3O_4-γ-Fe_2O_3 FNPs (thickness 12.6 μm) on SiO_2/n-Si structure with oxide breakdown field and barrier heights were executed. The self–assembly was immensely affected by different temperatures of heat treatments (70-300 ˚C). Crystallite sizes of the FNPs were characterized at 8 ± 1 nm for all samples. The growth of SiO_2 was proportional to the increased heating temperature. Self-assembly of the FNPs resulted in covalent Si-O-C linkages. Samples heated at 150 ˚C and 70 ˚C displayed more prominent intensities of Si-O-C vibrational IR bands than the other samples, signifying that the two samples possess the most coverage of Si-O-C linkages across their substrates and the most successful self-assembly of Fe_3O_4-γ-Fe_2O_3 FNPs. Contrarily, samples heated at 300 ˚C and 200 ˚C displayed weaker intensities of Si-O-C, C=O, and C-O vibrational stretch. These denote that the respective samples experienced physisorbed surfactants disintegration. Moreover developments of Si-OH defects were also intensified with increasing temperature. Saturation magnetization (M_s) of the as prepared film (sample heated at 300 ˚C) was achieved at 71.527 $A{\cdot}m^2/kg$ with coercivity (H_{ci}) of 929.942 A/m. The deposited FNPs film on Si substrate (heated at 300 ˚C) has higher values of M_s and H_{ci} (58.002 $A{\cdot}m^2/kg$) and (861.267 A/m) respectively than the bulk FNPs, owing to the physisorbed surfactants disintegration. The highest root mean square (RMS) roughness was accredited to the sample heated at 150 ˚C (18.12 ± 7.13 nm), whereas the lowest RMS roughness was obtained by the sample heated at 200˚C (12.99 ± 4.39 nm) with more or less the same value as the sample heated at 300 ˚C (13.58 ± 4.03 nm). The FNPs were deposited in a non-uniform aggregation across the Si surface. The resulted coarse surface of the aggregated Fe_3O_4-γ-Fe_2O_3 FNPs film explains the extensive value of RMS roughness generally for all samples. Besides, the Si-O-C linkages and RMS roughness play major roles in electrical properties of the samples. J-E characteristics extracted from I-V curves showed that sample heated at 150 ˚C with the most developed Si-O-C linkages and the highest RMS roughness displayed the highest breakdown field (E_B) and the highest barrier height (ϕ_B) at 2.58 x 10^{-3} MV/cm and 0.38 eV respectively. The highest RMS roughness corresponds to the greatest aggregation (generated by hydrophobic interactions) of the FNPs hence the closest approximation of each FNP to another. Self-assembly of the FNPs induced chemical interactions (covalent Si-O-C) at the interfaces of the film and substrate. These encouraged better energy level alignment and improved charge injection. On the other hand, sample heated at 300 ˚C with differing characteristics showed the lowest E_B (1.08 x 10^{-3} MV/cm) and ϕ_B (0.19 eV). In a nutshell, while heat treatment at 150 ˚C gave the best morphological and surface characteristics for electrical properties of the film, increasing heat treatments to 200-300 ˚C evoked several interrelated detrimental effects; physisorbed surfactants disintegration, breaking down of Si-O-C linkages and more formations of Si-OH defects, less aggregation of FNPs, as well as depletion of surface roughness. All of these caused reduction of breakdown field and barrier height.

In conclusion, coating 0.4 g/g oleic acid to iron oxide concentration on the Fe_3O_4-γ-Fe_2O_3 enables the FNPs to achieve the most optimum dispersity in aqueous medium and also encourages successful functionalization of 4-pentynoic acid. Whereas, 150 ˚C is the best self-assembly temperature that gives the highest oxide breakdown field and barrier height of the Fe_3O_4-γ-Fe_2O_3 FNPs/SiO_2/n-Si capacitor.

5.2 Recommendations for Future Research

Since this study evaluates oxide breakdown field of the metal oxide semiconductor structure, it is recommended that further studies be carried out on measuring the thickness of SiO_2 using transmission electron microscopy. This way, thickness of Fe_3O_4-γ-Fe_2O_3 FNPs film together with SiO_2 can be used in attaining more precise oxide breakdown field and barrier height.

REFERENCES

Ali, K., Sarfraz, A.K., Mirza, I.M., Bahadur, A., Iqbal, S., & ul Haq, A. (2015). Preparation of superparamagnetic maghemite (γ-Fe_2O_3) nanoparticles by wet chemical route and investigation of their magnetic and dielectric properties. *Current Applied Physics, 15*: 925-929.

Aliakbari, A., Seifi, M., Mirzaee, S., & Hekmatara, H. (2015). Influence of different synthesis conditions on properties of oleic acid-coated-Fe_3O_4 nanoparticles. *Materials Science-Poland, 33*(1): 100-106.

Altavilla, C., Ciliberto, E., Gatteschi, D., & Sangregorio, C. (2005). A New Route to Fabricate Monolayers of Magnetite Nanoparticles on Silicon. *Advanced Materials, 17*: 1084-1087.

Andrade, A.L., Valente, M.A., Ferreira, J.M.F., & Fabris, J.D. (2012). Preparation of size-controlled nanoparticles of magnetite. *Journal of Magnetism and Magnetic Materials, 324*(10): 1753-1757.

Beigel, J. (2013). *Doing more with less drives miniaturization of next generation electronic components*. Retrieved November 28, 2016, from http://www.sensorsmag.com/sensors-mag/it-s-small-world-and-getting-smaller-12519.

Benitez, M.J., Szary, P., Mishra, D., Feyen, M., H. Lu, A., Petracic, O., & Zabel, H. (2010). *Templated self-assembly of iron oxide nanoparticles*, Retrieved January 8, 2015, from https://arxiv.org/abs/1010.4166 database.

Bronstein, L.M., Huang, X., Retrum, J., Schmucker, A., Pink, M., Stein, B.D., & Dragnea, B. (2007). Influence of Iron Oleate Complex Structure on Iron Oxide Nanoparticle Formation. *Chemistry of Materials, 19*: 3624-3632.

Çapan, I., Tanmcr, C., Hassan, A.K., Tannsever, T. (2009). Characterisation and optical vapour properties of PMMA thin films. *Materials Science and Engineering C, 29*: 140-143.

Çaldıran, Z., Deniz, A.R., Şahin, Y., Metin, Ö., Meral, K., & Aydoğan, Ş. (2013). The electrical characteristics of the Fe_3O_4/Si junctions. *Journal of Alloys and Compounds*, *552*: 437-442.

Camponeschi, E., Walker, J., Garmestani, H., & Tannenbaum, R. (2008). Surfactant effects on the particle size of iron (III) oxides formed by sol–gel synthesis. *Journal of Non-Crystalline Solids, 354*(34): 4063-4069.

Cao, L., Chai, Y., Li, P., Shen, Z., & Wu, J. (2005). Efficient self-assembly of transition metal oxide nanoclusters on silicon substrates. *Thin Solid Films, 492*(1-2): 13-18.

Castelló, J., Gallardo, M., Busquets, M.A., & Estelrich, J. (2015). Chitosan (or alginate)-coated iron oxide nanoparticles: A comparative study. *Colloids and Surfaces A: Physicochemical and Engineering Aspects, 468*: 151-158.

Cattaruzza, F., Cricenti, A., Flamini, A., Girasole, M., Longo, G., Mezzi, A., & Prosperi, T. (2004). Carboxylic acid terminated monolayer formation on crystalline silicon and silicon nitride surfaces. A surface coverage determination with a fluorescent probe in solution. *Journal of Materials Chemistry, 14*: 1461-1468.

Cattaruzza, Fiorani, D., Flamini, A., Imperatori, P., Scavia, G., Suber, L., & Testa A.M. (2005). Magnetite Nanoparticles Anchored to Crystalline Silicon Surfaces. *Chemistry materials, 17*(12): 331-3316.

Chin, A.B., Yaacob, I.I. (2007). Synthesis and characterization of magnetic iron oxide nanoparticles via w/o microemulsion and Massart's procedure. *Journal of Materials Processing Technology, 191*: 235-237.

Chowdhury, S.R., & Yanful, E.K. (2013). Kinetics of cadmium(II) uptake by mixed maghemite-magnetite nanoparticles. *Journal of Environment Management, 129*: 642-651.

Chowdhury, S.R., & Yanful, E.K. (2010). Arsenic and chromium removal by mixed magnetite-maghemite nanoparticles and the effect of phosphate on removal. *Journal of Environment Management, 91*: 2238-2247.

Chowdhury, S.R., Yanful, E.K., & Pratt, A.R. (2012). Chemical states in XPS and Raman analysis during removal of Cr(VI) from contaminated water by mixed maghemite-magnetite nanoparticles. *Journal of Hazardous materials, 235-236*: 246-256.

Ciampi, S., Harper, J.B., & Gooding, J.J. (2010). Wet Chemical Routes to the Assembly of Organic Monolayers on Silicon Surfaces via the Formation of Si-C Bonds: Surface Preparation, Passivation and Functionalization. *Chemical Society Reviews, 39*: 2158−2183.

Cibert, J., Bobo, J.-F., & Lüders, U. (2005). Development of new materials for spintronics. *Comptes Rendus Physique, 6*(9): 977-996.

Clark, S.J. & Robertson, J. (2007). Band gap and Schottky barrier heights of multiferroic $BiFeO_3$. *Applied Physics Letters, 90*: 132903.

Cummings, S.P., Savchenko, J., & Ren, T. (2011). Functionalization of Flat Si Surfaces with Inorganic Compounds - Towards Molecular CMOS Hybrid Devices. *Coordination Chemistry Reviews, 255*: 1587-1602.

Darroudi, M., Hakimi, M., Goodarzi, E., & Kazemi, O.R. (2014). Superparamagnetic iron oxide nanoparticles (SPIONs): Green preparation, characterization and their cytotoxicity effects. *Ceramics International, 40*(9): 14641-14645.

DeBenedetti, W.J.I. & Chabal, Y.J. (2013). Functionalization of Oxide-Free Silicon Surfaces. *Journal of Vacuum Science and Technology A, 31*: 050826.

Deniz, A.R., Caldiran, Z., Metin, O., Meral, K. & Aydogan, S. (2016). The investigation of the electrical properties of Fe_3O_4/n-Si heterojunctions in a wide temperature range. *Journal of Colloid and Interface Science, 473*: 172-181.

Deniz, A.R., Çaldıran, Z., Şahin, Y., Şinoforoğlu, M., Metin, O., Meral, K., & Aydoğan S. (2013). The Synthesis of the Fe_3O_4 Nanoparticles and the Analysis of the Current–Voltage Measurements on Au/ Fe_3O_4/p-Si Schottky Contacts in a Wide Temperature Range. *Metallurgical and Materials Transactions A: Physical Metallurgy and Materials Science, 44*: 3809-3814.

Do, B.P.H., Nguyen, B.D., Nguyen, H.D. & Nguyen, P.T. (2013). Synthesis of magnetic composite nanoparticles enveloped in copolymers specified for scale inhibition application. *Advances in Natural Sciences: Nanoscience and Nanotechnology, 4*: 045016.

El-Shahawy, M.A. (1999). Polymethyl methacrylate mixtures with some organic laser dyes: I. Dielectric response. *Polymer testing, 18*: 389-396.

Faria, D.L.A., Venaüncio, S., Oliveira, M.T. (1997). Raman microspectroscopy of some iron oxides and oxyhydroxides. *Journal of Raman Specroscopy, 28*: 873-878.

Finsy, R. (1994). Particle sizing by quasi-elastic light scattering. *Advances in Colloid and Interface Science, 52*: 79-143.

Ghosh, S., & Srıvastava, P.C. (2014). Interface states of Fe_3O_4/Si interfacial structure and effect of magnetic field. *Journal of Electronic Materials, 43*: 4357-4363.

Goh, K.H., Haseeb, A.S.M.A., & Wong, Y.H. (2016). Physical and electrical properties of thermal oxidized Sm_2O_3 gate oxide thin film on Si substrate: Influence of oxidation durations. *Thin Solid Films, 606*: 80-86.

Goswami, M.M., Dey, C., Bandyopadhyay, A., Sarkar, D., & Ahir, M. (2016). Micelles driven magnetite (Fe_3O_4) hollow spheres and a study on AC magnetic properties for hyperthermia application. *Journal of Magnetism and Magnetic Materials, 417*: 376-381.

Graham, U. & Ian, C. (1996). *Understanding Statistics* (p. 55). United Kingdom: Oxford University Press.

Greaves, C. (1983). A powder neutron diffraction investigation of vacancy ordering and covalence in γ-Fe_2O_3. *Journal of Solid State Chemistry, 49*: 325-333.

Guo, C., Hu, Y., Qian, H., Ning, J., & Xu, S. (2011). Magnetite (Fe_3O_4) tetrakaidecahedral microcrystals: Synthesis, characterization, and micro-Raman study. *Materials Characterization, 62*: 148-151.

Guo T.L., & Ying, H. (2002). Synthesis of polymaleimide/silica nanocomposites. *Journal of Materials Science, 37*: 2305-2309.

Hackley, V.A. & Clogston, J.D. (2011). *Measuring the Hydrodynamic Size of Nanoparticles in Aqueous Media Using Batch-Mode Dynamic Light Scattering* (pp. 35-52). Totowa: Humana Press.

Hanesch, M. (2009). Raman spectroscopy of iron oxides and (oxy)hydroxides at low laser power and possible applications in environmental magnetic studies. *Geophysical Journal International, 177*: 941-948.

Hasegawa, M., Yanagihara, H., Toyoda, Y., Kita, E., & Ranno, L. (2007). Electrical and magnetic properties of Fe_2O_3 epitaxial films. *Journal of Magnetism and Magnetic Materials, 310*: 2283-2285.

Herzer, N., Hoeppener, S., & Schubert, U.S. (2010). Fabrication of Patterned Silane Based Self-Assembled Monolayers by Photolithography and Surface Reactions on Silicon-Oxide Substrates. *Chemical Communications, 46*: 5634-5652.

Hosseini-Monfared, H., Parchegani, F., & Alavi, S. (2015). Carboxylic acid effects on the size and catalytic activity of magnetite nanoparticles. *Journal of Colloid and Interface Science, 437*: 1-9.

Hunter, R.J. (1988). *Zeta Potential in Colloid Science: Principles and Application* (p. 239). United Kingdom: Academic Press.

Jeong, U., Teng, X., Wang, Y., Yang, H., & Xia, Y. (2007). Superparamagnetic Colloids: Controlled Synthesis and Niche Applications. *Advanced Materials, 19*: 33-60.

Ji, S., Wan, L., Liu, C-C., & Nealey P.F. (2016). Directed self-assembly of block copolymers on chemical patterns: A platform for nanofabrication. *Progress in Polymer Science, 54-55*: 76-127.

Jiang, F., Li, X., Zhu, Y., & Tang, Z. (2014). Synthesis and magnetic characterizations of uniform iron oxide nanoparticles. *Physica B: Condensed Matter, 443*: 1-5.

Kavas, H., Durmus, Z., Baykal, A., Aslan, A., Bozkurt, A., & Toprak, M.S. (2010). Synthesis and conductivity evaluation of PVTri–Fe_3O_4 nanocomposite. *Journal of Non-Crystalline Solids, 356*(9-10): 484-489.

Khalil, M., Yu, J., Liu, N., & Lee, R. (2014). Non-aqueous modification of synthesized hematite nanoparticles with oleic acid. *Colloids and Surfaces A: Physicochemical and Engineering Aspects, 453*: 7-12.

Khorsand Zak, A., Abd. Majid, W.H., Abrishami, M.E., & Yousefi, R. (2011). X-ray analysis of ZnO nanoparticles by Williamson–Hall and size–strain plot methods. *Solid State Sciences, 13*(1): 251-256.

Kim, T.G., Jeong, E.H., Lim, S.C., Kim, S.H., Kim, G.H., Kim, S.H., Jeon, H.Y., & Youk, J.Y. (2009). PMMA-based patternable gate insulators for Organic thin-film transistors. *Synthetic Metals, 159*: 749 753.

Kim, W., Suh, C.Y., Cho, S.W., Roh, K.M., Kwon, H., Song, K., & Shon, I.J. (2012). A new method for the identification and quantification of magnetite-maghemite mixture using conventional X-ray diffraction technique. *Talanta, 94*: 348-352.

Kotnala, R.K. & Shah, J. (2015). *Chapter 4 - Ferrite Materials, Nano to Spintronics Regime in Handbook of Magnetic Materials* (p. 291). Amsterdam: Elsevier.

Lee, K.U., Kim, M.J., Park, K.J., Kim, M., Kwon, O.J., & Kim, J.J. (2014). Catalytic growth of a colloidal carbon sphere by hydrothermal reaction with iron oxide (Fe_3O_4) catalyst. *Materials Letters, 125*: 213-217.

Lemine, O., Omri, K., Zhang, B., El Mir, L., Sajieddine, M., Alyamani, A., & Bououdina, M. (2012). Sol–gel synthesis of 8 nm magnetite (Fe_3O_4) nanoparticles and their magnetic properties. *Superlattices and Microstructures, 52*: 793-799.

Li, Y., Calder, S., Yaffe, O., Cahen, D., Haick, H., Kronik, L., & Zuilhof, H. (2012) Hybrids of Organic Molecules and Flat, Oxide-Free Silicon: High-Density Monolayers, Electronic Properties, and Functionalization. *Langmuir, 28*: 9920−9929.

Li, Y.-S., Church, J.S., & Woodhead, A.L. (2012). Infrared and Raman spectroscopic studies on iron oxide magnetic nano-particles and their surface modifications. *Journal of Magnetism and Magnetic Materials*, *324*(8): 1543-1550.

Li, Y.S., Church, J.S., Woodhead, A.L., & Moussa F. (2010). Preparation and characterization of silica coated iron oxide magnetic nano-particles. *Spectrochimica Acta, Part A, 76*: 484-489.

Li, L., Gao, P., Gai, S., He, F., Chen, Y., Zhang, M., & Yang, P. (2016). Ultra-small and highly dispersed Fe_3O_4nanoparticles anchored on reduced graphene for supercapacitor application. *Electrochimica Acta, 190*: 566-573.

Li, S., Zhang, T., Tang, R., Qiu, H., Wang, C., & Zhou, Z. (2015*).* Solvothermal synthesis and characterization of monodisperse superparamagnetic iron oxide nanoparticles. *Journal of Magnetism and Magnetic Materials, 379*: 226-231.

Lin, S., Lin, K., Lu, D., Liu, Z. (2017). Preparation of uniform magnetic iron oxide nanoparticles by co-precipitation in a helical module microchannel reactor. *Journal of Environmental Chemical Engineering, 5*: 303-309.

Linford, M.R. & Chidsey, C.E.D. (1993). Alkyl Monolayers Covalently Bonded to Silicon Surfaces. *Journal of the American Chemical Society, 115*: 12631-12632.

Liu, T., Zhang, X., Li, B., Ding, J., Liu, Y., Li, G., Meng, X., Cai, Q., & Zhang, J. (2014). Fabrication of quasi-cubic Fe_3O_4@rGO composite via a colloid electrostatic self-assembly process for supercapacitors. *RSC Advances, 4(*92): 50765-50770.

Lu, A.H., Salabas, E.L., & Schuth, F. (2007). Magnetic nanoparticles: synthesis, protection, functionalization, and application. *Angewandte Chemie International Edition, 46*(8): 1222-44.

Lu, G. (2006). Synthesis of self-assembled iron silicon oxide nanowires onto single-crystalline Si(100). *Journal of applied polymer science, 102*: 52-57.

Lu, Y. & Miller, J.D. (2002). Carboxyl Stretching Vibrations of Spontaneously Adsorbed and LB-Transferred Calcium Carboxylates as Determined by FTIR

Internal Reflection Spectroscopy. *Journal of Colloid and Interface Science, 256*(1): 41-52.

Ma, F.X., Hu, H., Wu, H.B., Xu, C.Y., Xu, Z., Zhen, L., & David L.X.W. (2015). Formation of Uniform Fe_3O_4 Hollow Spheres Organized by Ultrathin Nanosheets and Their Excellent Lithium Storage Properties. *Advanced Materials, 27*(27): 4097-101.

Maenosono, S., Okubo, T., & Yamaguchi, Y. (2003). Overview of nanoparticle array formation by wet coating. *Journal of Nanoparticle Research, 5*: 5-15.

Mahmed, N., Heczko O., Lancok A., & Hannula, S. (2014). The magnetic and oxidation behavior of bare and silica-coated iron oxide nanoparticles synthesized by reverse co-precipitation of ferrous ion (Fe^{2+}) in ambient atmosphere. *Journal of Magnetism and Magnetic Materials, 353*: 15-22.

Majee, S., Cerqueira, M.F., Tondelier, D., Geffroy, B., Bonnassieux, Y., Alpuim, P., & Bourée, J.E. (2015). Flexible organic–inorganic hybrid layer encapsulation for organic opto-electronic devices. *Progress in Organic Coatings, 80*: 27-32.

de Mierry, P., Ballutaud, D., Aucouturier, M., & Etcheberry, A. (1990). Effect of Surface Preparations on Electrical and Chemical Surface Properties of P-Type Silicon. *Journal of the Electrochemical Society, 137*: 2966-2973.

Miozzo, L., Yassar, A., & Horowitz, G. (2010). Surface engineering for high performance organic electronic devices: the chemical approach. *Journal of Materials Chemistry, 20*: 2513-2538.

Mir, N., Bahrami, M., Safari, E., & Hosseinpour-Mashkani, S.M. (2014). Fluorescent Superparamagnetic γ-Fe_2O_3 Hollow Nanoparticles: Synthesis and Surface Modification by One-Pot Co-precipitation Method. *Journal of Cluster Science, 26*: 1103-1113.

Morales-Acosta, M.D., Alvarado-Beltrán, C.G., Quevedo-López, M.A., Gnade, B.E. Mendoza-Galván, A., & Ramírez-Bon, R. (2013). Adjustable structural, optical and dielectric characteristics in sol–gel PMMA–SiO_2 hybrid films. *Journal of Non-Crystalline Solids, 362*: 124-135.

Mote, V., Purushotham, Y., & Dole, B. (2012). Williamson-Hall analysis in estimation of lattice strain in nanometer-sized ZnO particles. *Journal of Theoretical and Applied Physics, 6*(6): 1-8.

Muñoz-Noval, A., Rubio-Zuazo, J., Salas-Colera, E., Serrano, A., Rubio-Marcos, F., &Castro, G.R. (2015). Large coincidence lattice on Au/Fe_3O_4 incommensurate structure for spintronic applications. *Applied Surface Science, 355*: 698-701.

Nadeem, K., Ali, L., Gul, I., Rizwan, S., & Mumtaz, M. (2014). Effect of silica coating on the structural, dielectric, and magnetic properties of maghemite nanoparticles. *Journal of Non-Crystalline Solids, 404:* 72-77.

Nakata, K., Ohji, M., Ikuno, Y., Kusaka, S., Gomi, F., Kamei, M., Ross, D.F., Tano, & Y. (2004). Wide-angle viewing lens for vitrectomy. *American Journal of Ophthalmology, 137*: 760-762.

Némethová, V., Buliaková, B., Mazancová, P., Bábelová, A., Šelc, M., Moravčíková, D., Kleščíková, L., Ursínyová, M., Gábelová, A., & Rázga, F. (2017). Intracellular uptake of magnetite nanoparticles: A focus on physico-chemical characterization and interpretation of in vitro data. *Materials Science and Engineering C, 70*: 161.

Neamen, D.A. (2012). *Semiconductor Physics and Devices: Basic Principles* (4th ed.). New York: Mc-Graw Hill.

Ng, A., Ciampi, S., James, M., Harper, J.B., & Gooding, J.J. (2009). Comparing the Reactivity of Alkynes and Alkenes on Silicon (100) Surfaces. *Langmuir, 25*: 13934-13941.

Oh, I., Kim, M., & Kim, J. (2015). Fe_3O_4 /carbon coated silicon ternary hybrid composite as supercapacitor electrodes. *Applied Surface Science, 328*: 222-228.

Onclin, S., Ravoo, B.J., & Reinhoudt, D.N. (2005). Engineering Silicon Oxide Surfaces Using Self-Assembled Monolayers. *Angewandte Chemie International Edition, 44*: 6282-6304.

Pang, Y.L., Lim, S., Ong, H.C., & Chong, W.T. (2016). Research progress on iron oxide-based magnetic materials: Synthesis techniques and photocatalytic applications. *Ceramics International, 42*(1): 9-34.

Pavia, D.L., Lampman, G.M., & Kriz, G.S. (1996). *Introduction to Spectroscopy* (2nd ed.) (p. 73). New York: Harcourt College Pub.

Petcharoen, K. & Sirivat, A. (2012). Synthesis and characterization of magnetite nanoparticles via the chemical co-precipitation method. *Materials Science and Engineering: B*, 177(5): 421-427.

Pichon, B., Buchwalter, P., Carcel, C., Cattoën, X., Man, M.W.C., & Begin-Colin, S. (2012). Assembling of Magnetic Iron Oxide Nanoparticles Controlled by Self Assembled Monolayers of Functional Coordinating or Chelating Trialkoxysilanes. *The Open Surface Science Journal, 4*: 35-41.

Prabhakaran, K., Watanabe, Y., Nath, K.G., Homma, Y., Ogino, T., Shafi, K.V.P.M. & Ulman, A. (2003). Surface chemistry of Fe_2O_3 nanoparticles on ultrathin oxide layers on Si and Ge. *Surface Science, 545*(3): 191-198.

Puigdollers, J., Voz, C., Orpella, A., Quidant, R., Martín, I., Vetter, M., & Alcubilla, R., 2004. Pentacene thin-film transistors with polymeric gate dielectric. *Organic Electronics, 5*: 67-71.

Pujari, S.P., Scheres, L., Marcelis, A.T.M., Zuilhof, H. (2014). Covalent Surface Modification of Oxide Surfaces. *Angewandte Chemie International Edition, 53*: 6322-6356.

Pujari, S.P., Spruijt, E., Cohen Stuart, M.A., van Rijn, C.J., Paulusse, J.M., & Zuilhof, H. (2012). Ultralow adhesion and friction of fluoro-hydro alkyne-derived self-assembled monolayers on H-terminated Si(111). *Langmuir, 28*: 17690-17700.

Qian, Z., Zhang, Z., & Chen, Y. (2008). A novel preparation of surface-coated paramagnetic magnetite/polystyrene nanocomposite microspheres by radiation-induced miniemulsion polymerization. *Journal of Colloid and Interface Science, 327*: 354-361.

Raman, R.K.S., Gleeson, B., & Young, D.J. (1998). Laser Raman-Spectroscopy-A Technique for Rapid Characterization of Oxide Scale Layers. *Materials Science and Technology, 14*: 373-376.

Ramimoghadam, D., Bagheri, S., & Hamid, S. (2014). Progress in electrochemical synthesis of magnetic iron oxide nanoparticles. *Journal of Magnetism and Magnetic Materials, 368*: 207-229.

Rehana, D., Haleel, A.K., & Rahiman, A.K. (2015). Hydroxy, carboxylic and amino acid functionalized superparamagnetic iron oxide nanoparticles: Synthesis, characterization and in vitro anti-cancer studies. *Journal of Chemical Sciences, 127*(7): 1155-1166.

Roth, H., Schwaminger, S., Schindler, M., Wagner, F., & Berensmeier, S. (2015). Influencing factors in the Co-precipitation process of superparamagnetic iron oxide nano particles: A model based study. *Journal of Magnetism and Magnetic Materials, 377*: 81-89.

Ruhai, T., Oliver, S., Meng, L., Wenchuang (Walter) H., Yves, J.C., & Jinming, G. (2010). Infrared Characterization of Interfacial Si-O Bond Formation on Silanized Flat SiO_2/Si Surfaces. *Langmuir, 26*: 4563-4566.

Šutkaa, A., Lagzdinaa, S., Juhnevicaa, I., & Jakovlevsb, D. (2014). Precipitation synthesis of magnetite Fe_3O_4 nanoflakes. *Ceramics International, 40*: 11437-11440.

Sarantopoulou, E., Kovač, J., Pispas, S., Kobe, S., Kollia, Z., & Cefalas, A.C. (2008). Self-assembled ferromagnetic and superparamagnetic structures of hybrid Fe block copolymers. *Superlattices and Microstructures, 44*: 457-467.

Schroder, D.K. (2006). *Semiconductor Material and Device Characterization* (3rd ed.) (pp. 127-184). New Jersey, United States: John Wiley & Sons, Inc.

Scheres, L., Giesbers, M., Zuilhof, H. (2010). Organic Monolayers onto Oxide-Free Silicon with Improved Surface Coverage: Alkynes versus Alkenes. *Langmuir, 26*: 4790-4795.

Scheres, L., Rijksen, B., Giesbers, M., Zuilhof, H. (2011). Molecular Modeling of Alkyl and Alkenyl Monolayers on Hydrogen-Terminated Si(111). *Langmuir, 27*: 972-980.

Shete, P., Patil, R., Tiwale, B., & Pawar, S. (2015.) Water dispersible oleic acid-coated Fe_3O_4 nanoparticles for biomedical applications. *Journal of Magnetism and Magnetic Materials, 377*: 406-410.

Sieval, A.B., Van den Hout, B., Zuilhof, H., Sudhölter, E.J.R. (2001). Molecular Modeling of Covalently Attached Alkyl Monolayers on the Hydrogen-Terminated Si(111) Surface. *Langmuir, 17*: 2172-2181.

Singh, G., Chan, H., Udayabhaskararao, T., Gelman, E., Peddis, D., Baskin, A., Leitus, G. Kral, P. & Klajn, R. (2015). Magnetic field-induced self-assembly of iron oxide nanocubes. *Faraday Discuss, 181*: 403-21.

Skoog, D.A., Holler, F.J., Crouch, S.R. (2007). *Principles of Instrumental Analysis* (6th ed.) (pp. 516-517). Belmont: Thomson Brooks/Cole.

Smith, W.F. & Hashemi, J. (2006). *Foundations of Materials Science and Engineering* (4th ed.) Boston: McGraw Hill.

Soares, P., Alves, A., Pereira, L., Coutinho, J., Ferreira, I., Novo, C., & Borges, J. (2014). Effects of surfactants on the magnetic properties of iron oxide colloids. *Journal of Colloid and Interface Science, 419*: 46-51.

Sun, S. (2006). Recent Advances in Chemical Synthesis, Self-Assembly, and Applications of FePt Nanoparticles. *Advanced Materials, 18*: 393-403.

Swygenhoven, H.V. & Derlet, P. (2001). Grain-boundary sliding in nanocrystalline fcc metals. *Physical Review B, 64*: 224105-1-224105-9.

Tangwatanakul, W., Sirisathitkul, C., Limphirat, W., Yimnirun, R. (2017). Synchrotron Xray absorption of iron oxide (Fe_2O_3) nanoparticles: effects of reagent concentrationand sonication in co-precipitation synthesis. *Chinese Journal of Physics, 55*: 845-852.

Terris, B.D. & Thomson, T. (2005). Nanofabricated and self-assembled magnetic structures as data storage media. *Journal of Physics D: Applied Physics*, *38*(12): R199-R222.

Thissen, P., Seitz, O., & Chaba, Y. (2012). Wet chemical surface functionalization of oxide-free silicon. *Progress in Surface Science, 87*: 272-290.

Ünal, B., Durmus, Z., Baykal, A., Sözeri, H., Toprak, M.S. & Alpsoy, L. (2010). L-Histidine coated iron oxide nanoparticles: Synthesis, structural and conductivity characterization. *Journal of Alloys and Compounds*, *505*(1): 172-178.

Unal, B., Durmus, Z., Kavas, H., Baykal, A., & Toprak, M.S. (2010). Synthesis, conductivity and dielectric characterization of salicylic acid-Fe_3O_4 nanocomposite. *Materials Chemistry and Physics, 123*(1): 184-190.

Upadhyay, S., Parekh, K., & Pandey, B. (2016). Influence of crystallite size on the magnetic properties of Fe_3O_4 nanoparticles. *Journal of Alloys and Compounds, 678*: 478-485.

Vasilopoulou, M., Douvas, A.M., Kouvatsos, D., Argitis, P., Davazoglou, D. (2005). Characterization of various insulators for possible use as low-k dielectrics deposited at temperatures below 200 °C. *Microelectronics Reliability, 45*: 990-993.

Venkateswarlu, K., Bose, A.C., & Rameshbabu, N. (2010). X-ray peak broadening studies of nanocrystalline hydroxyapatite by Williamson-Hall analysis. *Physica B: Condensed Matter, 405*(20): 4256-4261.

Vikulov, V.A., Dimitriev, A.A., Balashev, V.V., Pisarenko, T.A., & Korobtsov, V.V. (2016). Low-temperature conducting channel switching in hybrid Fe_3O_4/SiO_2/n-Si structures. *Materials Science and Engineering B, 211*: 33-36.

Wallart, X., Henry de Villeneuve, C., Allongue, P. (2005). Truly Quantitative XPS Characterization of Organic Monolayers on Silicon: Study of Alkyl and Alkoxy Monolayers on H-Si(111). *Journal of the American Chemical Society, 127*: 7871-7878.

Waldron, R.D. (1955). Infrared Spectra of Ferrites. *Physical Review, 99*: 1727-1735.

Wan, J. Hwang, Amy, F., & Kahn, A. (2005). Impact of electrode contamination on the α-NPD/Au hole injection barrier. *Organic Electronics, 6*: 47-54.

Wang, Q., Jiao, L., Du, H., Wang, Y., & Yuan, H. (2014). Fe_3O_4 nanoparticles grown on graphene as advanced electrode materials for supercapacitors. *Journal of Power Sources, 245*: 101-106.

Wang, X., Song, B., Zhang, Y., Lv, Z., Hu, C., Liu, Z., Wen, J., Sui, Y., Han, Y., Tang, J., and Song, B. (2016). Voltage-controlled magnetoresistance of magnetite film in Fe_3O_4/Si structure at room temperature. *Journal of Alloys and Compounds, 657:* 268-272.

Wasilewski, P., & Kletetschka, G. (1999). Lodestone: Natures only permanent magnet-What it is and how it gets charged. *Geophysical Research Letters, 26*: 2275-2278.

Wu. W., He, Q., & Jiang, C. (2008). Magnetic Iron Oxide Nanoparticles : Synthesis and Surface Functionalization Strategies. *Nanoscale Res Lett, 3*: 397-415.

Yablonovitch, E., Allara, D.L., Chang, C.C., Gmitter, T., Bright, T.B. (1986). Unusually low surface-recombination velocity on silicon and germanium surfaces. *Physical Review Letters, 57*: 249-252.

Yan, F., Ding, J., Liu, Y., Wang, Z., Cai, Q., & Zhang, J. (2015). Fabrication of magnetic irregular hexagonal- Fe_3O_4 sheets/reduced graphene oxide composite for supercapacitors. *Synthetic Metals, 209*: 473-479.

Yanagihara, H., Hasegawa, M., Kita, E., Wakabayashi, Y., Sawa, H., & Siratori, K. (2006). Iron Vacancy Ordered γ-Fe_2O_3(001) Epitaxial Films: The Crystal Structure and Electrical Resistivity. *Journal of the Physical Society of Japan, 75*: 054708-054712.

Yang, K., Kim, D.H., Dho, J. (2011). Schottky barrier effect on the electrical properties Fe_3O_4/ZnO and Fe_3O_4/Nb: $SrTiO_3$ heterostructures. *Journal of Physics D: Applied Physics, 44*: 355301-355306.

Yang, K., Peng, H., Wen, Y., & Li, N. (2010). Re-examination of characteristic FTIR spectrum of secondary layer in bilayer oleic acid-coated Fe_3O_4 nanoparticles. *Applied Surface Science*, *256*: 3093-3097.

Yoon, T., Oh, J., Park, S., Kim, V., Jung, B. G., Min, S., Park, J., Hyeon, T., & Kim, K. (2004). Single and Multile-Step Dip-Coating of Colloidal Maghemite (γ-Fe_2O_3) Nanoparticles onto Si, Si_3N_4, and SiO_2 Substrate. *Advanced Functional Materials*, *14*: 1062-1068.

Yousefi, T., Golikand, A.N., & Mashhadizadeh, M.H. (2013). Synthesis of iron oxide nanoparticles at low bath temperature: Characterization and energy storage studies. *Materials Science in Semiconductor Processing*, *16*(6): 1837-1841.

Yuan, S.-L., Cai, Z.-T., & Jiang, Y.-S. (2003). Molecular Simulation Study of Alkyl Monolayers on the Si(111) Surface. *New Journal of Chemistry*, *27*: 626-633.

Zhang, D., Zang, C., Zhang, Y., Han, Y., Gao, C., Yang, Y., & Yu, K. (2012). Electrical property of nanocrystalline γ-Fe_2O_3 under high pressure. *Physica B*, *407*: 1044-1046.

Zhao, H., Zhou, M., Wen, L., & Lei, Y. (2015). Template-directed construction of nanostructure arrays for highly-efficient energy storage and conversion. *Nano Energy*, *13*: 790-813.

Zetasizer Nano User Manual. (2007). [Brochure]. United Kingdom: Malvern Instruments Ltd.

LIST OF PUBLICATIONS

Baharuddin, A.A., Ang, B.C., Abu Hussein, N.A., Andriyana, A. & Wong, Y.H. (2018). Mechanisms of highly stabilized ex-situ oleic acid-modified iron oxide nanoparticles functionalized with 4-pentynoic acid. *Materials Chemistry and Physics*, *203*: 212-222.

Baharuddin, A.A., Ang, B.C., & Wong, Y.H. (2017). Self-assembly and electrical characteristics of 4-pentynoic acid functionalized Fe_3O_4-γ-Fe_2O_3 nanoparticles on SiO_2/n-Si. *Applied Surface Science*, *423*: 236-244.

APPENDIX A

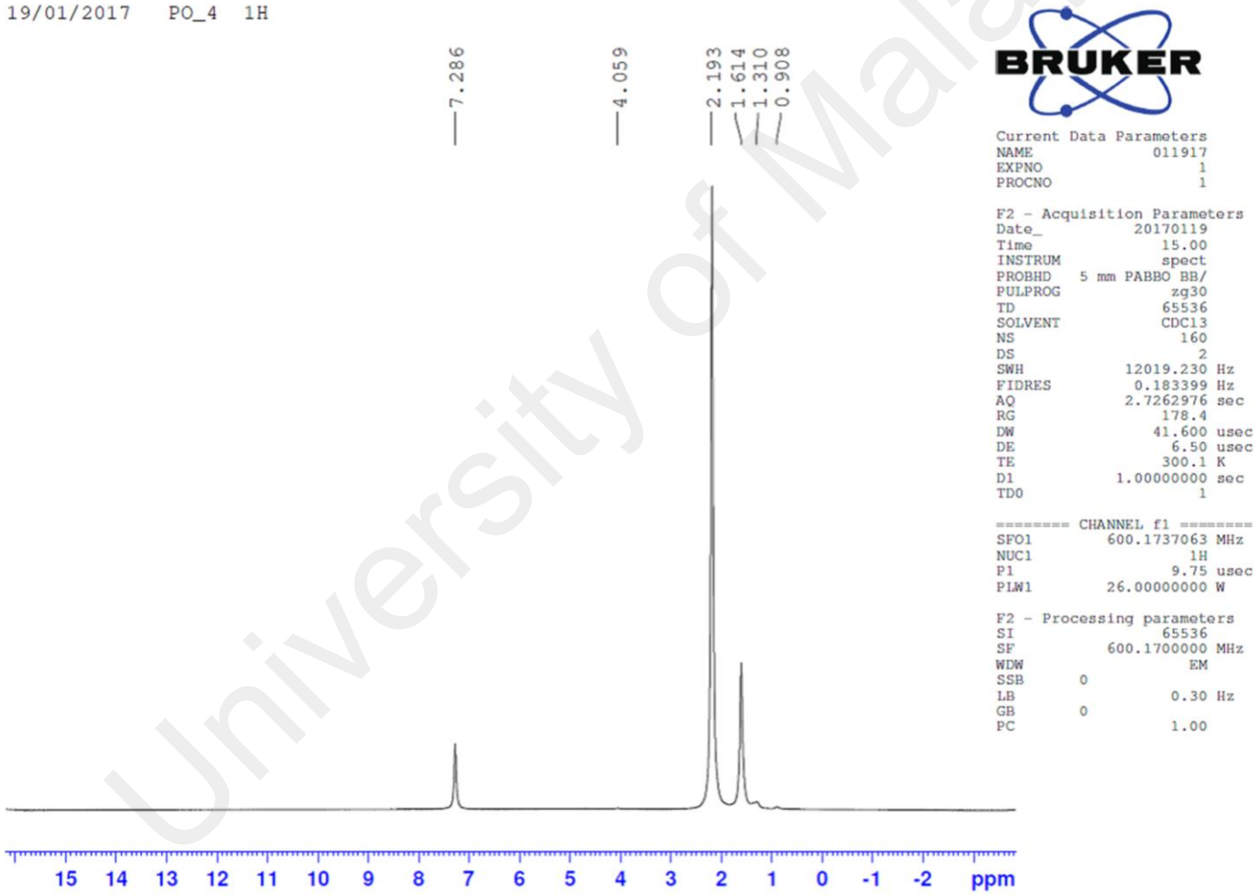

```
Current Data Parameters
NAME              011917
EXPNO                  1
PROCNO                 1

F2 - Acquisition Parameters
Date_           20170119
Time               15.00
INSTRUM            spect
PROBHD   5 mm PABBO BB/
PULPROG             zg30
TD                 65536
SOLVENT            CDCl3
NS                   160
DS                     2
SWH            12019.230 Hz
FIDRES          0.183399 Hz
AQ             2.7262976 sec
RG                 178.4
DW                41.600 usec
DE                  6.50 usec
TE                 300.1 K
D1            1.00000000 sec
TD0                    1

======== CHANNEL f1 ========
SFO1         600.1737063 MHz
NUC1                  1H
P1                  9.75 usec
PLW1         26.00000000 W

F2 - Processing parameters
SI                 65536
SF           600.1700000 MHz
WDW                   EM
SSB       0
LB                  0.30 Hz
GB        0
PC                  1.00
```

Proton NMR of sample P-0.4

APPENDIX B

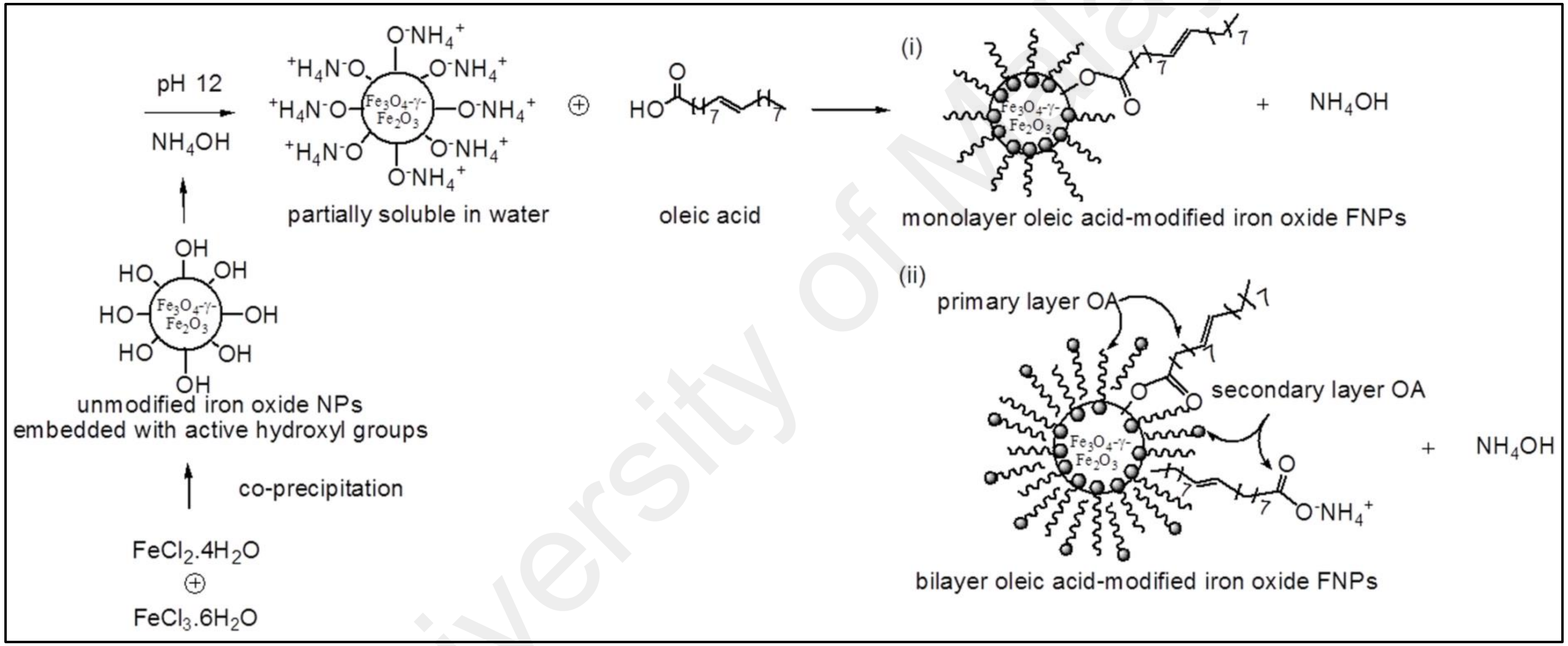

Mechanisms of monolayer and bilayer oleic acid-coated iron oxide FNPs

APPENDIX C

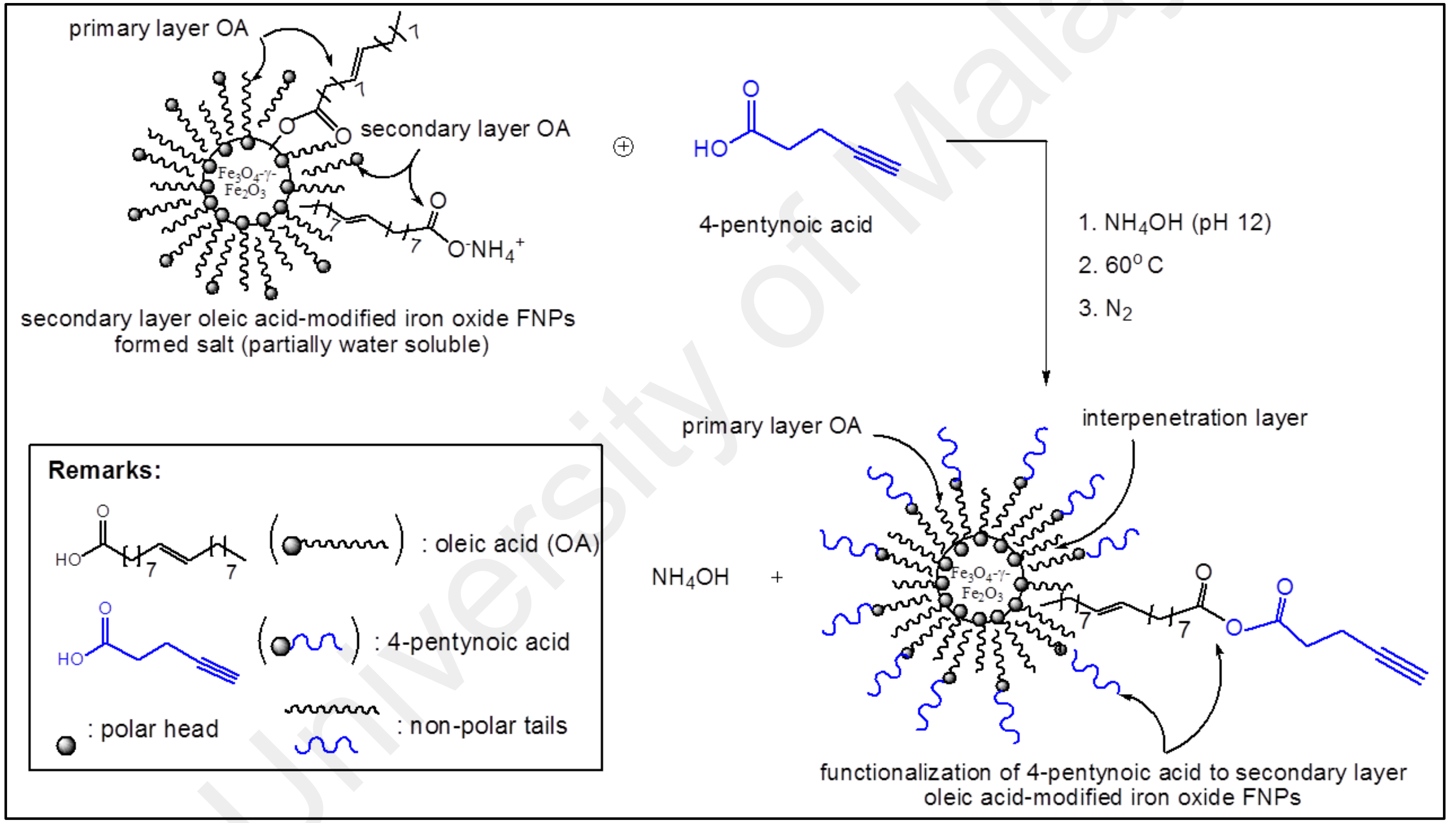

Mechanisms of 4-pentynoic acid functionalization to the bilayer oleic acid-coated iron oxide FNPs

APPENDIX D

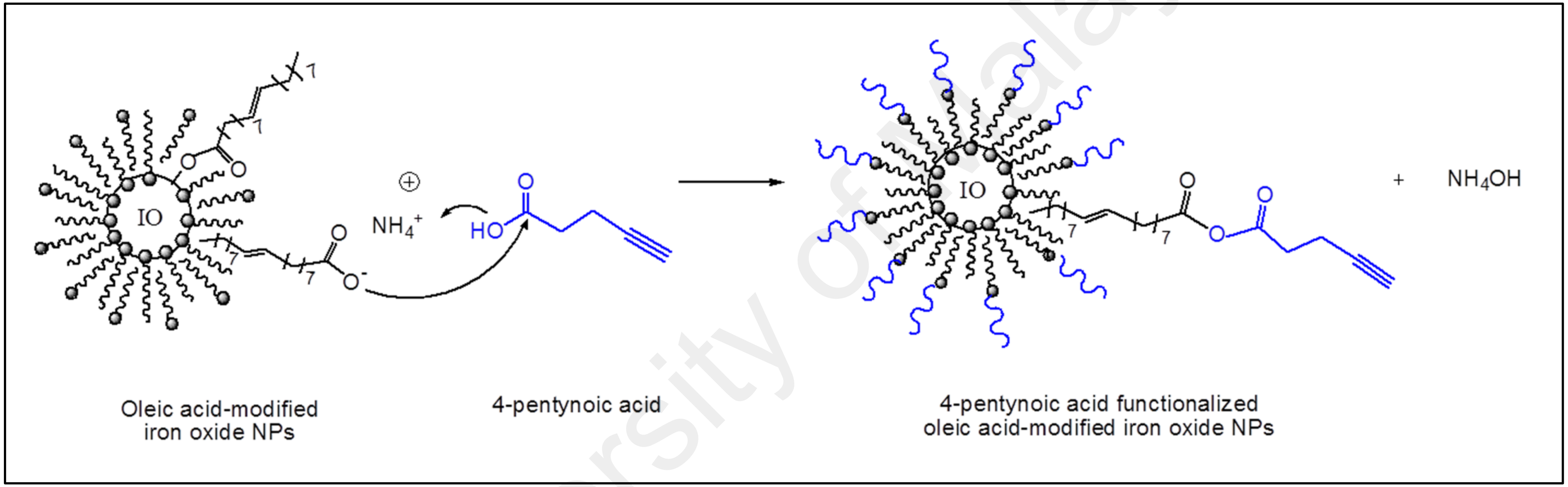

Intermediate of nucleophilic substitution between oleic acid-coated FNPs with 4-pentynoic acid